4H-SiC Detectors for Low Level Ultraviolet Detection

by

Jun Hu

A dissertation submitted to the Graduate School-New Brunswick

RUTGERS, THE STATE UNIVERSITY OF NEW JERSEY

In partial fulfillment of the requirements

For the degree of

Doctor of Philosophy

Graduate Program in

Electrical and Computer Engineering

Written under the direction of

Professor Jian H. Zhao

And approved by

_____

_____

_____

_____

New Brunswick, New Jersey

October, 2008

ABSTRACT OF THE DISSERTATION

4H-SiC Detectors for Low Level Ultraviolet Detection

By Jun Hu

DISSERTATION DIRECTOR:

Professor Jian H. Zhao

Ultraviolet radiation covers the wavelength from 400nm down to 10nm. The superior material properties of 4H-SiC make visible-blind, ultra sensitive and low noise UV photodetectors possible.

The major objective of this Ph.D. thesis research is to design and fabricate high performance 4H-SiC photodetectors for low-level UV detection. Schottky photodiodes, avalanche PIN photodiodes and avalanche phototransistors are studied for various applications.

In this study, the first 4H-SiC Schottky photodiode that can fully cover EUV to NUV range has been successfully fabricated. Ultralow leakage current, high quantum efficiency and high UV-to-visible rejection ratio have been achieved. The first 1×16 4H-SiC Schottky photodiode array with very large detection area has been successfully fabricated and characterized. A novel UV spectrographic system using the 4H-SiC Schottky photodiode array is demonstrated with a fine spectrum resolution.

4H-SiC single photon avalanche photodiode (SPAD) is studied for UV single photon detection. In this work, many challenging issues including bevel edge termination

and ohmic contact have been addressed. The 4H-SiC SPADs show high gain, low dark count rate and good single photon detection efficiency (SPDE). The best 4H-SiC SPAD shows a high counting efficiency of 79% and 32.5% with a dark count rate of 125.3 kHz and 38.8 kHz at -119.4 V and -119 V, respectively. The first 4H-SiC SPAD array has been successfully fabricated and characterized. Only 1 pixel out of 33 pixels shows high leakage and high dark count rate. For all the good pixels working at -119.5V, the gain is greater than 10^6, the dark count rate is less than 100 kHz and the SPDE is more than 2%. The proton irradiation impact to 4H-SiC single photon avalanche diodes is investigated for the first time.

A novel 4H-SiC avalanche phototransistor structure is also studied in this research. The first 4H-SiC avalanche phototransistor is demonstrated with an optical gain greater than 4.5×10^4.

DEDICATION

This work

is lovely dedicated to

my wife, Weining,

and

my parents

who have been, and will always be,

a profound source of

motivation and inspiration

in my

life.

ACKNOWLEDGEMENT

I wish to express my deep gratitude to Professor Jian H. Zhao, my dissertation director, for his guidance and support throughout the dissertation research.

I would like to thank Prof. Kuang Sheng and Prof. Wei Jiang of the department and Dr. Maurice Weiner from the United Silicon Carbide, Inc., for their critical reading of this dissertation.

I would like to thank Dr. Xueqing Li and Mr. Lei Lin for their consistent help with the device simulation. I would also like to thank Dr. Feng Yan and Dr. Xiaobin Xin, pioneers of the thesis work, for their assistance. I am also indebted to Mr. Peter Alexanderov, Dr. Leoid Fursin, and Dr. Jianhui Zhang for their helpful discussion of many critical device process techniques. Many thanks should also be given to Mr. Jian Wu, Mr. Ming Su, Mrs. Xiaohui Wang and all the other colleagues in SiCLAB. Nothing could be accomplished without their contribution and the group effort.

I would like to thank Dr. Kurt Gaskill of Naval research Laboratory for his help on 4H-SiC avalanche photodiode and avalanche phototransistor epilayer growth. Special gratitude would be given to Prof. Charles Joseph of the Department of Physics for his assistance on the EUV photoresponse measurement. I really appreciate the help from United Silicon Carbide, Inc. for their help in the 4H-SiC avalanche photodiode fabrication.

Finally, I wish to express my heartfelt thanks to my wife, my parents for their understanding, patience and sacrifices during the dissertation research.

Contents

Chapter 1 Introduction

1.1 UV detection and its applications

Ultraviolet (UV) radiation covers a wide wavelength span from 400 nm to 10 nm [1], including:

Near ultraviolet (NUV)	400-300 nm
Mid ultraviolet (MUV)	300-200 nm
Far ultraviolet (FUV)	200-100 nm
Extreme ultraviolet (EUV)	100-10 nm

Some time, the following subdivisions may be also encountered:

Ultraviolet-A (UVA)	400-320 nm
Ultraviolet-B (UVB)	320-280 nm
Deep ultraviolet (DUV)	350-190 nm
Vacuum ultraviolet (VUV)	200-10 nm

Ultraviolet research began in the latter half of the 19th century, when the invisible radiation beyond the blue end of visible spectrum began to attract attention. Significant attention has been paid for a long time to the detection of UV radiation, owing to its wide applications in astronomy, biotechnology, material science, ecology, astronavigation and UV location, etc.

1.1.1 EUV detection

The strongest UV radiation source around us is the Sun. The solar EUV irradiance can change by a factor of two in a period of less than one hour and by an order of

magnitude between solar minimum and solar maximum [2]. Absorption of this variable solar EUV radiation is the dominant source of energy for the heating and ionization of the earth's upper atmosphere and ionosphere, which causes phase delay of Global Position System (GPS), radio frequency and microwave communications and orbit shift of satellites in the low-earth-orbit due to the upper-atmospheric drag forces [3].

Detection of the solar EUV irradiation can provide information on the variations in the upper atmospheric density and in the ionospheric electron density, and has great significance in monitoring, specifying and predicting the space environment. However, at such short wavelengths, UV radiation damage becomes a major concern for semiconductor detectors. Semiconductor detectors with high radiation hardness and small volume are highly desired.

Another application is to detect man-made EUV sources such as in EUV photolithographic system.

1.1.2 MUV detection

One of the most attractive applications in MUV range is solar-blind UV detection. The Sun is the strongest irradiation source around us. **Fig. 1-1** shows the average solar irradiation at the top of the atmosphere and at the sea level on the earth. The cut-off wavelength of solar UV irradiance at the sea level of the earth is 280 nm, where the solar irradiance is less than 10^{-20} mW/m^2/nm, which corresponds to 6.1×10^{-5} photons/sec/nm/m^2. The stratospheric ozone layer strongly absorbs the UV emission with the wavelengths from 200 nm to 280 nm [4], and only the light with the wavelength longer than 280 nm reaches the Earth's surface. Simultaneously the far UV emission

from 110 to 250 nm is strongly absorbed by molecular oxygen and can only propagate a very short distance in air. At the extreme UV, atomic and molecular gases become strong absorbers. It is worthwhile to notice that, if the photodetection is carried out between 250 and 280 nm, it is practically free of the interference with the solar irradiation. Therefore, the UV spectrum from 250 to 280 nm is called "solar-blind" window. With visible blind UV detector, which has a high UV to visible rejection ratio, this window has been utilized for many applications including early missile plume detection, flame sensor for gas turbine control system [5, 6], and non-line-of-sight (NLOS) UV communications [7].

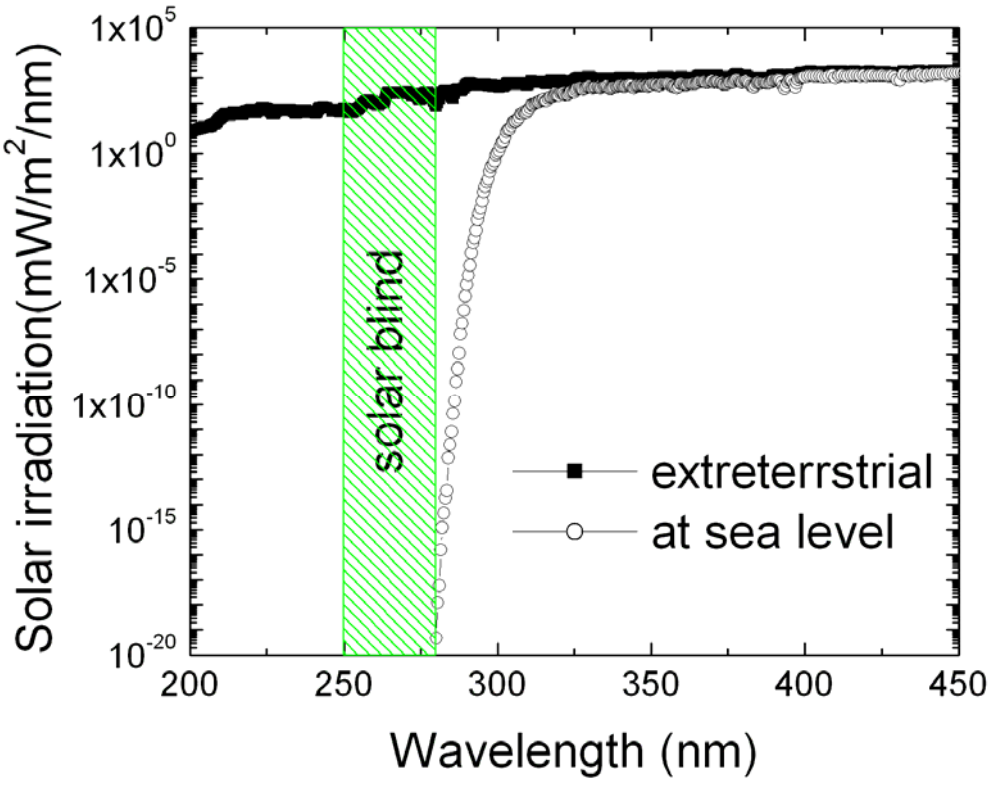

Fig. 1-1 Solar irradiation at the top of the atmosphere and at the sea level on the earth. The stratospheric ozone layer strongly absorbed the UV emission with the wavelengths from 200 nm to 290 nm.

1.1.3 Fluorescence detection in NUV range

Fluorescence is a luminescence phenomenon that is mostly found in cold bodies when the molecules are excited by incident photons. The relaxation of the excited molecules will trigger another photon emission at a longer wavelength than the incident photons. The energy difference between the absorbed and emitted photons ends up being molecular vibrations or heat. The fluorescence detection has been widely used in compound identification, such as biological-agent detection. The fluorescence generated by UV excited biological-agent often expands to NUV range with very weak intensity at the order of pW, i.e. 10^6 photons/sec. Low-level UV detection in the spectral range from 300 to 400 nm is used to identify the presence of a biological organism, to distinguish biological substances from non-biological substances and to differentiate common biological particles from harmful biological agents.

1.2 SiC for UV detection

Silicon carbide exists in at least 70 crystalline forms [8]. 4H-SiC, with a wide band gap of 3.28 eV, is a promising semiconductor material for high power, high temperature, and high frequency applications, owning to its high breakdown electric field, high electron saturation drift velocity, and high thermal conductivity.

In the last decade, tremendous progress has been made in epitaxial growth technologies, and work is still ongoing to reduce defects in SiC material. Micropipe free 4H-SiC substrate has been reported in 2005 [9]. Benefiting from the electrical and optical

properties of 4H-SiC and improved epitaxial growth technologies, 4H-SiC has also been demonstrated to have excellent potential for low level UV and EUV detection:

(a) Visible blindness:

4H-SiC has a wide band gap of 3.26 eV, which makes 4H-SiC intrinsically visible-blind. 4H-SiC photodiodes show a high UV-to-visible rejection ratio. **Fig. 1-2** shows the QE of a SiC PiN detector [10]. The detector shows a high QE of 78% at 290 nm and a very low QE of 5.9×10^{-9} electrons/photon at 442 nm. The cut off wavelength of visible spectrum is 400 nm, where the QE is less than 5×10^{-5} electrons/photon, indicating that a large UV to signal rejection ratio ($>1.5\times10^{4}$) can be achieved. As a result, the detectors show very weak response to most of the solar radiation spectrum and no expensive filters are need for UV detection.

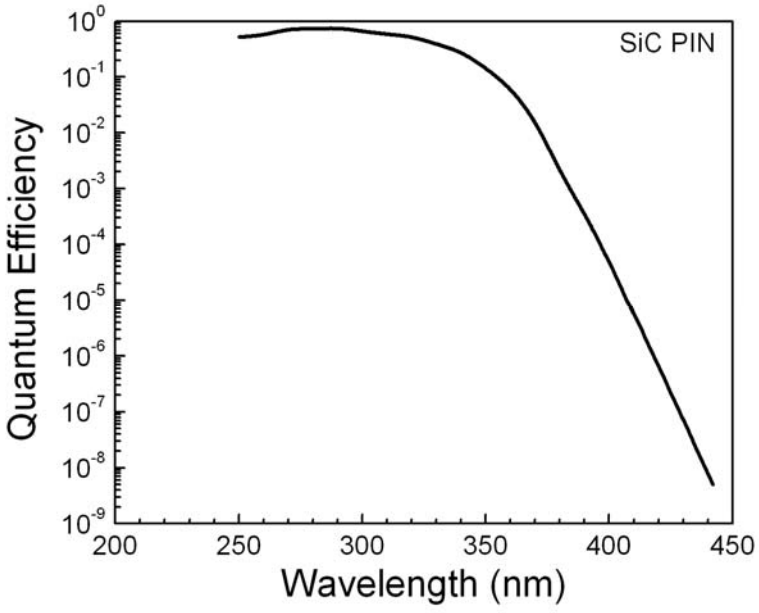

Fig. 1-2 Quantum efficiency of the 4H-SiC PiN detector. The detector has a high QE at 290 nm and a large UV to signal rejection ratio ($>1.5\times10^{4}$)

There are some other wide band gap materials such as ZnO, MgZnO, GaN and AlGaN. They are also visible blind. **Table 1-1** shows the energy band gap of those materials. Compared with those materials, 4H-SiC also benefits from other aspects, including penetration depth, mature growth technology, native thermal oxide etc., which will be discussed in detail later.

Table 1-1 Band gap of several common wide band gap materials.

Material	Eg (eV)	Cut–off wavelength (nm)
4H-SiC	3.26	380
6H-SiC	3.02	413
ZnO	3.37	368
$Mg_xZn_{1-x}O$	3.37-6.7	368-185
GaN	3.4	365
$Al_xGa_{1-x}N$	3.4-6.2	365-200

(b) High quantum efficiency in solar blind spectrum:

Fig. 1-3 shows the penetration depth of 4H-SiC [11] and 6H-SiC [12]. The experimental absorption coefficient of 4H-SiC is still incomplete at the wavelength less than 300 nm, however, the extrapolated absorption coefficients of 4H-SiC show that at the wavelength of 270 –280 nm 4H-SiC has a 1~5 μm penetration depth, which makes SiC detectors for solar blind UV detection with high quantum efficiency practically feasible.

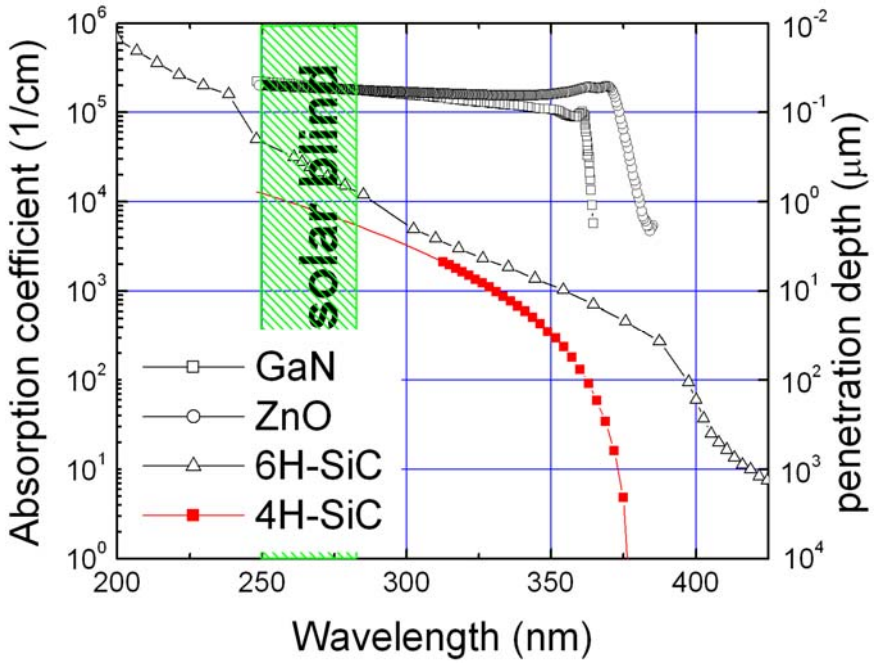

Fig. 1-3 Absorption coefficient and penetration depth of 4H-SiC and 6H-SiC.

As comparison, the penetration depth of other wide band gap semiconductors such as ZnO and GaN is less than 0.1 μm, which means most photons are absorbed at the surface. In this case, the surface recombination is not negligible and the quantum efficiency will be lower unless demanding structure with bandgap engineering is used to provide an optical window.

(c) Low leakage current:

4H-SiC has an ultra low intrinsic carrier density, which is 10^{18} times lower than that of Si, indicating the SiC based detectors have an ultra low leakage current. In addition, 4H-SiC has an ultra low thermal generation rate, which enables very low dark current at high temperature and makes very large detector area possible. For charge sensitive detectors, the extremely low thermal generation enables very long integration time, high transfer efficiency and very low noise. As an example, the dark count rate of SiC single photon avalanche diodes could

potentially be orders of magnitude lower than that of Si, if the SiC wafer quality can be further improved.

GaN and $Al_xGa_{1-x}N$ still suffer from lack of proper substrates and high defect density, which result in high leakage current, low block voltage, low yield of products, and reliability problems.

ZnO and $Mg_xZn_{1-x}O$ are II-VI semiconductor compounds, which are intrinsically n type materials. P-doping of these semiconductors is still a challenge and reliable heavily doped p-type ZnO has not been reported.

(d) Radiation-hardness and high temperature operation:

Displacement energy (E_d), defined as the minimum energy that must be impacted to a lattice atom to remove it from its lattice site, is widely used in radiation hardness measurements. The displacement energy of SiC shown in **Fig. 1-4** is 22eV [13]. Hence, SiC detectors could have better radiation hardness and a longer lifetime in strong radiation environments than Si detectors. NASA recently reported a 55.5 counts/day DCR increment for Si SPADs in a near-earth orbit satellite due to cosmic rays (such as MeV protons) and a distinct DCR increase (2500 cts/s per device) in a solar storm [14]. Whereas SiC exhibits no degradation after exposing to 63.3 MeV protons with a dose of 5×10^{13} cm^{-2} [15]. In addition, 4H-SiC based UV detectors, owning to the ultra low thermal generation rate of carriers, can be operated at high temperature. 4H-SiC shows exellent potential for UV detection under harsh envirenments.

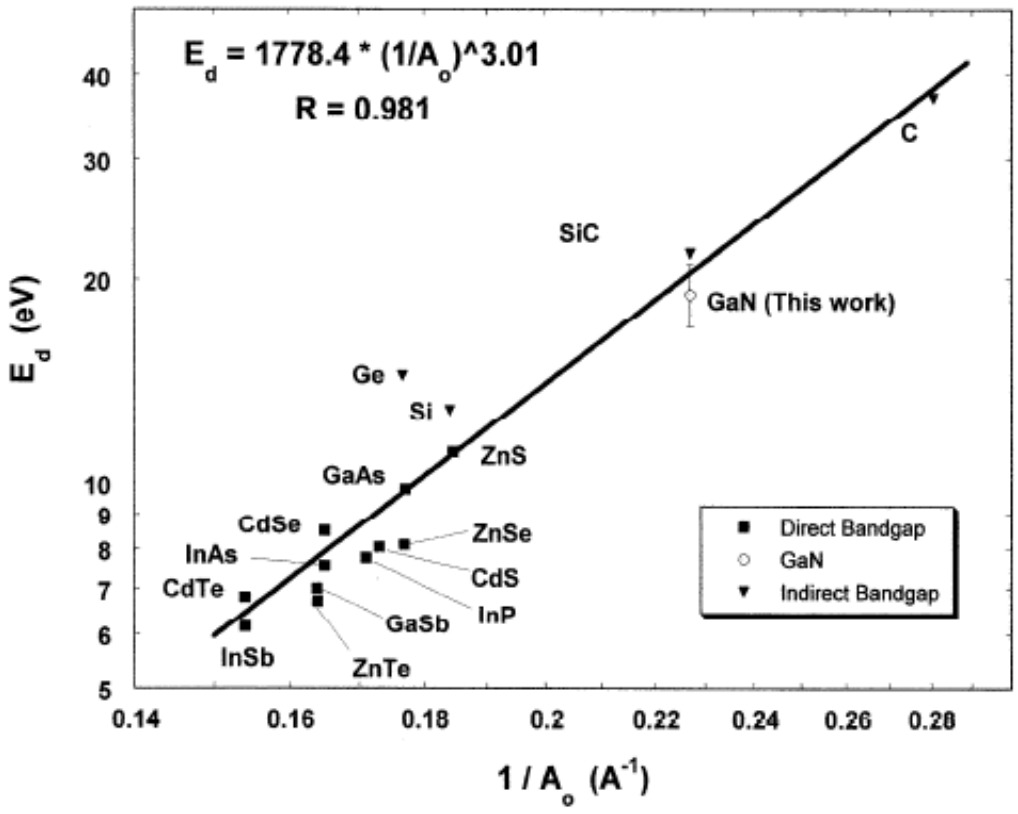

Fig. 1-4 Displacement energy of the most common semiconductors. The displacement energy of SiC is 22eV, indicating SiC detectors have much better radiation hardness and thus longer lifetime in strong radiation environments.

(e) Native thermal oxide:

One important advantage of 4H-SiC is that it has native thermal oxide, SiO_2. During the device fabrication, surface damages and residues can be removed by sacrificial thermal oxidation, and device surface can be passivated by native thermal oxide. Hence, the surface leakage current can be reduced, and the device performance and long term reliability can be improved.

1.3 4H-SiC Schottky photodiodes for low level UV detection

UV spectra span the wavelengths from 10 nm to 400 nm. In this wide range, the absorption coefficient for different materials varies a lot from several nanometers to several tens micrometers. SiC p-i-n photodiodes have been demonstrated as excellent detectors for the wavelength range from 200 nm to 400nm. At the same time, SiC Schottky photodiodes are of interest due to their surface junction, large detection area and relatively easier fabrication process. Forjdh et al have fabricated 6H-SiC Schottky photodiodes by evaporating Ti on substrates with different n-type levels. Better results for n-type 6H-SiC Schottky photodiodes with Au- SiC Schottky barrier were reported by Anikin et al. All those devices have a small detection area and show a leakage current density higher than 10^{-10}A/cm^2 at the reverse bias of -10 V. The UV photoresponse measurement from 200 nm to 400 nm shows a poor UV-to-visible rejection ratio.

In 2004, Feng Yan reported 4H-SiC UV Schottky photodiode with large detection area up to 1 cm^2 [16]. The 5mm x 5mm device shows an ultralow leakage current of less than 1 fA at zero bias and 12 fA at 1V. The quantum efficiency (QE) is higher than 30% from 240 to 320 nm. The detectivity is higher than 10^{15}cmHz$^{1/2}$/W from 210 nm to 350 nm.

Since 1974, the National Oceanic and Atmospheric Administration (NOAA) has operated a series of satellites at geosynchronous orbit to provide critical weather observations. This satellite system is known as the Geostationary Operational Environmental Satellite (GOES) program. On the next series of GOES spacecraft, designated as GOES NO/PQ, an operational EUV sensor has been added to the SEM

suite of instruments. The EUV sensor will monitor the solar EUV irradiance between 5 and 125 nm in five broadband wavelength bands.

SiC p-n photodiode for EUV detection was fabricated in 2006. When the wavelength is less than 200 nm, the quantum efficiency drops dramatically due to the very shallow absorption depth [17].

The first 4H-SiC EUV Schottky photodiode was demonstrated in 2005 by Xiaobin Xin [18]. The QE from 21.5 to 400 nm was determined. The device has a 2×2 mm active area and a leakage current < 1 pA at low bias. The peak QE is 40–45% around 270 nm. Between 120–200 nm, the QE is about 4–20%. EUV light generates multiple electron hole pairs in the range of 21.5 to 77.5 nm, resulting in an apparent QE above 140% at 21.5 nm. The QE from 80 nm to 120 nm was too poor to be measured..

When high speed detection is not required, 4H-SiC Schottky photodiode with large detection area is an excellent candidate for low lever UV and EUV detection from 10 nm to 400 nm, with high quantum efficiency, low leakage current, and high spectral detectivity.

Table 1-2 Review of SiC Schottky photodiodes for UV detection

Structure	Area (cm^2)	I_{dark} (A)	R (A/W)	QE	When	Author
Au-6H-SiC	10^{-2}	10^{-11}A@-1V	0.15A/W@ 215nm	0.8@215nm	1992	M. M. Anikin
Cr-4H-SiC	10^{-2}		0.15A/W@ 250	0.74@250nm	1992	R. G. Verenchikova
Au-6H-SiC		~10^{-8}A@-1V ~10^{-7}A@-5V		0.2@300K 0.4@500K	1998	L. A. Kosyachenko
Au-6H-SiC[6]	$5.3*10^{3}$	<10^{-6}A@-10V ~10^{-3}A@-50V		0.4@360nm	2000	M. Badila
Cr-4H-SiC				0.3@253nm	2001	T. V. Blank
Pt-6H-SiC[7]				0.75(simulation)	2003	G. Brezeanu
Pt-4H-SiC	0.25-1	10^{-14}A@-1V		0.37@240-300nm	2004	Feng Yan
*Ni-4H-SiC	0.04	10^{-12}@-5V		0.45@270nm 4% @120nm	2005	XiaoBin Xin

In summary, 4H-SiC Schottky photodiodes are very attractive for many applications because:

1. 4H-SiC Schottky photodiodes are surface junction devices and show excellent potential for the vacuum UV detection from 10 nm to 200 nm due to its very shallow penetration depth in this UV range.
2. They have high quantum efficiency from 10 nm to 350 nm.
3. They can work at photovoltaic mode without any bias, which will simplify the detection circuit, and improve the detectivity.
4. Detectors with large detection area and photodiode array with large detection area can be fabricated.
5. Compared with other photodetectors, Schottky photodiodes are relatively easier to fabricate.

1.4 4H-SiC avalanche photodiodes and phototransistors

High-speed low-level UV detection is required in many applications such as NLOS, flame detection and UV quantum communications.

Photomultiplier tubes (PMTs) have been often used for these applications because of their high responsivity, high speed, and low dark current. However, they are expensive, large and require high bias. Therefore, solid-state single photon avalanche diodes (SPADs) with high gain and high speed have the best potential their quantum limit approaching capability. Si SPADs, benefiting from the mature growth and processing technologies, have been utilized in the last decade. Recently state-of-the-art Si single photo avalanche diodes with very high detection efficiency (>60%) in the visible

wavelength region and low dark count rate (<1kHz) has been reported [19]. However, for UV detection, Si SPADs only demonstrated Single photon counting down to 400 nm [20]. And Si SPADs have relatively high dark current at room temperature, In order to decrease the dark count rate (DCR), large size Si SPADs need to be cooled down. Moreover, like PMTs, Si SPADs are also very sensitive to visible and infrared radiations. For solar-blind UV detection applications, both Si SPADs and PMTs need to block photons with lower energy than interested UV light using additional filters, which are costly, hard to manufacture and poor for transmission of UV signals. For some specific UV detections in harsh environments, such as a wide operation temperature range and high-energy radiation, degradation of Si SPAD has been observed [14].

To achieve solar-blind operation, SPADs based on wide band gap materials have been studied. Recently, GaN SPADs demonstrated high single photon detection efficiency (SPDE) with low dark count rate, but high defect density and lack of proper substrates limit GaN SPAD's yield [21, 22].

It has also been reported that hole ionization coefficient (β) of 4H-SiC is more than one-order higher than electron ionization coefficient (α) when the critical electric field E_{CR} is less than 4MV/cm(**Fig. 1-5**), which means the avalanche multiplication is dominated by hole injections [23]. In this case, the excess noise can be expressed as:

$$F = kM + (1-k)(2-\frac{1}{M}),$$

where M is the avalanche multiplication, k is the ionization ratio. The excess noise is dominated by the first term.

With a low ionization ratio of k=α/ β, 4H-SiC APDs should have a much lower excess noise [24]. As comparison, for most III-V semiconductors, electron ionization coefficient is close to hole ionization coefficient.

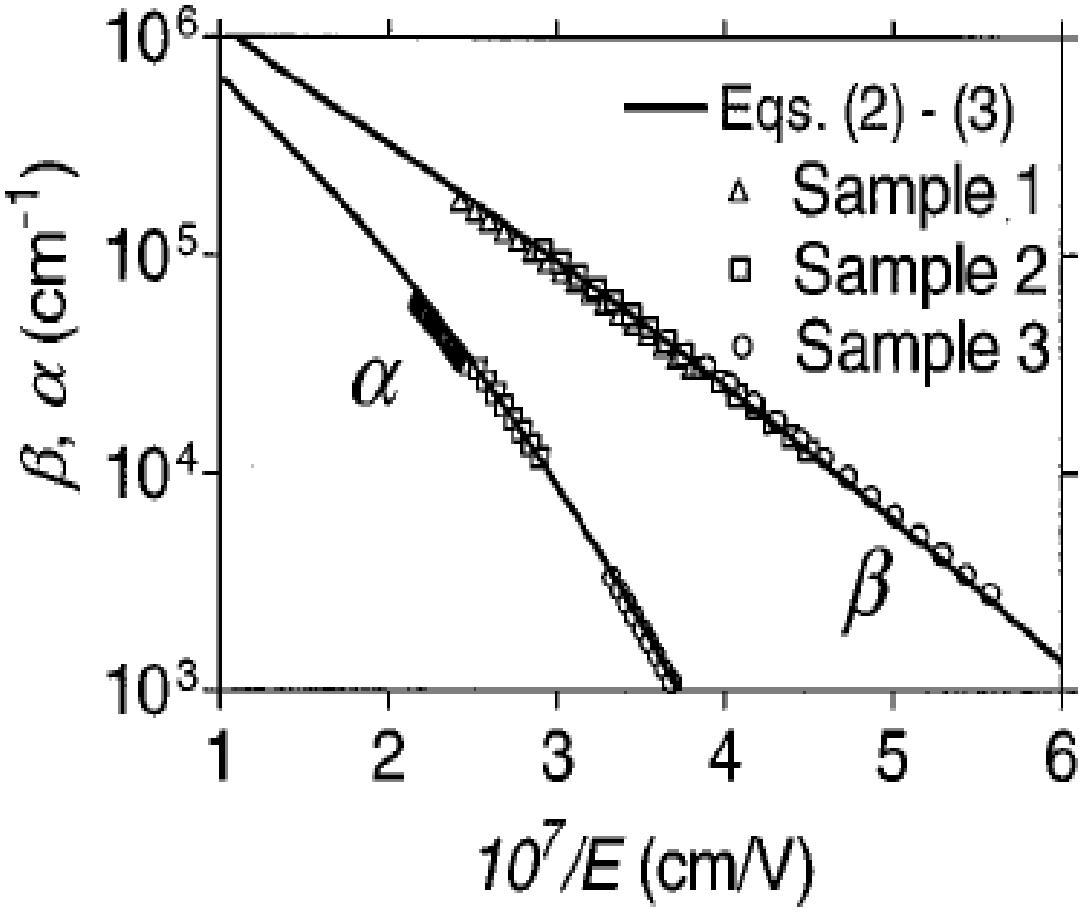

Fig. 1-5 Hole ionization ratio (β) and electron ionization ratio (α) of 4H-SiC. The avalanche multiplication is dominated by hole injections.

In addition, SiC has high junction failure power density (P_D), **Fig. 1-6** shows the calculated P_D of SiC, GaN, and Si. P_D of 4H-SiC is approximately ten times higher than that of Si and five times higher than that of GaN. Owing to these advantages, 4H-SiC UV SPADs have been studied extensively recently. Since the first 4H-SiC SPAD was reported in early 2005 [25], a rapid progress has been made subsequently. 4H-SiC

SPADs under the passive quenching and the gated quenching modes with high performance have been reported [26-30].

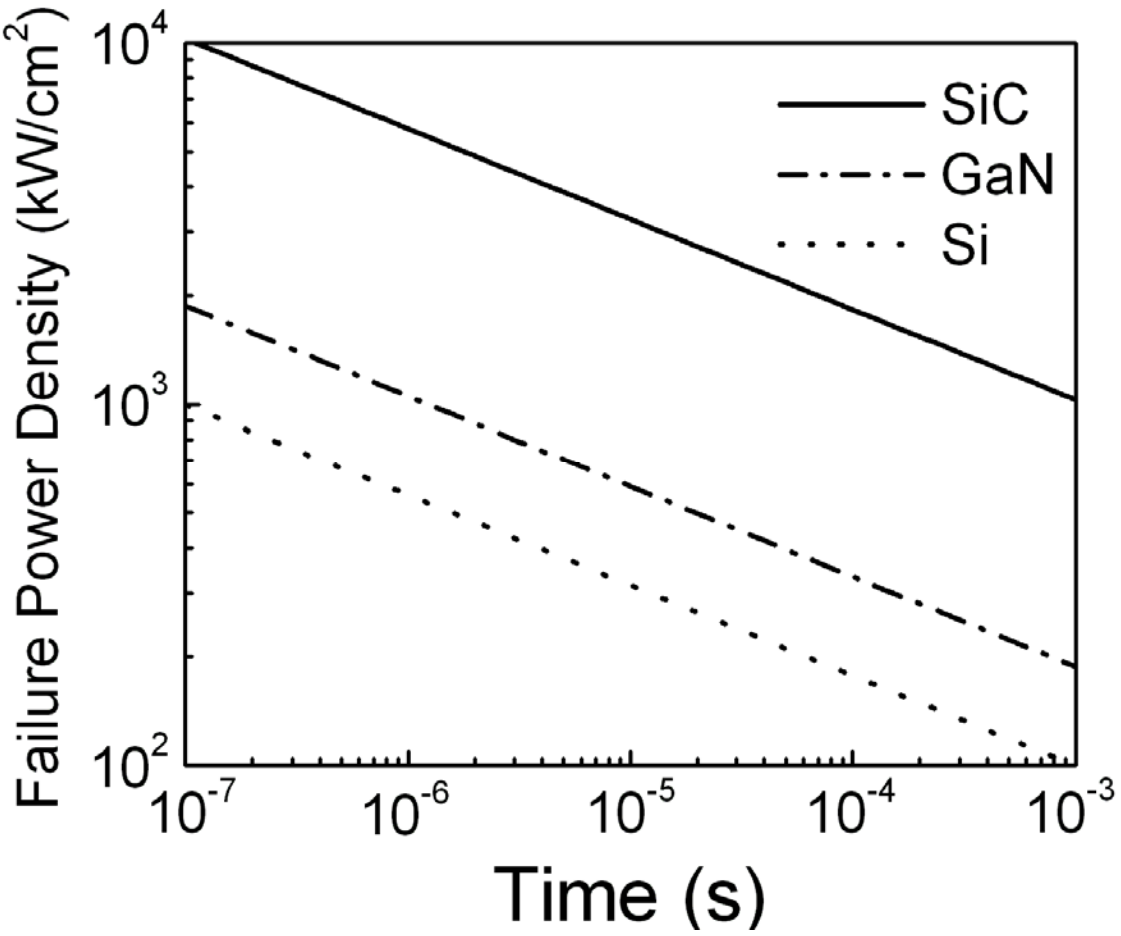

Fig. 1-6 Calculated failure power densities of SiC, GaN, and Si. The power density of 4H-SiC is approximately ten times higher than that of Si and five times higher than that of GaN.

Another possible candidate for SiC UV single photon detection is SiC avalanche phototransistor. Regular phototransistor is an optical detectors that provides internal gain. Avalanche phototransistor may combine the advantages of avalanche photodiode and regular phototransistor and provide a higher gain at with a lower dark count rate than avalanche photodiode.

In 1975, the first Si avalanche phototransistor has been demonstrated with the capability of generating nanosecond output pulses at high current levels [31], and a laser-activated avalanche transistor compatible with planar processing has also been reported [32]. Later, Heterojunction avalanche phototransistors were reported with higher gains [33-36].

SiC phototransistor was fabricated in 1998 with an optical gain of 145 at 25 ^{o}C and 106 at 250 ^{o}C, under a 10 V bias and 10 W incident optical power at the wavelength of 500 nm.

In summary, 4H-SiC avalanche photodiodes and phototransistors have been studied for about 10 years. Compared with other photodetectors, SiC avalanche photodiodes and phototransistors demonstrate the following major advantages:

1. 4H-SiC avalanche photodetectors benefit from a high gain when working at the voltage higher than the avalanche breakdown. The gain can be $>10^6$. With better design and fabrication discussed in this thesis, the gain can be higher than 10^9.
2. Ultra low dark current can be achieved.
3. With proper design, 4H-SiC avalanche photodetectors present a high quantum efficiency in the solar blind UV range from 270 -280 nm.
4. They can be used for single photon counting detection applications, such as the non-line-of-sight (NLOS) UV communication in solar blind UV range.
5. High frequency, high speed UV detection requirements can be met.
6. They are visible blind with a high UV-to-visible rejection ratio.

1.5 Purpose of This dissertation research

This PhD thesis research is to further investigate the crucial issues in 4H-SiC photodetectors for low level ultraviolet detection applications. The thesis research has two major parts: one is about 4H-SiC Schottky photodiodes and photodiode arrays, and the other is about 4H-SiC avalanche photodiodes and phototransistors. The device design, fabrication process and characterization are studied in order to improve and optimize the overall performance.

Specifically, the objective of the research on 4H-SiC Schottky photodiodes and arrays includes:

1. To design and fabricate UV detectors and arrays for the visible-blind low-level EUV-NUV detection.
2. To address the major challenging issues in 4H-SiC Schottky photodiode design and fabrication, to develop processing technologies, and to characterize the major parameters of the 4H-SiC Schottky photodiode, including leakage current, quantum efficiency and uniformity. The photodiode and array should have a high quantum efficiency (>20%), a large detection area, a high sensitivity from EUV to NUV range, and a good uniformity within the optical window and among the pixels.
3. To demonstrate 4H-SiC Schottky photodiode arrays with large detection area for EUV and UV detection applications.
4. To demonstrate a UV spectrographic system using a 4H-SiC Schottky photodiode array with a good spectrum resolution.

The objective of the research on 4H-SiC avalanche photodetectors includes:

1. To develop process technologies for 4H-SiC avalanche photodetectors including edge termination, ohmic contact, etc.
2. To design and fabricate 4H-SiC avalanche photodiodes toward single photon counting detection applications. To improve and optimize the performance of single photon avalanche diodes.
3. To characterize the 4H-SiC single photo avalanche diode, including leakage current, multiplication gain, quantum efficiency (QE), single photon detection efficiency (SPDE) and counting efficiency (CE).
4. To demonstrate and characterize the 4H-SiC single photon avalanche diode arrays.
5. To design, fabricate and characterize 4H-SiC avalanche phototransistors.

1.6 Thesis outline

In the introduction, material properties of 4H-SiC and previous research on 4H-SiC photodetectors, including 4H-SiC Schottky photodiodes and avalanche photodiodes, are reviewed.

4H-SiC Schottky photodiodes and arrays are studied in chapter 2. Firstly, the design of 4H-SiC Schottky photodiodes, including the wafer structure, Schottky metal properties, device design and photo mask information, is presented. Secondly, the fabricated 4H-SiC Schottky photodiodes are characterized, and their I-V and C-V characteristics and quantum efficiencies are presented. At the end, the characterization results of 4H-SiC Schottky photodiode array, including I-V characteristics, cross-talk, spectrographic measurement results are presented.

4H-SiC single photon avalanche diodes are studied in chapter 3. Firstly, device structure design, edge termination design, and ohmic contact study are presented.

Secondly, the characterization results of 4H-SiC single photon avalanche diode with on-mesa overlay and off-mesa overlay are presented in two sub-chapters. Then the characteristics of 4H-SiC single photon avalanche diode array are presented.

In chapter 4, we investigate for the first time the 4H-SiC punch-through and avalanche phototransistors. The design, fabrication and characterization of 4H-SiC phototransistors are presented.

Finally, a summary of this thesis study and future work suggestions are presented at the end of this dissertation.

The research work included in this dissertation was carried out from September 2003 to July 2008.

Chapter 2 4H-SiC Schottky photodiodes and arrays

2.1 Design and fabrication of 4H-SiC Schottky photodiodes and arrays

The device design of 4H-SiC Schottky photodiodes and arrays, including Schottky metal properties, device structure, device geometry, and mask information, are discussed in this part. In order to fabricate 4H-SiC Schottky photodiodes and arrays with good performance, the following issues need to be considered:

(a) Quantum efficiency (QE): Only the photons absorbed in the absorption layer contribute to the quantum efficiency. For 4H-SiC, the absorption depth drops dramatically from several micrometers to several nanometers when the wavelength decreases from the near UV region to the EUV region [37]. At the wavelengths from 100 to 160 nm, the penetration depth is less than 5 nm, which means that most incident photons are absorbed at the surface. Many photon-generated carriers are recombined due to the surface recombination, which causes poor QE. A 4H-SiC PiN diode has been demonstrated with a high QE (~80%) in the near UV region, whereas in EUV region, the QE is as poor as less than 1% [38]. High QE (> 20%) in this region is required for accurate EUV detection.

(b) Leakage current: For low level EUV and UV detection, ultra low leakage current is required to improve the spectral detectivity. For GOES-R EUV

detection applications, the total noise current is required to be less than 2 fA at 1 Hz.

(c) Detection area: Sensitivity of photo detectors can be improved by increasing the detection area. However, the existence of defects in a device may cause high leakage current and limit the detector size. **Fig. 2-1** shows some typical defects of 4H-SiC, such as micropipes, closed core screw dislocations, poly-type inclusions, and growth pits [39-41]. Some defects, such as the first three types mentioned above, have been identified to cause high leakage current. Some defects, such as small growth pit, are surface defects, and our experiments do not show any evidence that those surface defects can cause high leakage. To identify the effects of different defects on the leakage current is a "must" to improve the performance and yield of the photodiodes.

(d) Uniformity: As we mentioned before, the QE is low at the wavelength between 100 and 160 nm due to the very shallow penetration depth. Therefore uniformity is important for low level EUV and UV detection. A <5% non-uniformity is required.

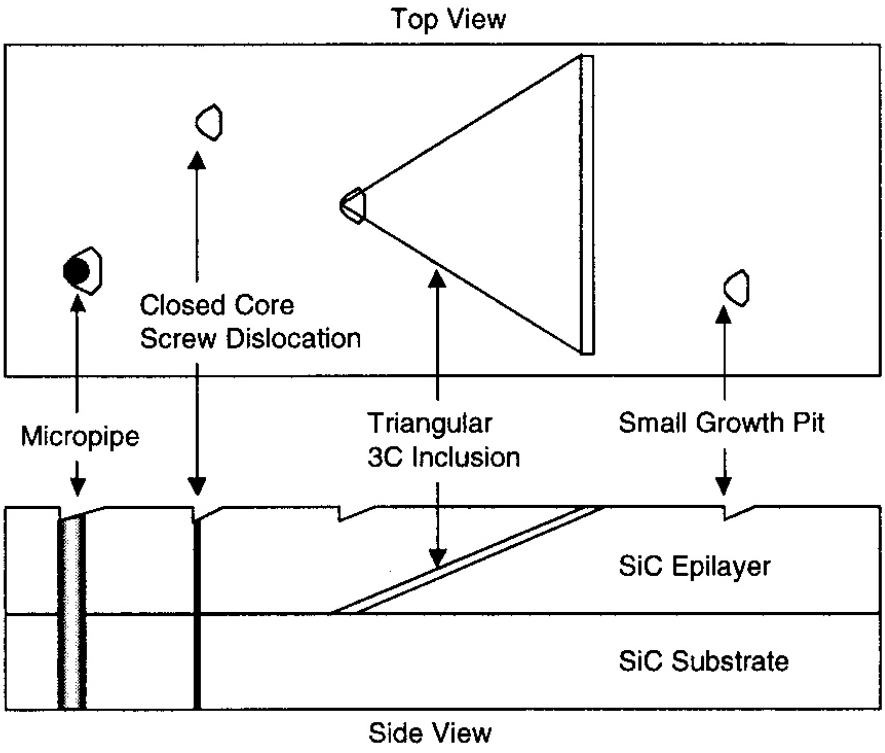

Fig. 2-1 Some common defects on SiC epilayer.

2.1.1 Schottky metal properties

4H-SiC Schottky photodiodes are fabricated on the n- type SiC epilayer. Only those metals with high work function, high transmittance to UV light are excellent candidates for Schottky contact with n-type 4H-SiC [42]. Table 2-1 shows work functions of some common metals.

Transmittance of the Schottky metal to the ultraviolet wavelength determines the QE of Schottky photodiodes. The transmittance of Schottky metals varies with the UV wavelength and is measured before 4H-SiC Schottky photodiode fabrication.

Table 2-1 Work functions of some common metals

Metal	Atomic number	Density (g/cm^3 at 300K)	Electron work function (eV)
Al	13	2.702	4.28
Au	79	19.32	5.10
Cu	29	8.96	4.65
In	49	7.31	4.12
Mo	42	10.22	4.60
Ni	28	8.9	5.15
Pt	78	21.45	5.65
Ti	22	4.54	4.33
W	74	19.35	4.55
Zn	30	7.13	4.33

Firstly, a calibrated Si UV enhanced photodiode is used to measured the photocurrent, I_{ph}, generated by the transmitted photons through a sapphire substrate from 200 nm to 400 nm. Then, the Schottky films are deposited on the sapphire substrate using a Denton DC magnetic sputtering system and the transmitted photocurrent, I_{tr}, is measured again at the same wavelength. The transmittance of the Schottky film is defined as: $T = I_{tr} / I_{ph}$.

Fig. 2-2 shows the transmittance of different semitransparent films. The thickness of the films is measured using atomic force microscopy (AFM). The 5 nm Ni film shows

the highest UV transparency in this UV region, and the 4.5 nm Pt film is also a good candidate.

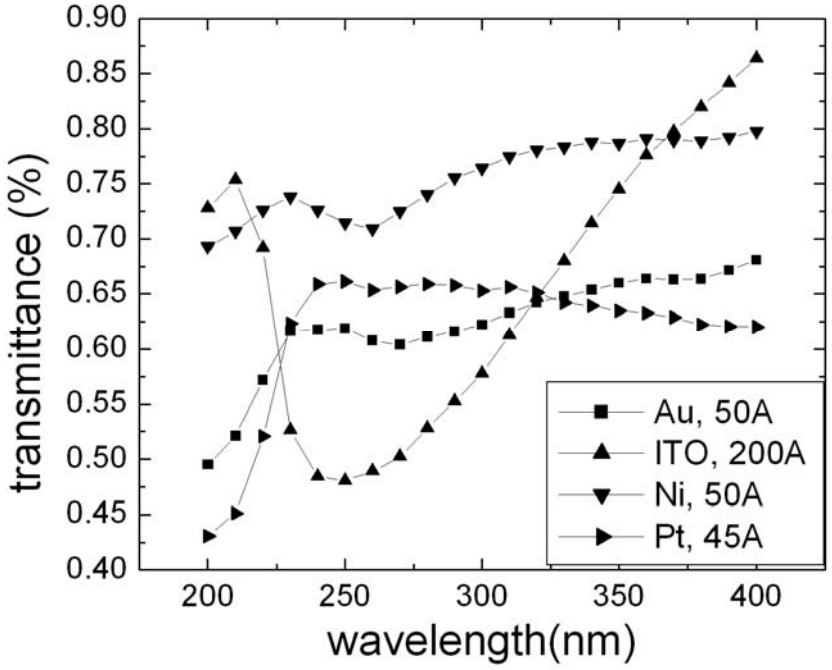

Fig. 2-2 Transmittance of different Schottky metals.

Another important issue is the surface morphology of Schottky metals on SiC surface. Photo-response uniformity of detectors with large detection area is very critical for accurate low-level EUV and UV detection. **Fig. 2-3** shows the surface roughness of Au, Ni and Pt semitransparent films with the thickness of 45~50 Å on 4H-SiC. The Pt semitransparent film is the smoothest and the Au film shows the roughest surface.

Considering the work function, morphology and UV transparent of Schottky metal films, semitransparent Ni and Pt films are chosen as Schottky contacts with 4H-SiC n- drift layer.

Fig. 2-3 Schottky metal films on 4H-SiC surface. All the films are about 5nm thick. The top is Au film on SiC, the center is Ni and the bottom is Pt. Pt shows the best film quality among the three films.

2.1.2 Device structure design

Fig. 2-4 and **Fig. 2-5** are the cross sectional views of the 4H-SiC Schottky photodiode and array, respectively.

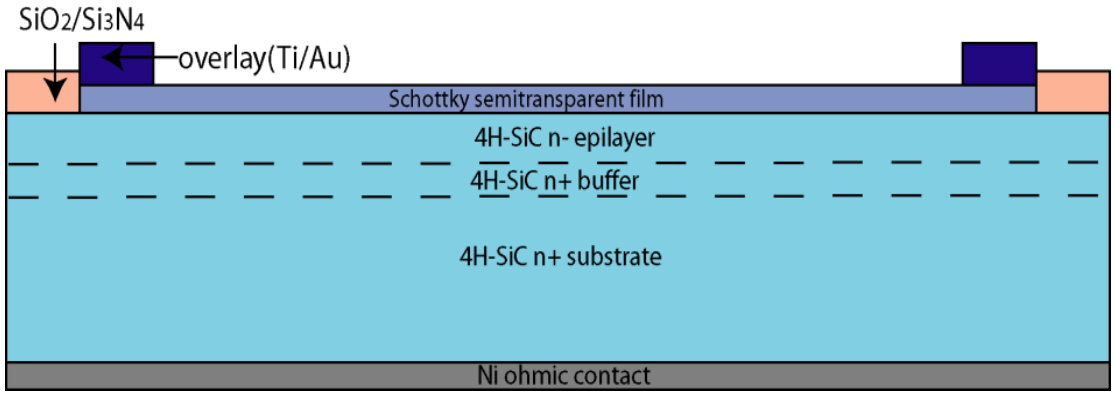

Fig. 2-4 Cross sectional view of 4H-SiC Schottky photodiode with large detection area.

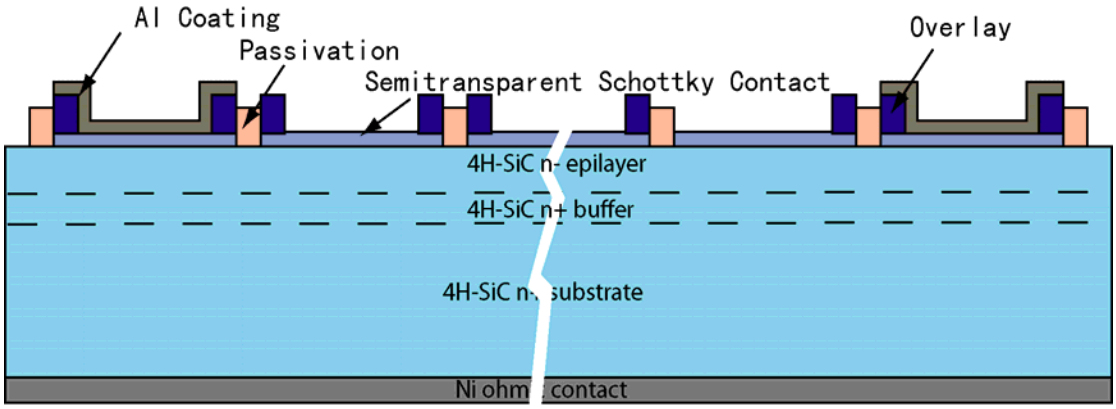

Fig. 2-5 Cross sectional view of 4H-SiC Schottky photodiode array with large detection area.

The vacuum UV light from 5 nm to 200 nm has a very shallow penetration depth in 4H-SiC, and the major portion of the incident photons will be absorbed at the Schottky interface. Therefore, to improve the QE of the photodiodes, ultra-thin semitransparent films of Pt and Ni are chosen as Schottky contacts and the active n- drift layer is designed to be thick enough.

In this work, the n- drift layers with very low doping are designed with different thickness of 5um and 10um, respectively, for 4H-SiC UV/EUV Schottky photodiode.

SiC epilayers are grown on off-axis SiC substrates. The use of off-axis substrates enables step-controlled epitaxy [43, 44]. The steps on the growth surface expose several alternating silicon and carbon planes, thereby transferring stacking information which preserves the polytype in the epitaxially grown film. The epilayer information of the wafers for 4H-SiC Schottky photodiode fabrication is shown in **Table 2-2**.

Defect density limits detection area and the yield of 4H-SiC Schottky photodiodes and arrays. The SiC substrate with ID of 2A.4N.4D.1S is 4^o off the c-axis and the others with IDs of 2A.4N.8D.1S and W4NPD8C-L0S1 are 8^o off.

Table 2-2 Wafer information for 4H-SiC Schottky photodiode fabricaton

Wafer ID	Degree off the c-axis	Epilayer doping (cm^{-3})	Epilayer thickness (um)
2A.4N.4D.1S	4^o	4e14	10
2A.4N.8D.1S	8^o	4e14	10
W4NPD8C-L0S1	8^o	4e14	5

The 4^o off wafer has the dominating defects shown in **Fig. 2-6**, which introduce high leakage current and degrade the device performance. Some spikes and holes with the size of about 25um in diameter are also found on the surface. The spikes are about 10 um high and the holes are about 15 um deep.

The 8^{o} off wafer (2A.4N.8D.1S) has needle-shape defects, which are about 40 μm long. The defect density is about 1/mm^{2}. Those defects shown in **Fig. 2-7** do not cause any leakage, indicating they are very shallow on the SiC surface.

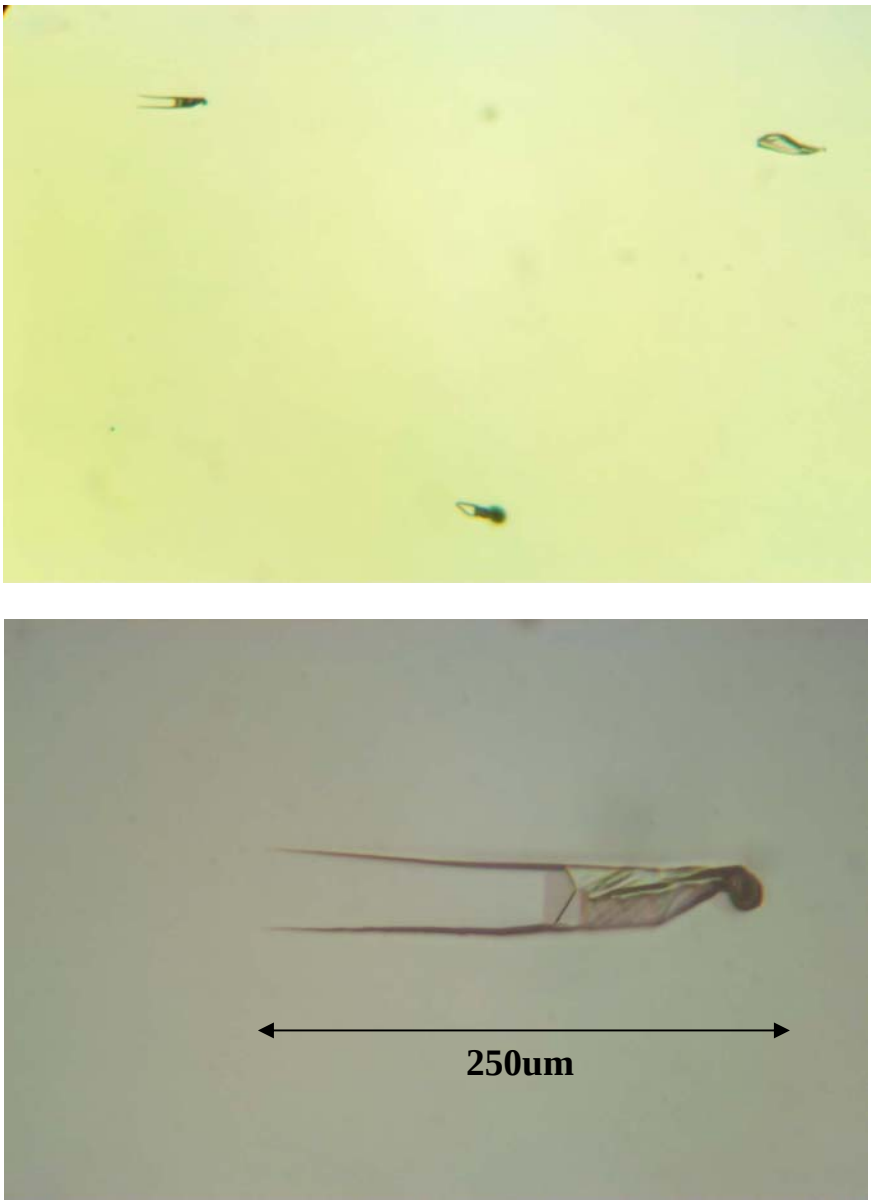

Fig. 2-6 Dominating defects of epilayer on 4^{o} off-axis 4H-SiC substrate.

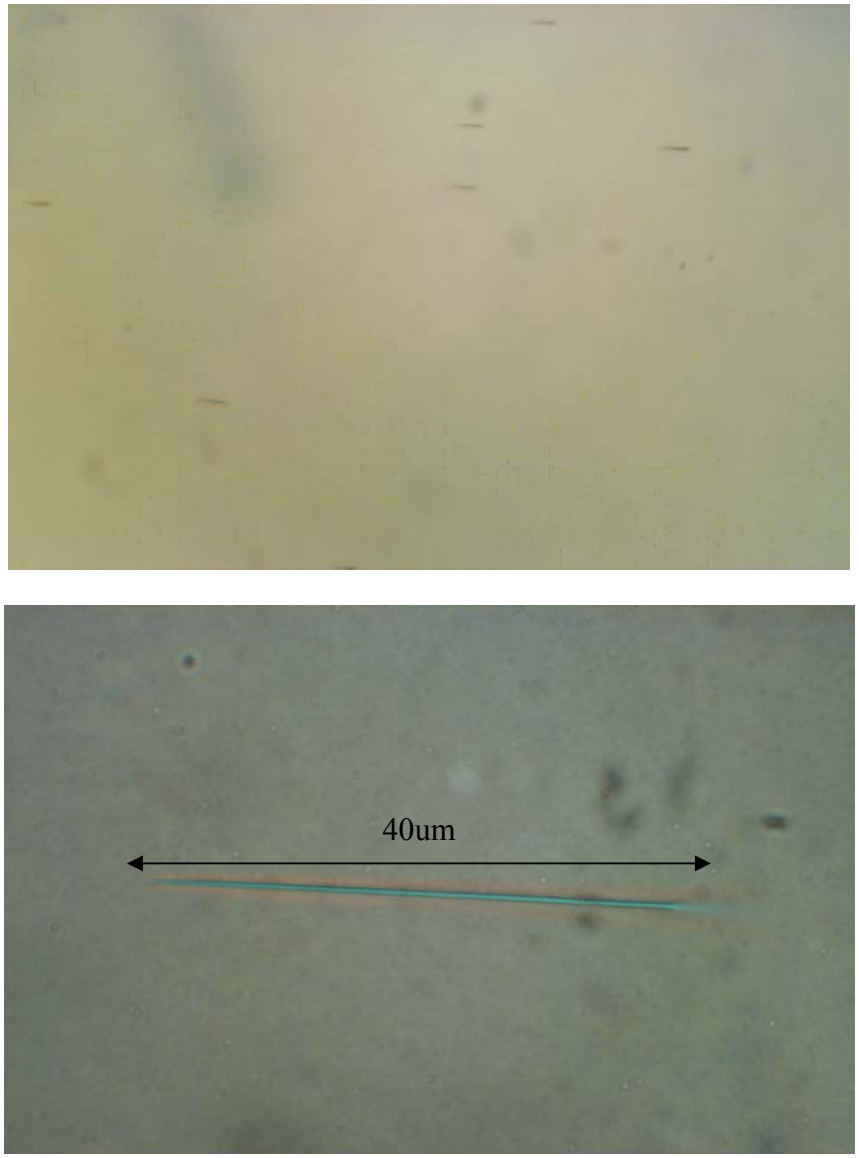

Fig. 2-7 Dominating defects of epilayer on 8^{o} off-axis 4H-SiC substrate. The defect density is about 1defect/mm^{2}

C-V measurement of wafer W4NPD8C-L0S1 is carried out on a 5 mm × 5mm Ni/4H-SiC photodiode to -20 V and shown **Fig. 2-8**. The doping profile of the device shown in **Fig. 2-9** extrapolated from the C-V curve indicates that the n- drift layer is 4.6 μm thick with a doping concentration increasing from 1.5×10^{14} cm^{-3} at 3 μm to

$1\times10^{15}cm^{-3}$ at 4.5 μm. The graded doping profile is different from the designed uniform doping, and the epilayer is also slightly thinner than the designed structure.

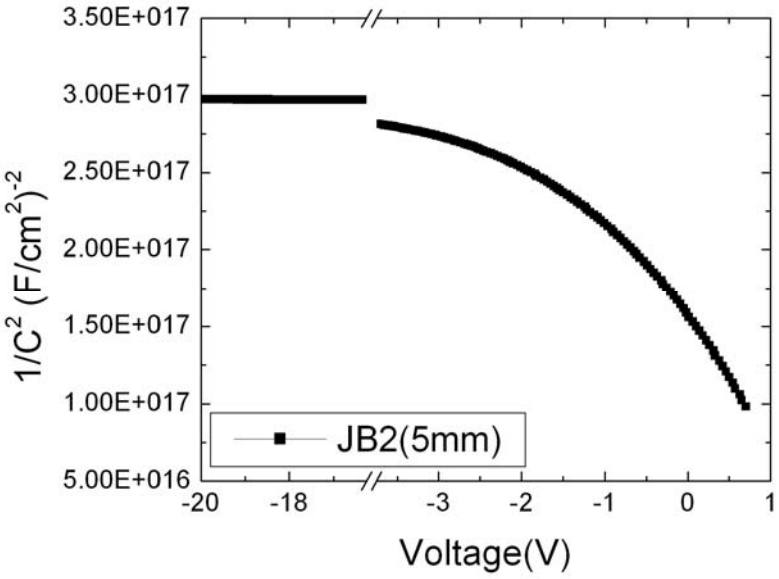

Fig. 2-8 C-V characteristics of Ni/4H-SiC Schottky photodiode on the wafer (W4NPD8C-L0S1).

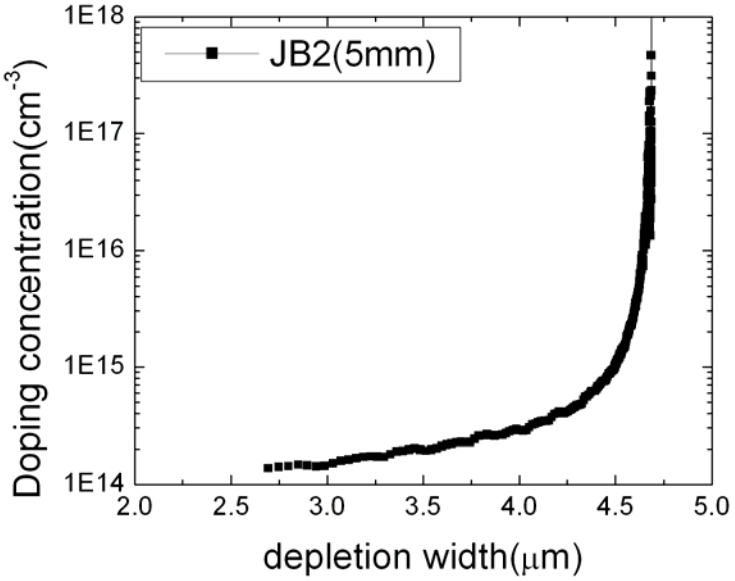

Fig. 2-9 The extrapolated doping profile of wafer W4NPD8C-L0S1.

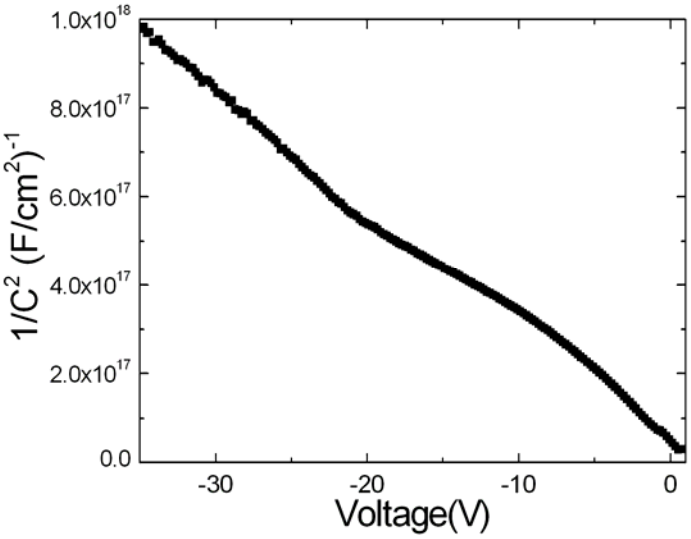

Fig. 2-10 C-V characteristics of Ni/4H-SiC Schottky photodiode on the wafer (2A.4N.8D.1S).

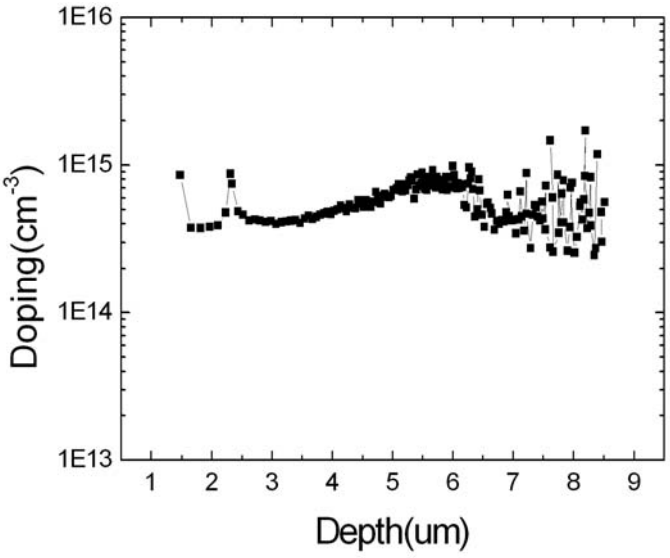

Fig. 2-11 The extrapolated doping profile of wafer 2A.4N.8D.1S.

The wafer 2A.4N.8D.1S from IntrinSiC, Inc. has a 10 μm n- epilayer. The C-V characteristics measured to the system limit of -40 V on a 5 mm × 5mm Pt/4H-SiC photodiode are shown in **Fig. 2-10**, and the extrapolated doping profile from the C-V curve is show in **Fig. 2-11**. The doping concentration of n- drift layer is ~$6\times10^{14}$$cm^{-3}$,

which is higher than the designed target, and the drift layer is thicker than 9 μm. Due to the voltage limit of the C-V measurement, the real thickness of the n- drift layer is unknown.

2.1.3 Mask information

The mask for the fabrication of UV/EUV Schottky photodiodes is shown in **Fig. 2-12**. It consists of devices with different sizes of 1cm ×1cm, 5mm×5mm, 3mm×3mm, 2mm×2mm, and 1mm×1mm.

The mask for the fabrication of EUV Schottky photodiode arrays is shown in **Fig. 2-13**. The pixel size is 0.75mm×15.6mm with a detection area of 9.75 mm^2.

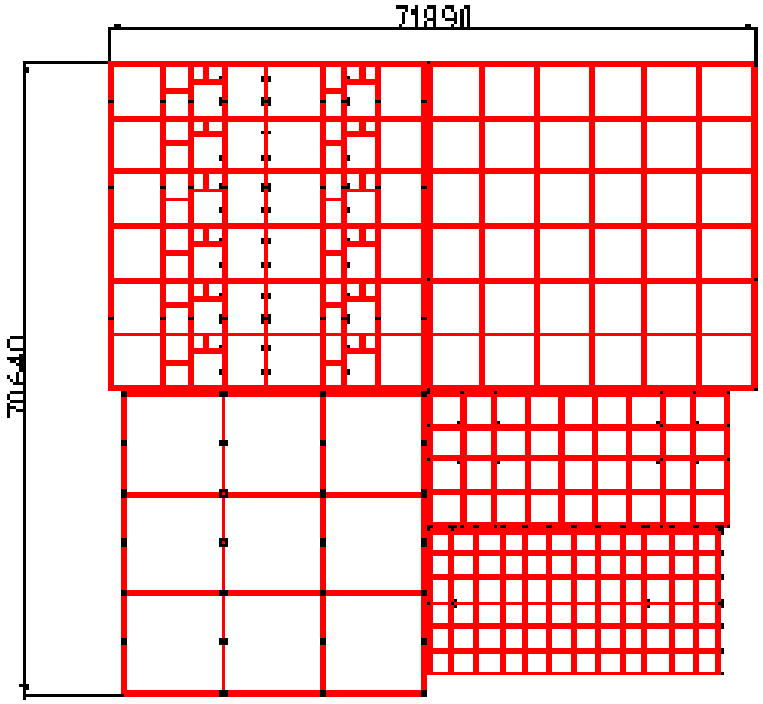

Fig. 2-12 Mask layout of 4H-SiC Schottky photodiode fabrication.

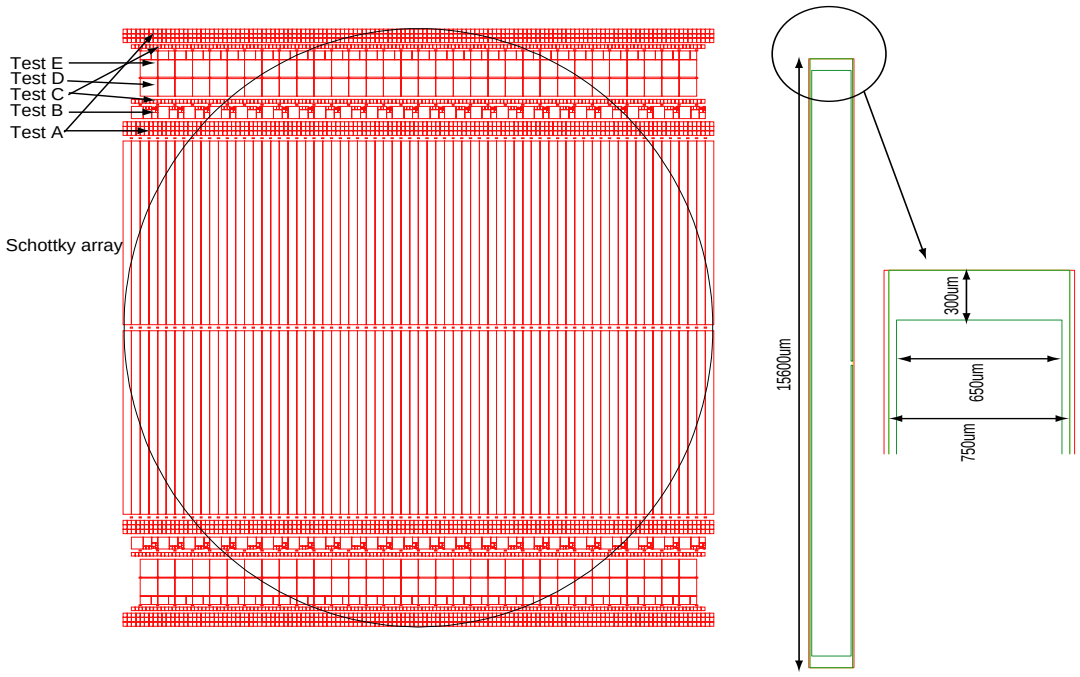

Fig. 2-13 Mask for 4H-SiC Schottky photodiode array fabrication. The pixel size is 0.75mm×15.6mm with a detection area of 9.75 mm^2.

2.1.4 Fabrication of 4H-SiC Schottky photodiodes:

Our Schottky photodiodes are fabricated on 4H-SiC wafer with a 5 or 10μm lightly doped n-epilayer. The schematic processing procedure is shown in **Fig. 2-14**.

1. Device passivation: After a standard RCA clean is carried out, a thin thermal oxide layer is grown in wet oxygen at 1050 ^{o}C for 30 minutes and then removed by diluted HF. The purpose is to remove damages and contaminations on the sample surface. After the sacrificial oxide is removed, the device is passivated by growing a thin layer of thermal oxide in wet oxygen at 1050 ^{o}C for 3 hours, followed by another 200 nm PECVD SiO_2 and 300 nm PECVD Si_3N_4 Deposition.
2. Backside ohmic contact formation: After the oxide is removed from the backside by wet etching using buffered oxide etchant (BOE) 7:1, a 300 nm Ni layer is

sputtered and then annealed at 1050 ^{o}C for 5 min in N_2/H_2 foaming gas to form the n-type ohmic contact. Simultaneously, the top PECVD SiO_2 \ Si_3N_4 layer is condensed by the annealing.

3. Optical window: The optical window is defined by photolithography using photoresist AZ5214. The patterned photoresist is condensed by hard baking at 130 ^{o}C for 30 minutes. The top Si_3N_4 layer in the optical window is etched away by CF_4-only ICP dry etching using the condensed photoresist as etching mask and the SiO_2 layer underneath as stopper layer. Then the SiO_2 layer underneath is removed by wet etching and the optical window is open.
4. Schottky contact formation: a semitransparent Schottky metal film (Ni or Pt) is immediately deposited in the optical window as the Schottky contact, when the window is open. Lift-off technology is used to remove the metal sputtered outside of the optical window.
5. Overlay formation: A thick Schottky layer is first sputtered on the periphery of the Schottky contact followed by an overlay deposition. The overlay metal is 20 nm Ti and 300 nm Au, which is good for wire bonding. A thin Ti layer can improve the adhesion of Au layer on the Schottky contact. Otherwise, the overlay may peel off during the wire bonding. Because the work function of Ti is lower than the Schottky metal, a thick Schottky metal layer, deposited between the Schottky contact and the overlay, can prevent the Schottky barrier lowing caused by the contact of the overlay on the ultra thin Schottky film.

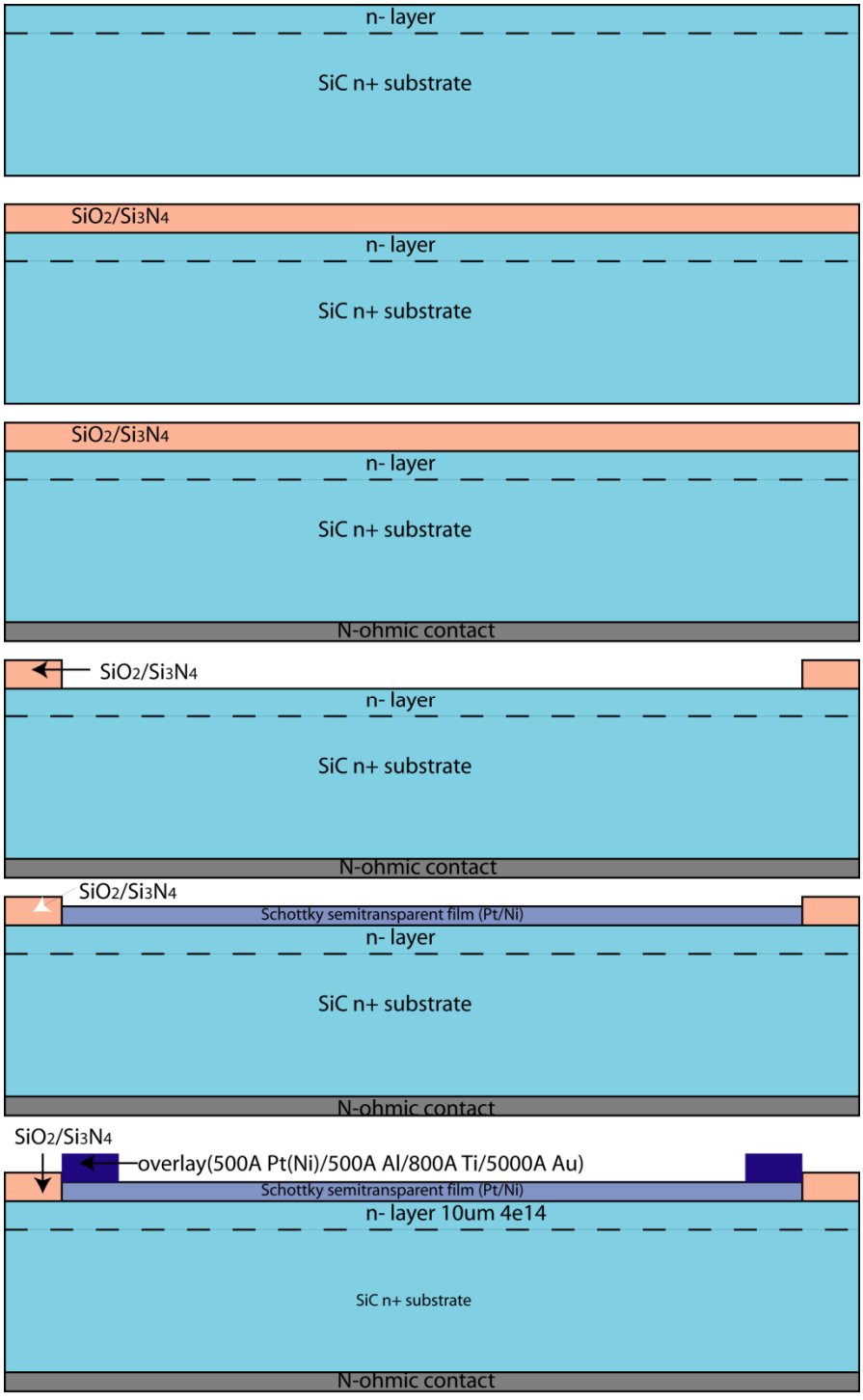

Fig. 2-14 Schematic Processing procedures of 4H-SiC Schottky photodiodes

2.1.5 Fabrication of 4H-SiC Schottky photodiode arrays

The photomask set for 4H-SiC Schottky photodiode array fabrication is shown in **Fig. 2-13**. Our Schottky photodiode array is fabricated on a 2-inch 4H-SiC wafer (**2A.4N.8D.1S**) with a 10 μm lightly doped n-epilayer on an n+ substrate. Device fabrication is exactly the same as the individual 4H-SiC Schottky photodiode. Device passivation is first accomplished by growing a thin layer (50 nm) of thermal oxide in wet oxygen at 1050 ^{o}C for 3 hours followed by another PECVD deposition of 200 nm SiO_2 and 300 nm Si_3N_4. After the oxide is removed from the backside of the wafer, a Ni alloy is sputtered and then annealed at 1050 ^{o}C for 5 min in H_2/Ar (5%/95%) gas mixture to form the n-type ohmic contact. The optical window is defined by the ICP etching of Si_3N_4 and wet etching of SiO_2 on the top n-layer using photo resist as the etching mask. And then a semitransparent Pt film of thickness 15 Å is deposited in the window as the Schottky contact. A thick Pt/Ti/Au overlay contact is sputtered on the periphery of the Pt Schottky film for wire bonding. Finally, 500 Å Al is sputtered in the optical window of the two end "blind" pixels. The inset of **Fig. 2-15** shows the top view of the 1×16 4H-SiC Schottky photodiode array. Each pixel is 750 μm wide, 15.6 mm long and has an optical window of 9.74 mm^2. The total detection area is 1.365 cm^2 and occupies 73% of the array area.

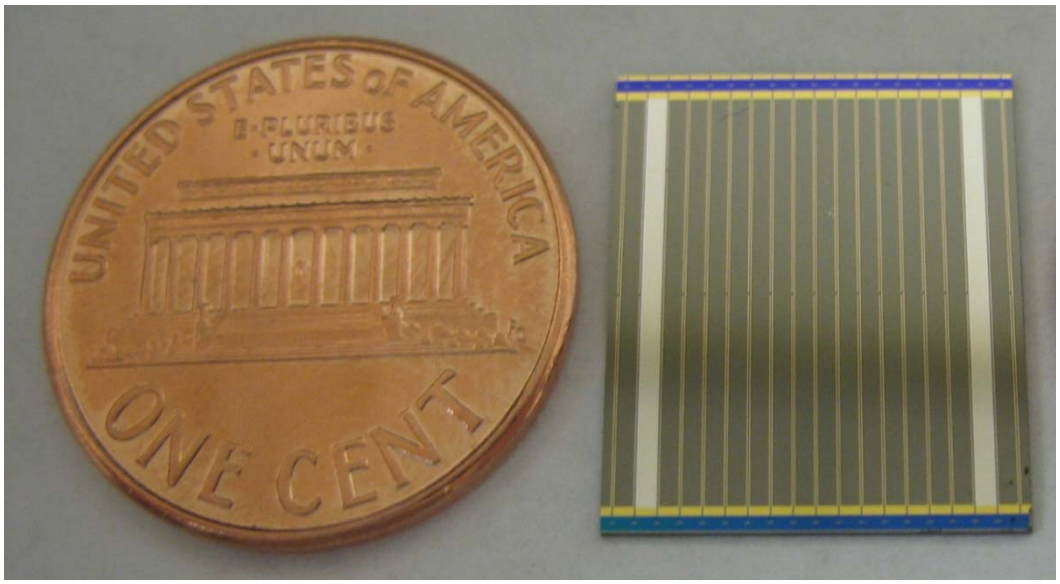

Fig. 2-15 Top view of a 1x16 Pt/4H-SiC Schottky photodiode array. The size of the array is 1.872 cm2. The two end "UV-blind" pixels are coated with Al.

2.2 Characteristics of 4H-SiC Schottky photodiodes

2.2.1 I-V characteristics

The dark I-V characteristics of Ni/4H-SiC Schottky photodiodes at room temperature are shown in **Fig. 2-16**. The optical window size is 5 mm × 5mm.

The thermionic emission theory predicts the current of Schottky metal/semiconductor contact to be:

$$I = A \cdot A^* \cdot T^2 \cdot \exp\left(\frac{-q\phi_B}{nk_BT}\right) \cdot \left[\exp\left(\frac{qV}{nk_BT}\right) - 1\right],$$

where A is the area of the diode, A^* the Richardson's constant, ϕ_B the barrier height, n the ideality factor, k_B Boltzmann's constant, q the electron charge, and T the

absolute temperature. The ideality factor is determined to be 1.06, and the Schottky barrier height is approximately 1.58eV, which is very close to the ideal barrier height (1.66eV) given by Itoh [45]. The leakage current is measured from 0 to -5 V using the Keithley 595 Quasi-static CV measurement system. The leakage current is less than 0.1 pA at -4 V. The dynamic resistance at 0 bias, *dV/dI*, is estimated to be $\geq 3 \times 10^{13}\,\Omega$.

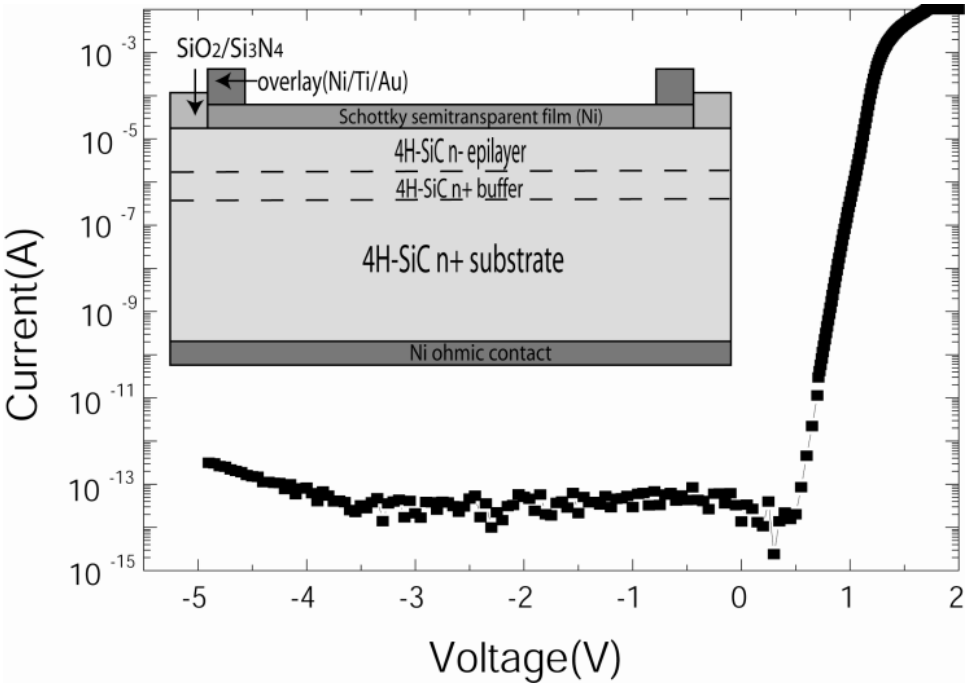

Fig. 2-16 Cross sectional view and I-V characteristics of Ni/4H-SiC Schottky photodiode.

The I-V characteristics of the Pt/4H-SiC Schottky photodiode with the same size as the Ni/4H-SiC photodiode are measured using a Keithley 4200 semiconductor characterization system at room temperature in dark. The thickness of the Pt semitransparent film is 1.5 nm. The I-V characteristics of the Pt/4H-SiC Schottky photodiode are shown in **Fig. 2-17**.

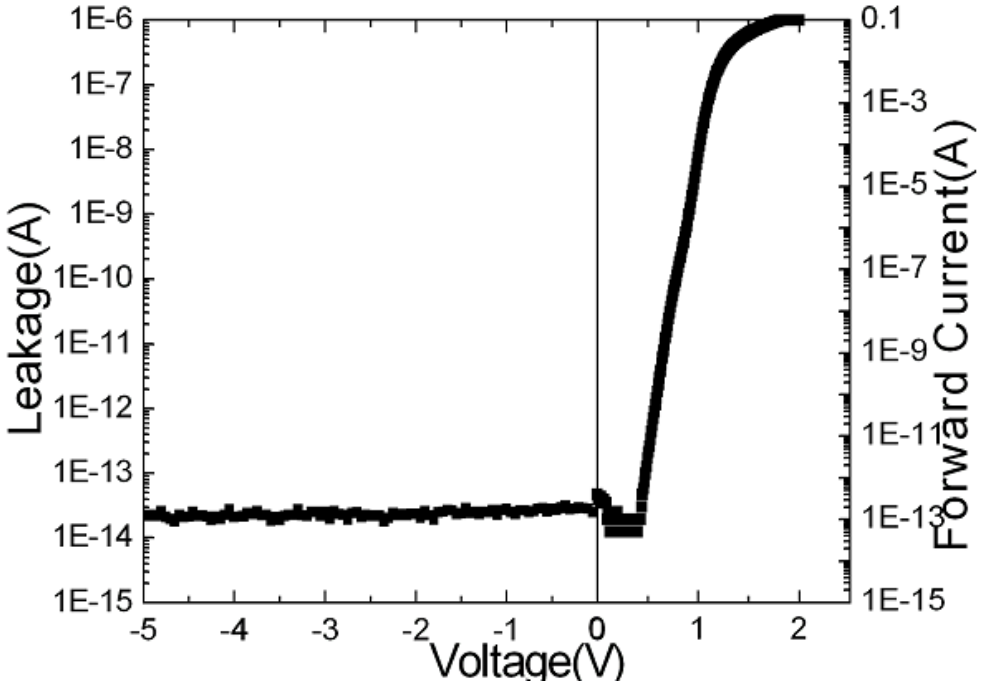

Fig. 2-17 I-V characteristics of Pt/4H-SiC Schottky photodiode.

The ideality factor of Pt/4H-SiC Schottky photodiode is determined to be around 1.10. The Schottky barrier height is approximately 1.56 eV and the corresponding work function of Pt is calculated to be 5.01 eV [46], which is lower than the accepted value of 5.65 eV. The difference is partially due to the inhomogeneous barrier height effect [47, 48].

Since the capacitance of the diode is relatively large and the input impedance of the instrument at ultra low current measurement at fA level is high, the settling time should be long enough to ensure the displacement current to be negligible [49]. The dark current is less than 20 fA at -5V. At lower bias, the actual leakage current should be lower than the measured value and a longer settling time should be chosen for the accurate current measurement.

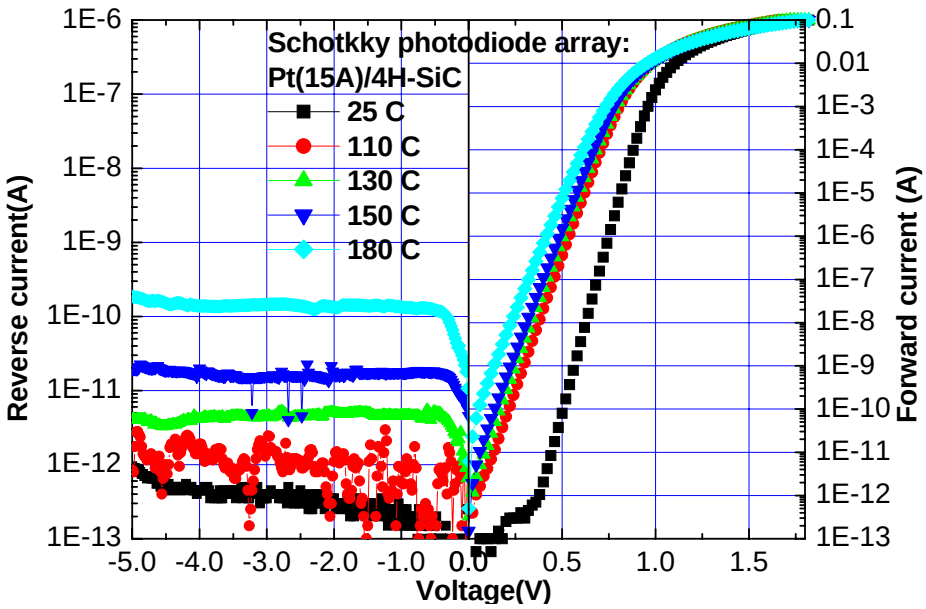

Fig. 2-18 I-V characteristics of Pt/4H-SiC Schottky photodiode from 25°C to 180°C

Fig. 2-18 shows the typical temperature dependence of the reverse I-V characteristics of the Pt/4H-SiC Schottky photodiode. As shown in the figure, the leakage current increases as the temperature increases from room temperature to 200 °C. When the temperature is less than 150 °C, the leakage of the Schottky diode is less than 20pA.

2.2.2 Quantum efficiency measurement

The photoresponse measurements of the Ni/4H-SiC Schottky photodiode from 3 nm to 380 nm are performed on the beamline X24C using the National Synchrotron Light Source (NSLS) at Brookhaven National Laboratory.

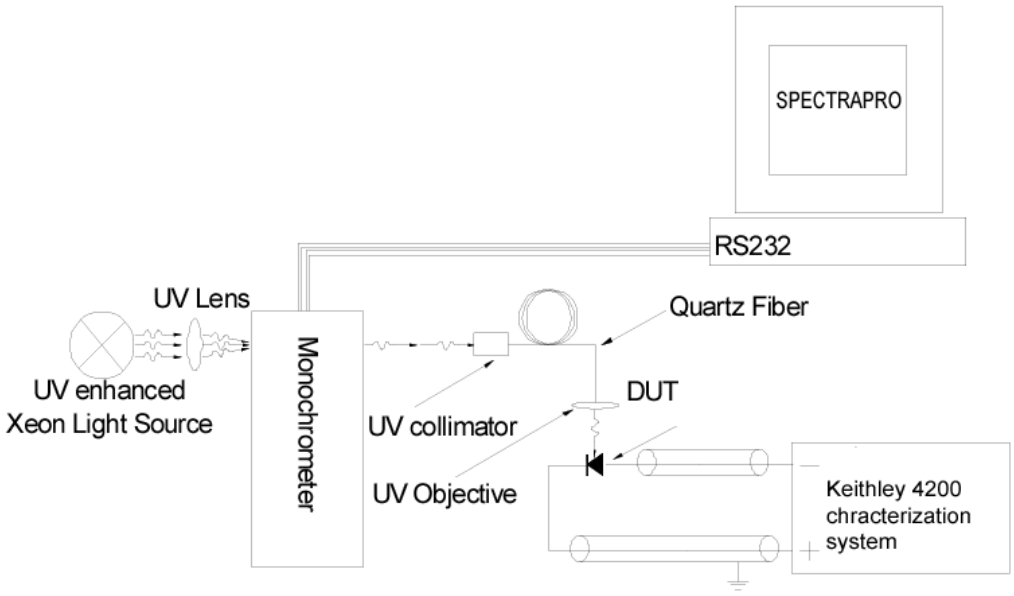

Fig. 2-19 Photoresponse measurement setup in the UV range from 200 nm to 400 nm.

A monochromator with interchangeable gratings of 150 g/mm, 600 g/mm and 2400 g/mm provided dispersed x-ray and EUV radiation with a resolving power of 500. The overall wavelength range of the gratings is approximately from 12 Å to the visible. Thin metal filters attenuated the higher harmonics from the monochromator while passing the X-ray or the EUV of interest. Removing the metal filter and setting the monochromator grating to the zero diffraction order allowed the photodiode to be illuminated by broadband radiation, which consists of all the wavelengths greater than ~1 nm. The photoresponse spectra from 200 nm to 400 nm are measured in air by using a Xenon lamp light source with a near UV monochromator shown in **Fig. 2-19**. And in all cases the beam spot is under-filled the detector.

The photoresponse spectra of the Ni/4H-SiC Schottky photodiodes are measured at 0 V bias. **Fig. 2-20** shows the measured external QE of two SiC photodiodes we fabricated. As comparison, the QE of an AXUV Si detector from International Radiation

Detectors Inc. is also shown in the plot. The QE of SiC Schottky photodiodes is <0.1% when the wavelength is higher than 380 nm because the incident photon energy is less than the bandgap of 4H-SiC. It increases gradually as the wavelength decreases and reaches a local maximum of 65% at 275 nm. The QE between 230 nm and 295 nm is higher than 50%. From 230 nm to 160 nm, the QE rapidly decreases as the wavelength decreases. And then it starts to rise when the wavelength is less than 160 nm except for the singular wavelength of 120 nm, where the QE of both SiC and Si photo detectors reach their local minima. The QE exceeds 100% at the wavelength shorter than 50 nm and finally reaches 30 electrons/photon at 3 nm.

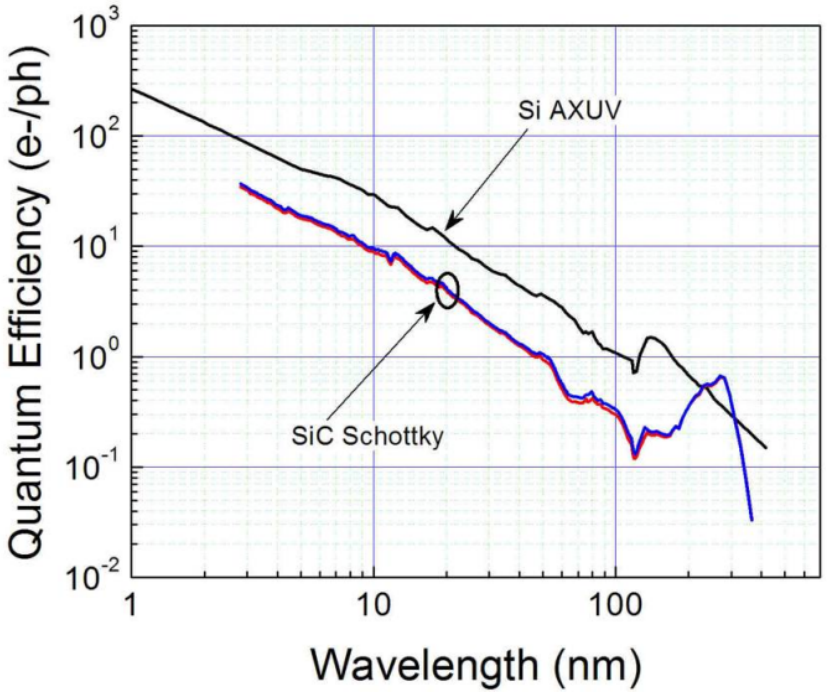

Fig. 2-20 Quantum efficiency of Ni/4H-SiC Schottky photodiode from 3nm to 400nm measured in Brookhaven National Laboratory.

The internal QE of the Ni/4H-SiC Schottky photodiode is investigated at the wavelength from 159 nm to 400 nm. The Fresnel coefficients of reflectance and

transmittance at the vacuum-Ni and Ni-SiC interfaces are calculated using the complex refraction index of the materials (Ni and SiC). As shown in **Fig. 2-21**, the radiation loss from 230 nm to 300 nm due to the reflectance and absorption of the 45 Å Ni film varies between 35% and 50%. At zero bias, the depletion width is about 1.7 μm and the corresponding internal QE between 230 nm and 300 nm is close to 100%.

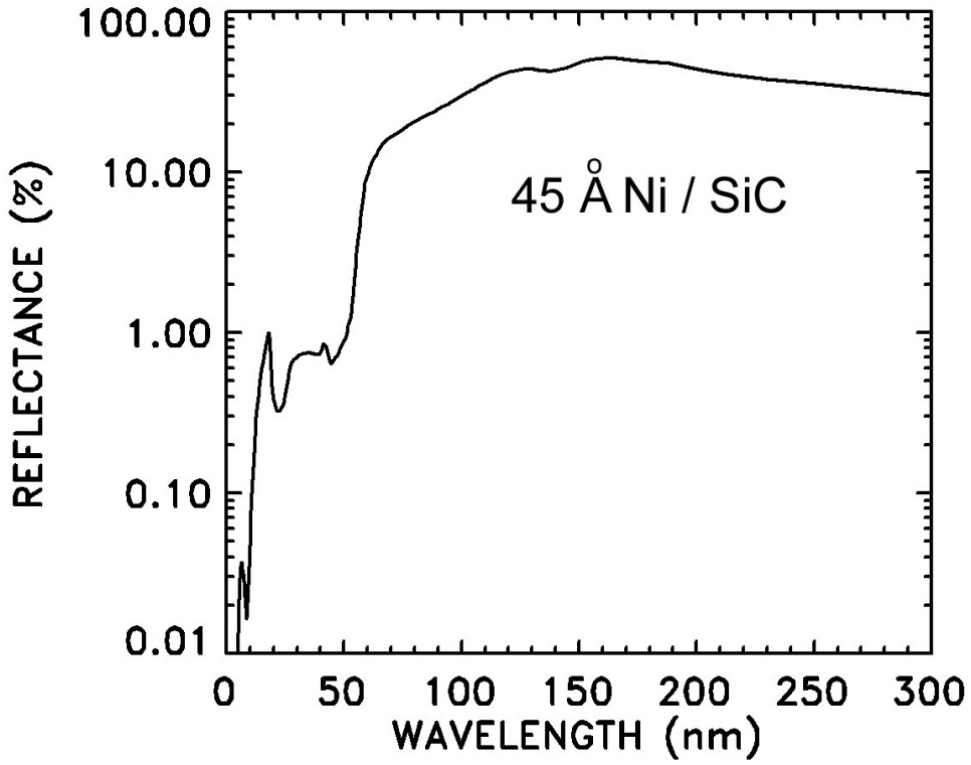

Fig. 2-21 Reflectance of UV light from 10 nm to 300 nm for the 45 Å Ni Schottky contact on 4H-SiC.

The SiC Schottky detectors show very good visible blindness. The QE at the wavelength of 390 nm is 0.034%, comparing with the peak QE of about 65% at 275 nm. The rejection ratio of UV to visible light is 2×10^{3}. The QE at 442 nm has also been calibrated to be 6.45×10^{-5} using a 20 mW He-Cd laser. The QE at 600 nm and 700 nm is estimated by projecting the tungsten-halogen lamp light through 600 nm and 700 nm

bandpass filters (bandwidth = 10 nm). The QE is as low as 10^{-5}. Considering the contribution of the UV light leaking through the optical filters, the actual QE at 600nm and 700nm should be substantially lower than 10^{-5}.

The decrease of the QE between the wavelength 230 nm and 160 nm is attributed to the dead zone effect introduced by the surface recombination, which becomes significant when the penetration depth starts to be comparable with the dead zone. In this wavelength range, a large portion of photons is absorbed in the dead zone, where the photon-generated carriers are recombined and have no contribution to the photo-response. The depth of the dead zone has been estimated based on the internal QE. At 200 nm, the external QE is 33%. Given that about 56% incident photons are reflected or absorbed by the 45 Å Ni semitransparent film at 200 nm, the internal QE is estimated to be around 75%. According to the optical properties of SiC reported by C. Cobet et al., the penetration depth of 4H-SiC at this wavelength is 11 nm, and the corresponding depth of the dead zone is about 3 nm. Based on this calculated depth of dead zone, at 160 nm the penetration depth is only around 4.2 nm, and the calculated QE is about 17%, which agrees very well with the experimental result of 18%.

The QE of SiC photodiodes starts to increase at 160 nm. Since the wavelength corresponds to the reported 4H-SiC pair generation energy W_{SiC} (7.8 eV), the increase is attributed to the multiple electron-hole pair generation. The QE spectra of Ni/4H-SiC photodiodes are quite similar to that of the Si photodiode between 3 nm and 120 nm. But the QE of Ni/4H-SiC is about a factor of three to five lower than that of Si photodiodes in this range. This difference is mainly due to the difference in pair generation energy for Si

(3.64 eV) and 4H-SiC, absorption in the 45 Å Ni film and the dead zone effect caused by the surface recombination.

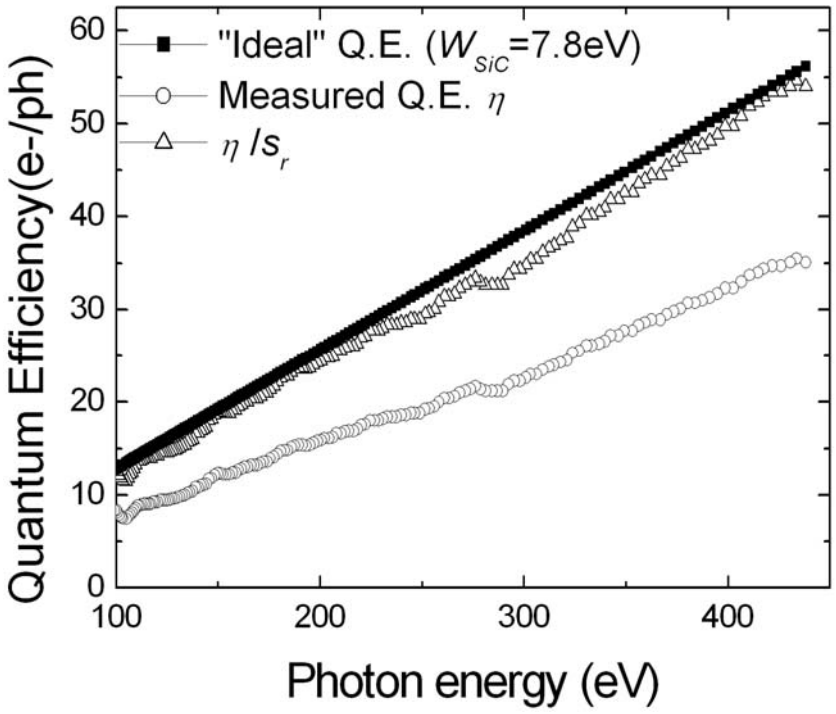

Fig. 2-22 Quantum efficiency of the Ni/4H-SiC photodiode from 100 eV to 420 eV.

The mean energy of electron-hole pair generation for 4H-SiC, W_{SiC}, is estimated from the QE spectra of Ni/4H-SiC photodiodes in the EUV region considering the losses due to the reflection and absorption of the 45 Å Ni film and the dead zone effect. **Fig. 2-22** shows the measured QE as a function of photon energy from 100 eV to 420 eV. In this spectrum region, one photon with high energy can generate multiple electron-hole pairs, and the QE is expressed as $\eta = s_r \frac{h\nu}{W_{SiC}}$, where s_r is a dimensionless factor, which describes the loss processes. For an "ideal" SiC detector without any losses, $s_r = 1$. For Ni/4H-SiC Schottky photodiodes, the average loss due to the reflection and absorption of the 45 Å Ni film and the dead zone effect is assumed to be about 35%. As a result,

around 65% incident photons contribute to the photocurrent, and the slope of QE vs. photon energy should be $0.65/W_{SiC}$. The mean pair generation energy of 4H-SiC, Ws_iC, is found to be 7.9 eV, in excellent consistence with the reported 7.8 eV that is measured in the X-ray spectrum.

A figure-of-merit, the spectral detectivity, D^* , is often used to evaluate the sensitivity of photo detectors. For the SiC Schottky photodiode working at 0 V bias, the dark current is very small and the Johnson noise dominates. In this case, $D^* = q\eta / hv \times (R_0 A / 4k_B T)^{1/2}$, where η is the QE, R_0 is the dynamic resistance at 0 V, A is the detector area and v is the photon frequency. At 275 nm where the maximum QE is achieved, the spectral detectivity is 3.4×10^{15} cmHz$^{1/2}$/W and the corresponding noise equivalent power， $NEP = (A\Delta f)^{1/2} / D^*$, is equal to 1.7×10^{-16} Hz$^{1/2}$/W. D^* over the wavelength range from 190 nm to 330 nm is above 10^{15} cmHz$^{1/2}$/W. As comparison, D^* of the Si AXUV detector is three orders lower.

The uniformity of the devices is also checked in the UV range. The spot size on the photodiode is less than 1 mm^2. The peak-to-peak variation of the quantum efficiency across the active area of the device is about ± 2%.

The photo-response of Pt/4H-SiC Schottky photodiode over wavelengths from 400 nm down to 7.5 nm is also investigated under photovoltaic mode at 0V bias, and in all cases the beam size under-fills the detector. The measurement from 400 nm to 260 nm is performed in air using an Oriel Xenon lamp with a monochromator as the UV source. Atmospheric molecular, oxygen, stratospheric ozone layer and other contaminants strongly absorb UV light with wavelength less than 260 nm. Therefore, the UV response from 260 nm down to 7.5 nm is measured in vacuum.

A deuterium arc lamp combined with an Action VM-502 monochromator is used as the UV light source for the measurement within the wavelength from 260 nm down to 120 nm. From 120 nm down to 7.5 nm, the UV photoresponse is measured in an extreme ultraviolet vacuum chamber consisting of a McPherson 247 grazing-incident monochromator and a windowless hollow cathode light as the EUV source. The Schueler-type lamp with a mixture of Ar and H gases produces strong continuous discharge ion-line sources in EUV range from 7.5 nm to 120 nm [50].

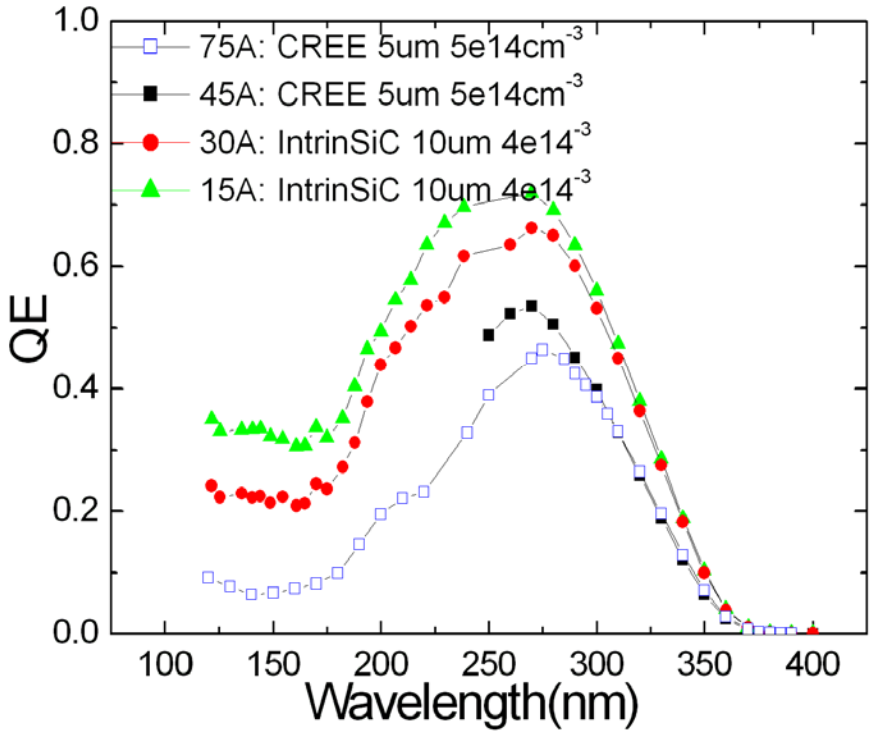

Fig. 2-23 Quantum efficiency of the Pt/4H-SiC Schottky photodiode from 120 to 400 nm.

The Quantum efficiency of the Pt/4H-SiC Schottky photodiode is investigated with different thickness of 4H-SiC n-type drift layer and Pt semitransparent film. **Fig. 2-23** shows that the QE of SiC Schottky photodiode increases as the Pt film becomes thinner. With 10 μm 4H-SiC n-type drift layer, at the wavelengths of 120 nm (280 nm), The QE increases from 24% (63%) to 35% (70%) when the Pt thickness decreases from 3

nm to 1.5 nm. It should be pointed out that the QE maximum in Near UV range does not change with the film thickness.

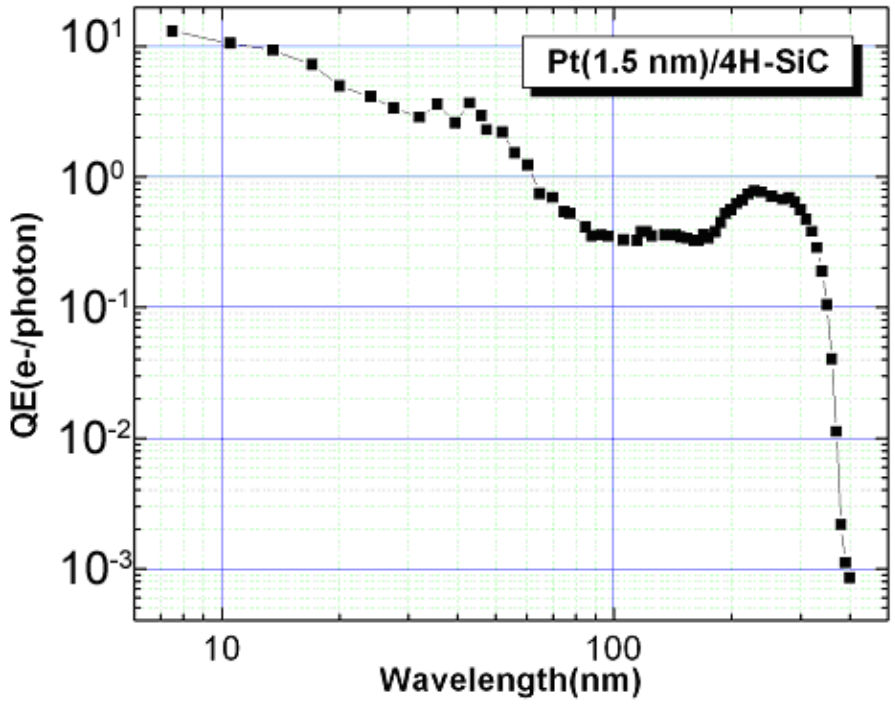

Fig. 2-24 Quantum efficiency of the Pt/4H-SiC Schottky photodiode from 400 to 7.5 nm

Fig. 2-24 shows the quantum efficiency of a 4H-SiC Schottky photodiode with 1.5 nm Pt Schottky contact from 400 nm to 7.5 nm. The QE of the SiC Schottky photodiodes is <0.1% at 400 nm because the energies of the incident photons are less than the band gap of 4H-SiC. This out-of-band visible-light rejection is highly desirable for many UV applications. The QE increases gradually as the wavelength decreases and reaches a local maximum of 78% at 230 nm. The QE between 190 nm and 310 nm is higher than 50%, owing to the ultra thin Pt film and the thick n- absorption layer.

At wavelengths shorter than 230 nm, the QE rapidly decreases as the wavelength decreases due to the surface recombination and the much shallower absorption length at this wavelength range. The QE then starts rising again at about 158 nm when the photon

energy exceeds the energy for a single electron-hole pair generation in the 4H-SiC. The QE exceeds 100% for the wavelengths shorter than 61 nm and finally reaches 13 electrons/photon at 7.5 nm.

For Pt/4H-SiC Schottky photodiode, at the local maximum of QE near 230 nm, the spectral detectivity, D^*, is 6.6×10^{15} cmHz$^{1/2}$/W and the corresponding noise equivalent power, $NEP = (A\Delta f)^{1/2} / D^*$, is equal to 6.0×10^{-17} W/Hz$^{1/2}$. D^* remains higher than 10^{15} cmHz$^{1/2}$/W as the wavelength decreases from 350 nm down to 7.5 nm.

2.3 Characteristics of 4H-SiC Schottky photodiode arrays

2.3.1 I-V characteristics

In order to meet the requirement of the Geostationary Operational Environmental Satellites (GOES) project, the shunt resistance, $R=dV/dI$, at room temperature should be higher than 3000 MΩ, and the dark current noise of the pixels of Schottky photodiode array, $(4k_BT/R)^{1/2}$, should be less than 2 fA at 1 Hz. When the array is working at photovoltaic mode under zero bias, the leakage current should be less than 10 pA.

The reverse I-V characteristics of the Pt/4H-SiC Schottky photodiode array are measured using Keithley 4200 SCS at room temperature in dark (**Fig. 2-25**). The leakage current is less than 50 fA when the reverse bias is less than 3 V.

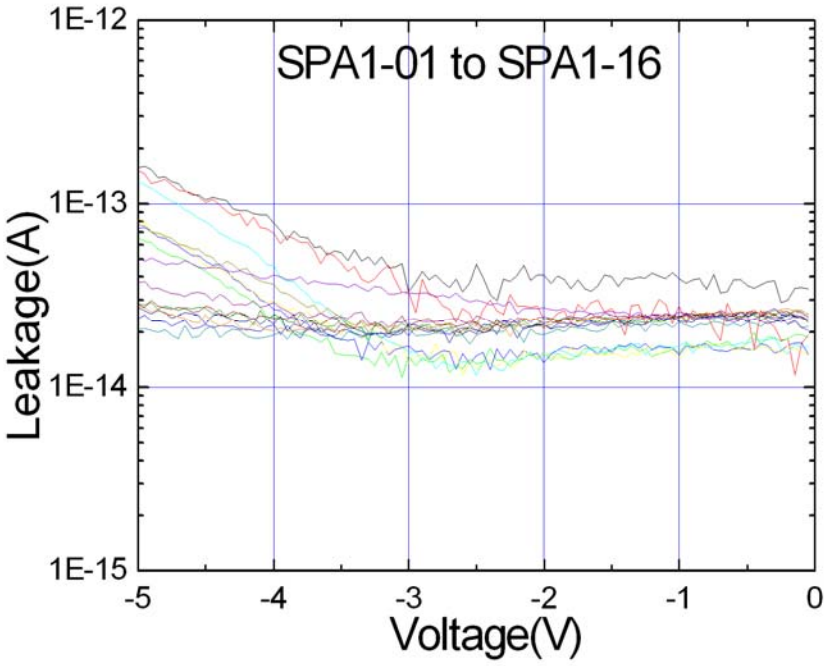

Fig. 2-25 Reverse I-V characteristics of the 1×16 Pt/4H-SiC Schottky photodiode array. The leakage current is less than 50 fA when the reverse bias is less than 3 V.

In order to determine the dark current of the Schottky photodiode array accurately, we measured the dark current of one pixel at the reverse bias of -0.1, -0.4, -0.8, -1.2, -1.6, -2, -2.5, -3, -3.5, 4, -4.5 and -5V. At each voltage, we scan the dark current for a long time to ensure the displacement current due to the high input impedance of the Keithley 4200 SCS and the large capacitance of the photodiode pixel with a large optical window to be negligible. The dark current is recorded when the reading becomes stable. At -0.4 V and -5V, the leakage current is 6.4 fA and 51 fA, respectively. The corresponding leakage current density is 55 fA/cm^2 at -0.4 V and 436 fA/cm^2 at -5 V. The dynamic resistance R_0 at 0 V is determined from $(dV/dI)_{V=0}$ to be $7.7\times10^{13}\,\Omega$.

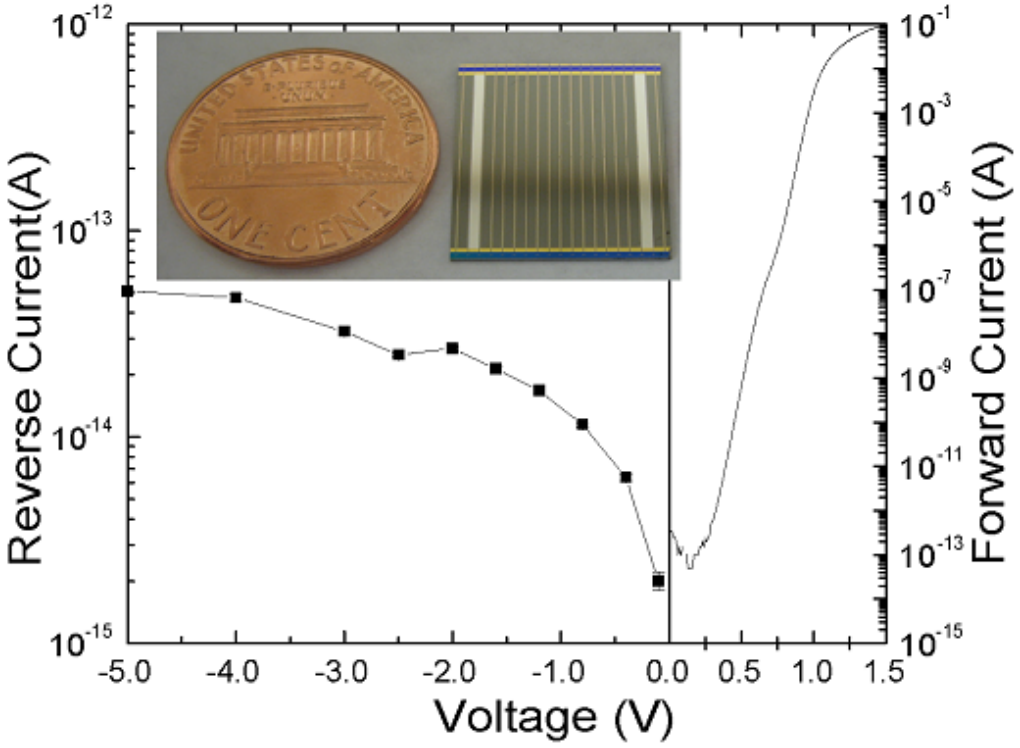

Fig. 2-26 I-V characteristics of one pixel in the Pt/4H-SiC Schottky photodiode array. The settling time is set to be long enough to make the displacement current negligible.

2.3.2 Cross talk characteristics

Crosstalk occurs when photo-generated carriers in one pixel junction diffuse a significant distance and be collected by an adjacent pixel. The crosstalk experiment is performed at the wavelength of 270 nm. The UV light spot is about 50 μm in diameter. Within the optical window, all the pixels show a uniform photo response with a variation less than 2% (**Fig. 2-27**). When the UV spot is focused at the center of one pixel, the photocurrent of the pixel is 80 times higher than that of the adjacent pixels. When the UV spot is located at the edge of the optical window of the pixel (position "A" in **Fig. 2-27**) and still fully focused in the window, the photocurrent is 42 times higher than that of the

adjacent pixel. The photocurrent of the pixel starts to drop when the UV spot moves away from the pixel.

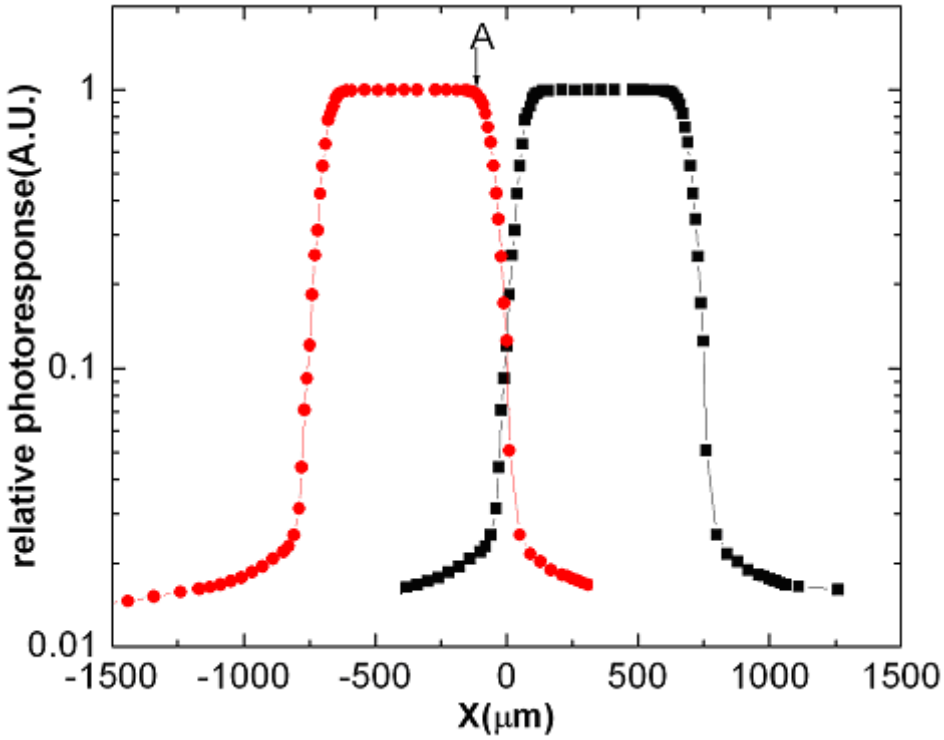

Fig. 2-27 Crosstalk measurement of 4H-SiC Schottky photodiode array.

2.3.3 Spectrographic characteristics

High QE and high sensitivity of our 4H-SiC Schottky photodiode array make it an excellent choice for low level EUV and UV detection applications. A UV spectrographic measurement using our 4H-SiC Schottky photodiode array is demonstrated. The setup is shown in **Fig. 2-28**.

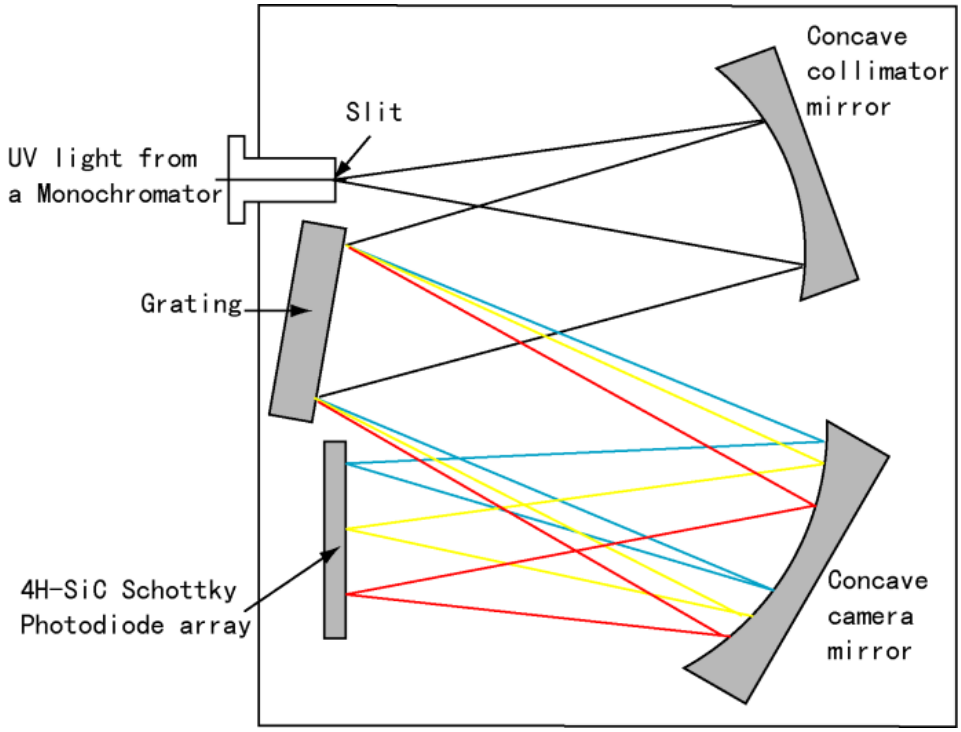

Fig. 2-28 Schematic UV spectrographic measurement setup using 4H-SiC Schottky photodiode array.

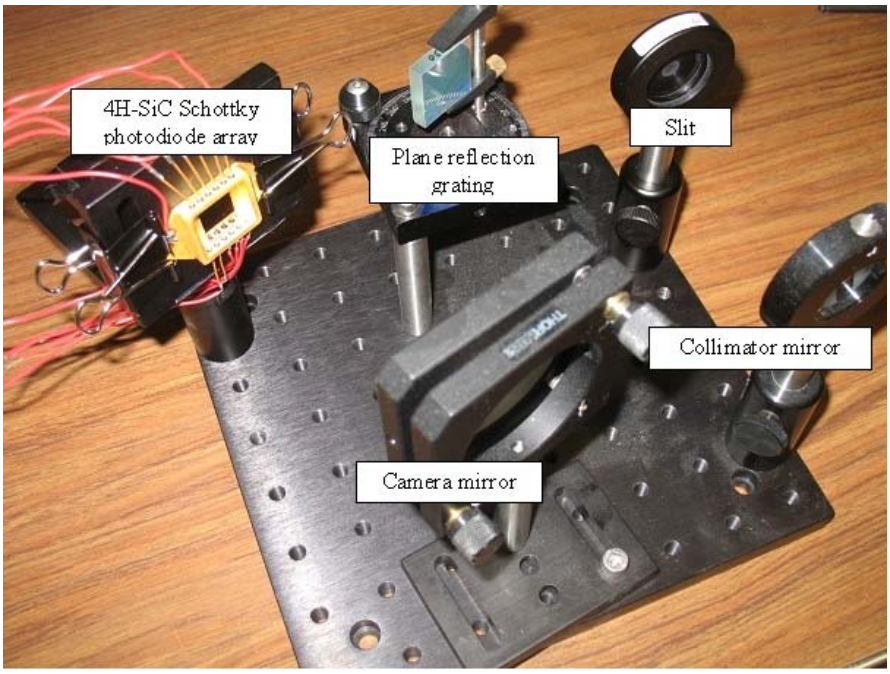

Fig. 2-29 UV spectrgraphic measurement setup using 4H-SiC Scottky photodiode array

The UV source is the monochromic UV light from a commercial monochromator so that the wavelength of the UV light incident to our spectrographic setup can be identified. The monochromic UV light is normal incident on the slit, which is 20 μm wide and placed at the focus of the concave collimator mirror. The UV light from the slit is collimated and then diffracted by a plane reflection grating with the groove density of 1200/mm and 2400/mm, respectively. The first order diffracted UV light is focused onto the photodiode array by a concave camera mirror with a focal length, f = 10 cm. **Fig. 2-29** shows the photo of the experimental setup for the spectrographic measurement.

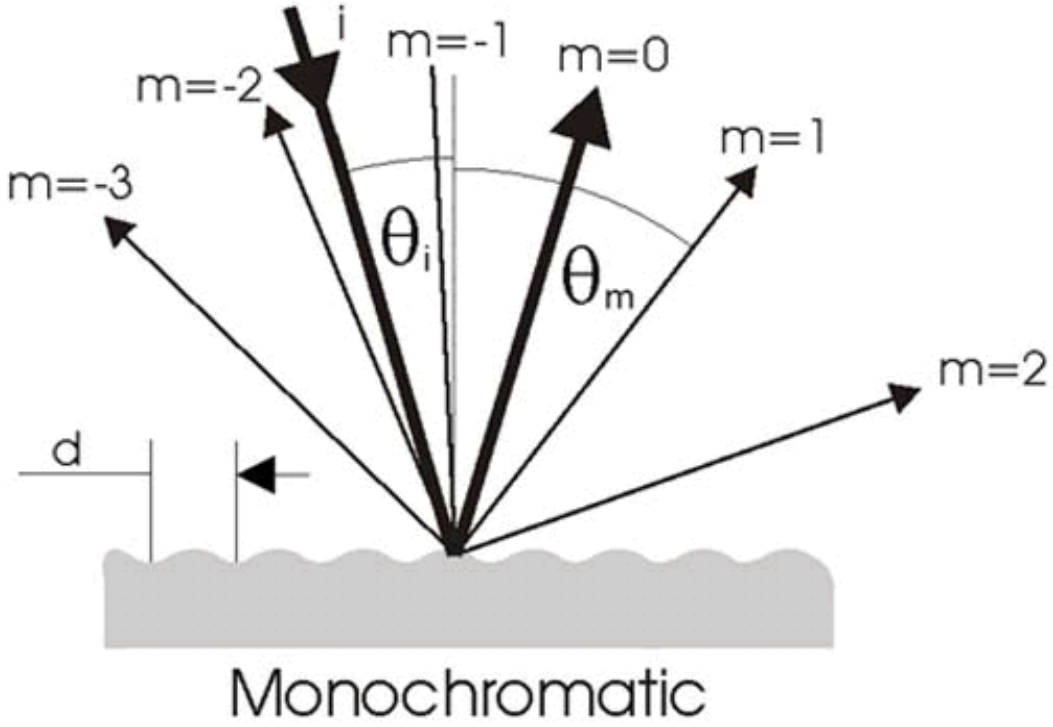

Fig. 2-30 Angular separation for monochromatic radiation caused by a grating.

The basic grating equation is:

$$\sin\theta_m = \sin\theta_i + m\frac{\lambda}{d},$$

where θ_i and θ_m are angles of the incident and diffracted wave directions to the normal of the grating surface;

λ is the wavelength;

d is grating period;

m is the order of diffraction (integer value, m = 0, 1, 2, ...).

This equation is valid for reflection gratings, whose grooves are perpendicular to the plane of incidence. Gratings in spectrometers are mostly used in reflectance mode. The equation shows that for the m-th order radiation, reflected light with different wavelengths is separated angularly. This effect is called dispersion. Spectrometers normally use the first order dispersed light. Influences of other orders and the non dispersive zero order must be suppressed. **Fig. 2-30** shows the angular separation for a monochromatic radiation, caused by a grating.

When the UV spectrographic system is working at the wavelength around 350 nm with normal incidence ($\theta_i=0^o$), the angle of the first order dispersed light is dependent on the groove density of the reflection grating. For d=1/1200 mm, the first order dispersed angle, $\theta_1=24.9^o$. If d=1/2400 mm, $\theta_1=57.1^o$

The linear dispersion of a spectrographic system is defined as:

$$\frac{dl}{d\lambda} = \frac{f \cdot m}{d \cdot \cos\theta_m},$$

where f is the focal length, m the order of diffraction, d the groove period, and θ_m the diffraction angle. With a normal incident angle, the diffraction angle and the linear dispersion at 350 nm are calculated to be 24.9^o and 1.32 mm/nm, 57.1^o and 0.46 mm/nm, respectively.

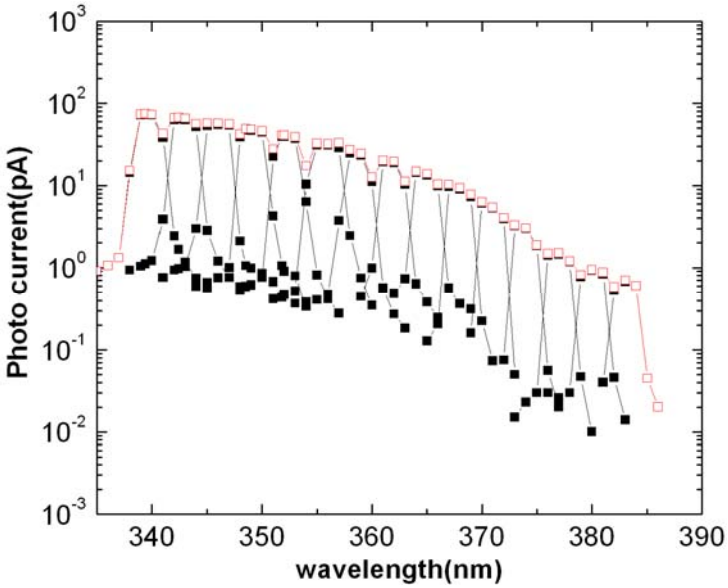

Fig. 2-31 Spectrographic result from 340 nm to 390 with a 1/1200 mm grating.

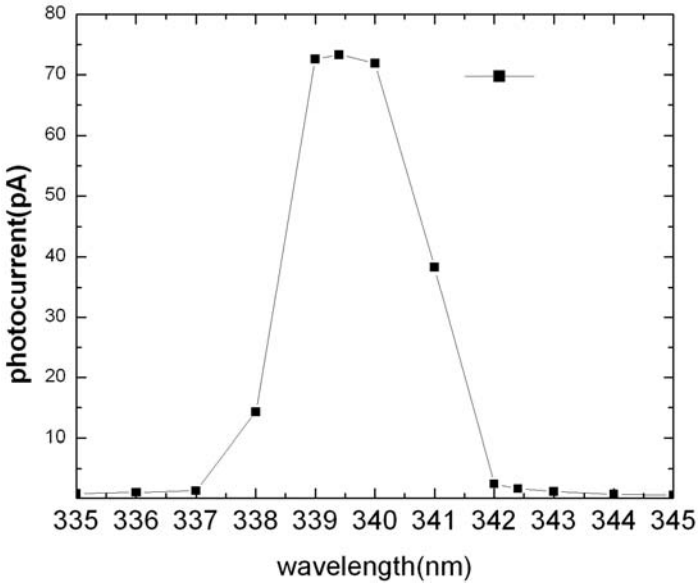

Fig. 2-32 The photocurrent of one pixel in detail with a 1/1200mm grating. The dispersion resolution is 3.0 nm/pixels

Spectrographic measurement is performed with 1/1200 mm and 1/2400 mm gratings, respectively. **Fig. 2-31** shows the spectrographic result with the 1/1200 mm grating from 340 nm to 390 nm. **Fig. 2-32** shows the photocurrent of one pixel in detail.

The pulse width at the half-height of the photocurrent is 3.0 nm, and the dispersion resolution is 3.0 nm/pixels.

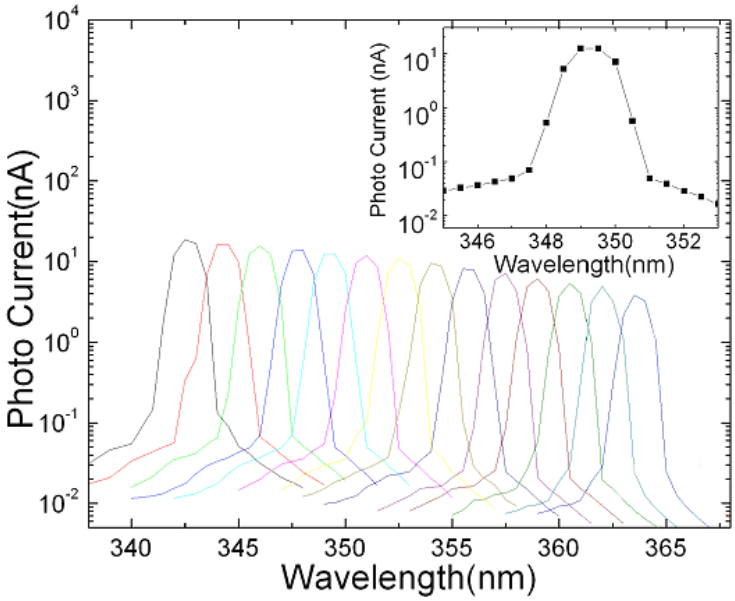

Fig. 2-33 Spectrographic result from 342 nm to 366nm with a 1/2400 mm grating.

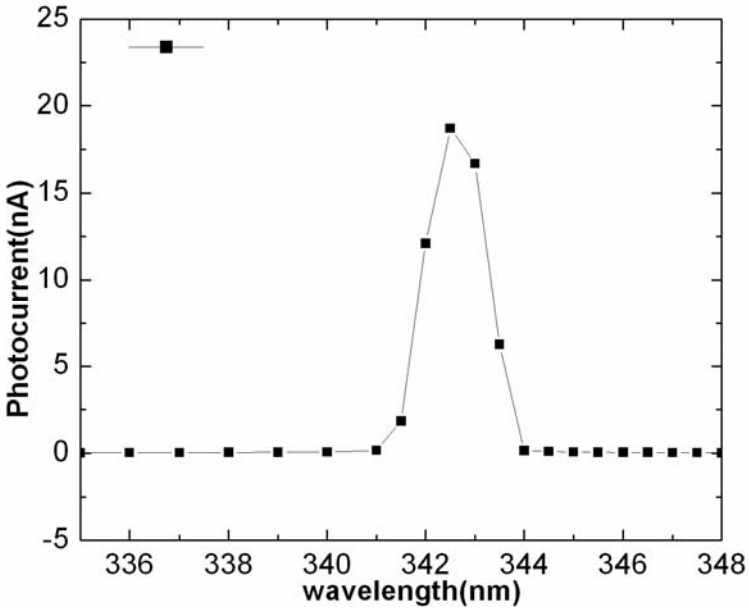

Fig. 2-34 Photocurrent of one pixel in detail with a 1/2400mm grating. The photocurrent pulse width at the half-height is 1.6 nm.

With the groove density of 1/2400 mm, the spectrographic system covers wavelengths from 342 nm to 366 nm, and the result is shown in **Fig. 2-33**. The corresponding sampling resolution is 1.6 nm/pixel. According to the linear dispersion equation, the linear dispersion resolution, $dl/d\lambda$, is inversely proportional to the grading period, d, which means that the sampling resolution of the spectrographic system with d=1/2400 mm should be twice of that with d=1/1200 mm. It fits very well with our measured results shown in **Fig. 2-32** and **Fig. 2-34**. The spectroscopic system resolution is determined by the linear dispersion and resolution of the optics as well as the internal resolution of the detector and the sampling size of the pixels. For sensor-limited resolution, the photodiode pixel width can be reduced from our current 750 μm to 40 μm and the number of the pixels can be increased to keep the total detection area the same. Potentially, a dispersion of 0.08 nm/pixel with a corresponding 2-pixel resolution of 0.16 nm can be achieved. Moreover, the leakage current per pixel of the SiC photodiode array will also decrease significantly, since it scales with the Schottky contact area.

Chapter 3 4H-SiC Single photo avalanche diodes

3.1 Design of 4H-SiC Single photon avalanche diodes

4H-SiC sinlge photon avalanche photodiodes (SPADs) have excellent potential for UV detection applications in which high gain and high speed are required. This section presents the guidelines for the avalanche diode design for single photon counting detection:

(a) High optical gain and very low dark count rate: When 4H-SiC avalanche photodiodes are operating at the Geiger mode, the gain should be larger than 10^6, which is often achieved at the excess voltage of 3-4 V higher than the breakdown voltage. Whereas the dark count rate is not negligible. According to our experiments, the dark count rate scales with the dark current to some degree. To decrease the dark current is an effective way to improve the performance of 4H-SiC single photon avalanche photodiodes.

(b) Edge termination: SiC has a very high critical field of 2MV/cm~5MV/cm. To guarantee the device can work under the Geiger mode without surface breakdown, edge termination is critical to eliminate the electric field crowding at the edge and allow 100% bulk avalanche breakdown.

(c) Uniformity: When SPADs are working under the Geiger mode with the gain higher than 10^6, 0.1V difference over the p-n junction will cause a huge non-uniformity of gain, which will degrade the detection efficiency. Good ohmic contact will improve the uniformity of the gain over the junction.

3.1.1 Device structure design

The schematic cross sectional view of 4H-SiC SPADs is shown in **Fig. 3-1**. The 4H-SiC SPADs have on-mesa or off-mesa overlay according to the different design. With the same optical window, the process of the on-mesa overlay structure is relatively easier than the off-mesa overlay structure. However, the on-mesa overlay structure occupies a larger p-n junction area which may have higher dark current and lower yield. The off-mesa overlay structure has its overlay on the dielectric layer. The process is more complicated and the dielectric layer should be thick enough to prevent the breakdown through the dielectric.

The dark current of 4H-SiC SPADs is generated by the dark carriers under high electric field when the SPADs are working under the Geiger mode. 4H-SiC SPADs are designed with a P-i-N structure instead of a PN junction. By inserting the i- layer, the performance of 4H-SiC SPADs can be improved in the following aspects:

a) High quantum efficiency: The i-layer increases the thickness of absorption layer. More photons can be absorbed.

(a) Low leakage current: High electric field at the device edge may lead to high peripheral leakage current. With the i-layer, the critical field at the breakdown voltage drops a lot, and the peripheral leakage current can be significantly reduced.

(b) Low dark count rate: With a lower critical field at the avalanche breakdown, a lower dark count rate can be achieved owning to the reduced dark carrier population.

(c) Low excess noise: The excess noise is determined by the ionization ratio of α/β. The ratio of α/β decreases with the decrease of the critical electrical field, indicating the low doped drift layer can suppress the excess noise.

(d) High frequency: The junction capacitance can be reduced with the i-layer, therefore, the recovery time of the SPADs, which is determined by RC time constant, can be reduced, and the SPADs can work at higher frequency.

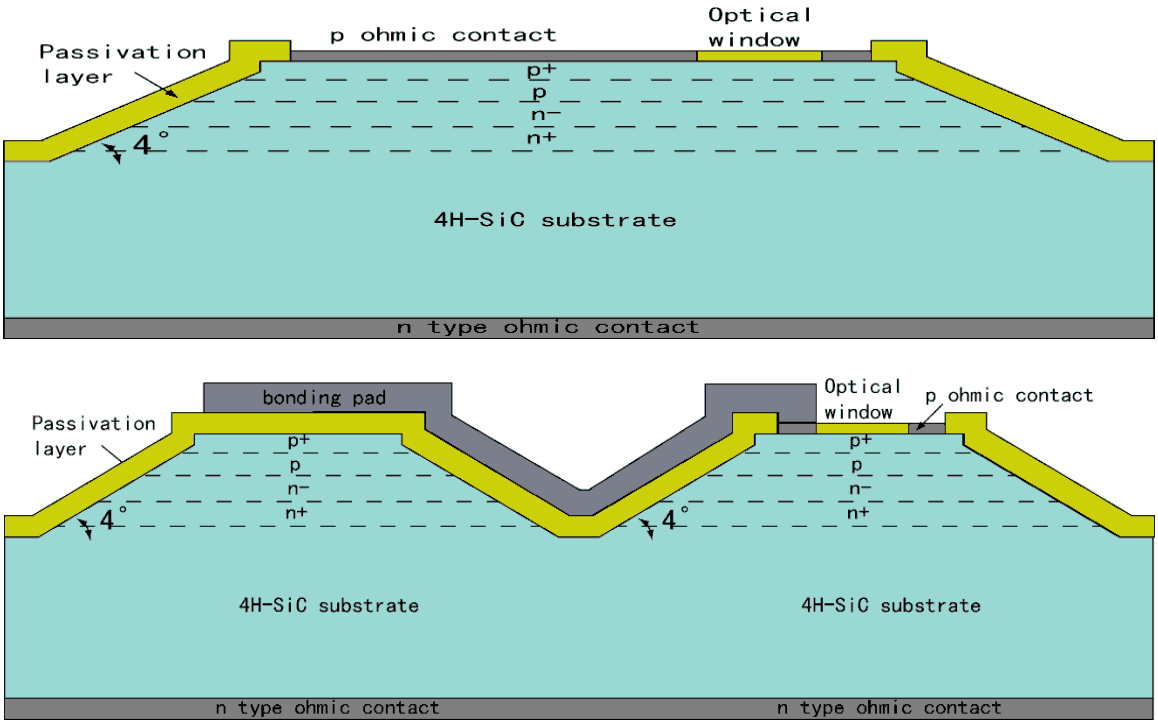

Fig. 3-1 Cross sectional view of 4H-SiC single photon avalanche diodes.

3.1.2 Edge termination design

Edge termination is very critical for SiC avalanche photodiodes. It is used to eliminate the electric field crowding at the device edge in order to avoid surface breakdown. In addition, Good edge termination can reduce the peripheral leakage current

at high electric field stress. Many edge termination technologies, including planar field, guard rings, junction termination extension, and positive or negative bevel edge termination, have been developed for SiC high power devices. People often classify them into two types, planar edge termination and mesa edge termination. Planar edge termination is often formed by ion implantation, which is the only selective area doping technology practically for SiC. The ion implantation energy of the dopants for SiC is much higher than that for Si for the same doping depth and the activation efficiency of ions is hard to control. In addition, the post implication annealing temperature of SiC is higher than Si, which introduces the surface roughness and further results in a higher leakage current. Another disadvantage is that the lattice damage due to the implantation cannot be completely recovered by high temperature annealing. Therefore, high leakage current and edge breakdown make the planar edge termination unfeasible for 4H-SiC SPAD fabrication.

Mesa edge termination includes multiple junction termination extension (MJTE) and bevel edge termination. Multiple junction termination extension shown in **Fig. 3-2** is formed by inductive coupled plasma (ICP) dry etching using Al as etching mask. Firstly, the outmost one or two shallow JTEs are etching with the step of 200 to 300 Å. The etching depth of the inner most JTE should be controlled very carefully until the edge of an epitaxial *p*-*n* junction forms a thin *p* layer, which is completely depleted when the breakdown occurs. Due to the high resistance of the *p*-layer after depletion, the voltage drop across the junction is reduced at the edge and the surface electric field can therefore be substantially reduced. In this case, the etching depth of the inner most JTE is very critical because over etching or under etching of the inner most JTE will cause surface

breakdown. In real device fabrication, The MJTE etching is carried out before the device passivation, in which damages on the device surface are removed and a thin SiC layer (normally 500 to 600 Å) is consumed. Therefore, a margin should be left during the ICP etching before the inner most JTE reaches its optimized step.

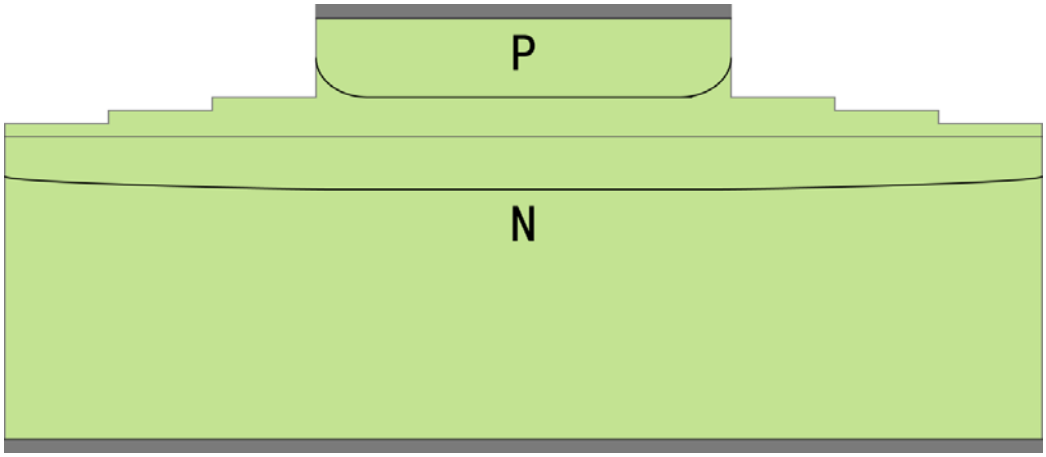

Fig. 3-2 Schematic diagram of multiple step junction termiation extension.

Another mesa edge termination is bevel edge termination. Compared with the other edge termination technologies, the bevel edge termination is the most feasible approach for SiC avalanche photodiodes to eliminate the electric field crowding and allow 100% bulk avalanche breakdown. Bevel edge termination can be classified into positive and negative bevels. **Fig. 3-3** shows a *p*-*n* junction terminated by a positive bevel edge termination.

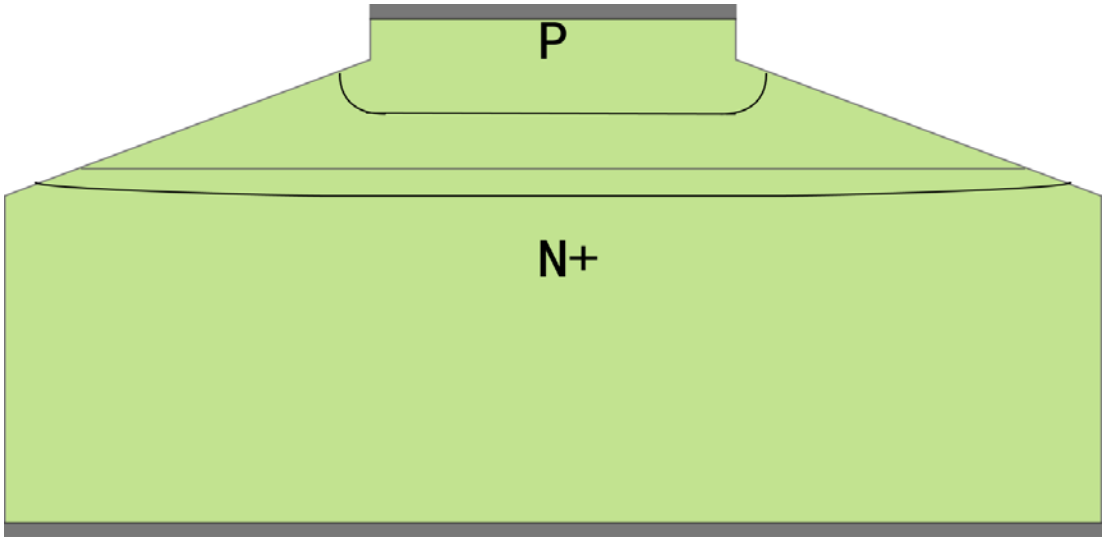

Fig. 3-3 Schematic diagram of a positive bevel edge termination.

The area of the junction decreases from the heavily doped side to the lightly doped side for the positive bevel edge termination. In order to maintain a charge balance on the opposite sides of the junction, the depletion layer on the lightly doped side of the junction is forced to expand near the surface. This expansion of depletion layer causes a reduction in the electric field at the surface. Since the depletion layer width along the surface is much larger than in the bulk, it can be concluded that the electric field along the surface will be much smaller than in the bulk, which ensures bulk breakdown prior to surface breakdown.

If the edge of the junction is cut in the opposite direction so that the area of the junction increases when proceeding from the highly doped side towards the lightly doped side, the termination is called negative bevel junction. The depletion layer shape for this case is illustrated in **Fig. 3-4**.

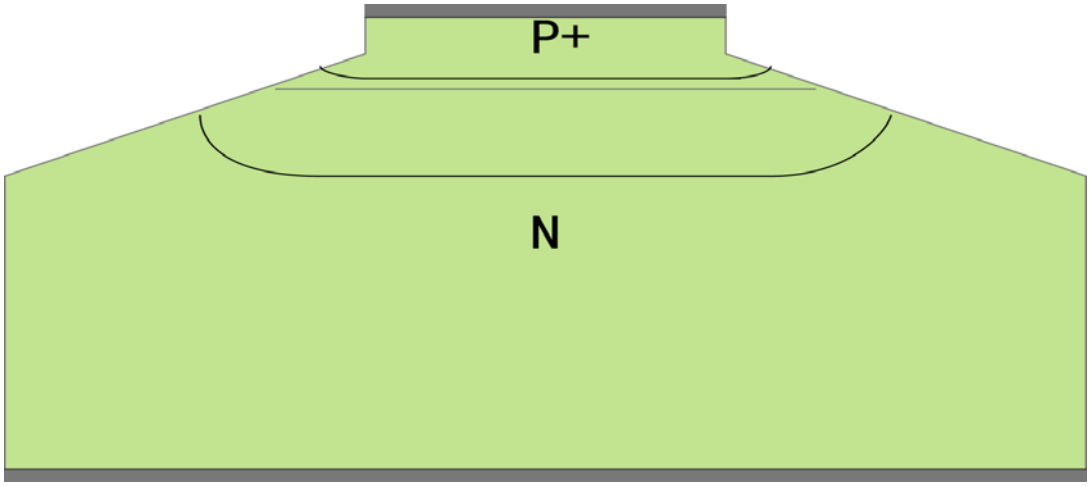

Fig. 3-4 Schematic diagram of a negative bevel edge termination.

The establishment of charge balance on the opposite sides of the junction causes the depletion layer at the surface of the lightly doped side to decrease while the depletion layer on the heavily doped side expands. The depletion layer shrinkage on the lightly doped side will have the dominant influence. Since the reverse bias across the junction is being supported across a narrower depletion layer at the surface than in the bulk, the electric field at the surface is higher than in the bulk. Consequently, surface breakdown will precede bulk breakdown in the negative bevel.

However, when a very shallow negative bevel angle is created, the argument is no longer valid because the surface depletion width can be increased as illustrated in **Fig. 3-5**.

The large amount of material removed from the p+ side forces the depletion layer to expand considerably along the surface on the p+ side. It should be pointed out that the depletion layer on the lightly doped side gets pinned to the metallurgical junction edge at the surface under this circumstance and the expansion of the depletion layer on the p+

side of the junction lowers the surface electric field. When the negative bevel angle is made very small, the maximum surface electric fiend becomes less than in the bulk.

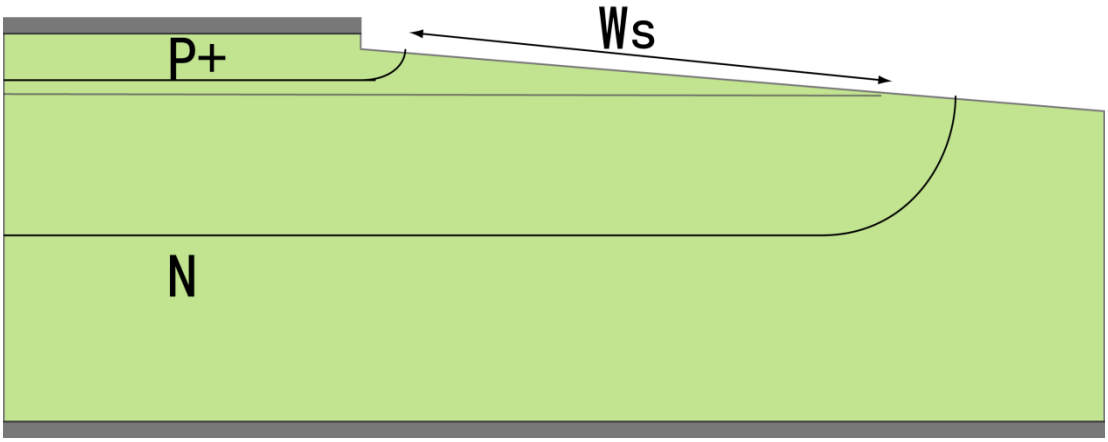

Fig. 3-5 Schematic diagram of a shallow negative bevel edge termination.

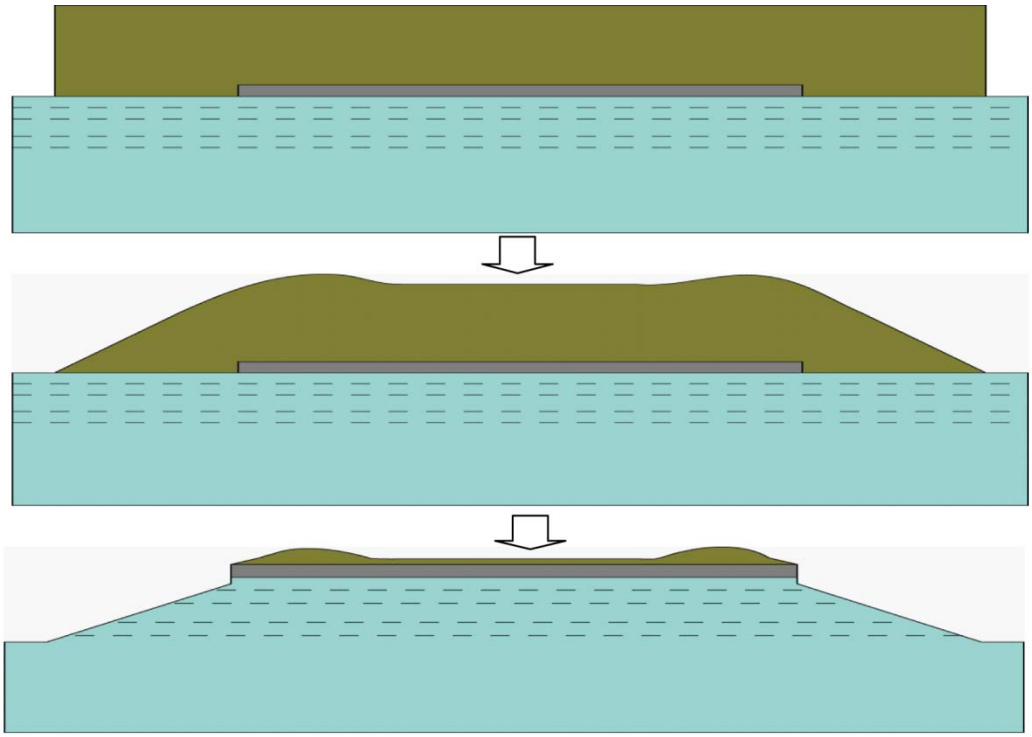

Fig. 3-6 Schematic diagram of SiC bevel formation

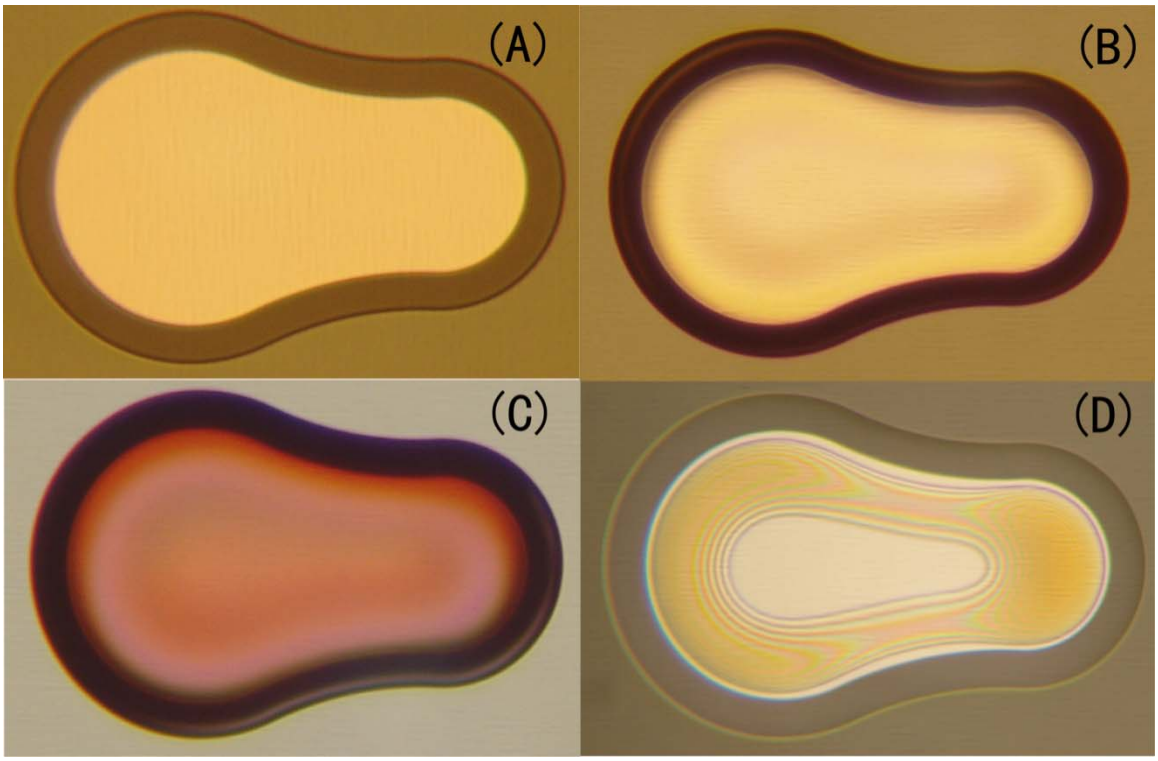

Fig. 3-7 photos of the bevel edge termination formation. (A) shows the pattern thick photoresist before hard bake; (B) shows the PR bevel after hard bake; (C) shows the PR bevel after electron-beam curing; (D) shows the SiC bevel after ICP etching.

Fig. 3-6 shows the schematic fabrication process of SiC bevel. In order to prevent the plasma etching damage to the mesa top surface, A 300 nm Al is deposited and a photolithography using a thin photo-resist (PR) is performed to define the top mesa pattern. Then the sample is hard baked to condense the PR. Al is selectively etched by Al etchant II and the SiC surface is exposed except the mesa top.

Then, a thick PR，AZ4620，is spun on the sample. The thickness of the PR is very sensitive to the spin speed and temperature. After photolithography, the patterned thick PR is shown in **Fig. 3-7**(a). Normally, the thickness of the PR is about 7 μm at 22^{o}C.

The PR is baked in a hot oven. As a result, a beveled edge is formed on the patterned PR shown in **Fig. 3-7**(b). The angle of the PR bevel can be controlled by the baking time and temperature. After hard baking, The PR is condensed by an electron-beam curing (**Fig. 3-7**(c)). An ICP etching is performed using the beveled PR patterns as etching mask and the bevel on the PR is transfer to the SiC. Since the etching rate of SiC is much slower than that of the condensed PR in the ICP etching, a SiC mesa with a shallow bevel can be achieved (**Fig. 3-7**(d)).

The surface quality of the etched bevel is very sensitive to the ICP substrate temperature, the sample size, and the etching gas flow rate according to our experiments.

1. ICP substrate temperature:

   We try the bevel etching in two ICP etching systems. One ICP system has a water cooled substrate, and the other one does not. The etching condition is shown in **Table 3-1**.

Table 3-1 ICP Etching condition for SiC bevel formation

Base Pressure	Etching gas	Gas flow rate	DC bias	RF power
10 mTorr	CF_4 only	5 sccm	50 V	700 W

When the SiC bevel is etched on the substrate without the water cooling system, the ICP chamber is heating up during the etching and the substrate temperature increases with the etching time. After 10 minute ICP etching, we find from **Fig. 3-8** that the etched PR surface and SiC bevel surface are very rough. As comparison, Another SiC sample with the same size is etched on a water cooled substrate under the same condition for 19 minutes. Both of the etched PR surface

and the etched SiC bevel surface are very smooth. The reason is that the ICP dry etching of photo resist at high temperature will leave organic residues on the surface.

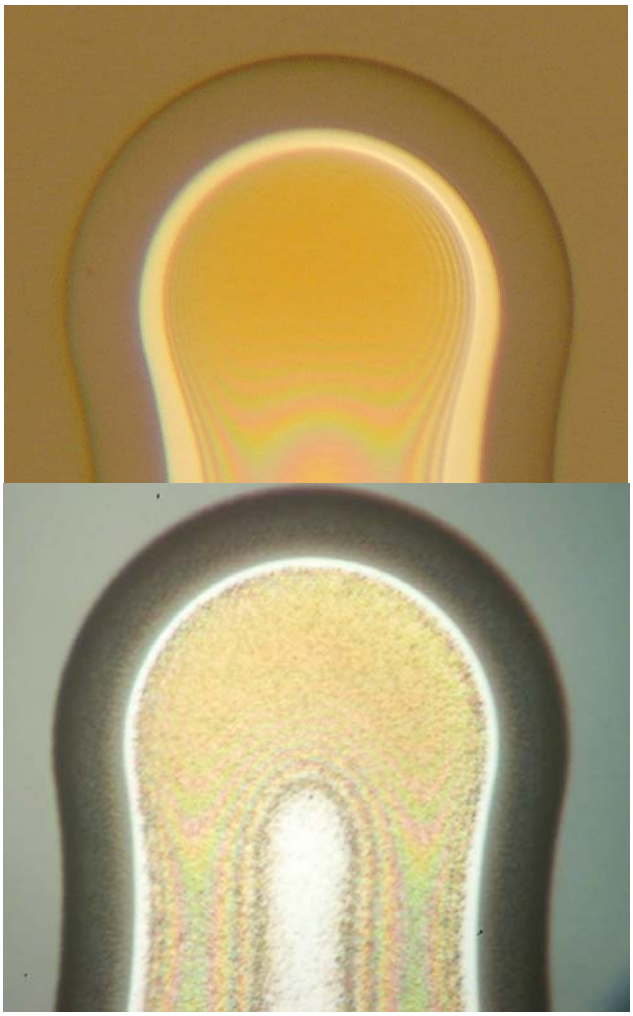

Fig. 3-8 SiC bevel etched on the substrate with and without water-cooling. The top photo shows a very smooth SiC bevel etched on a water-cooled substrate. The bottom one shows a rough SiC bevel etched on a substrate without water-cooling.

2. Sample size:

Two samples with different size of 40 mm^2 and 400 mm^2 respectively, are prepared simultaneously. The bevel etching is done under the same etching

condition shown in Table 3-1 ICP Etching condition for SiC bevel formation. The SiC bevel surface after dry etching shown in **Fig. 3-9** reveals that the surface of the smaller sample is much better than that of the larger sample.

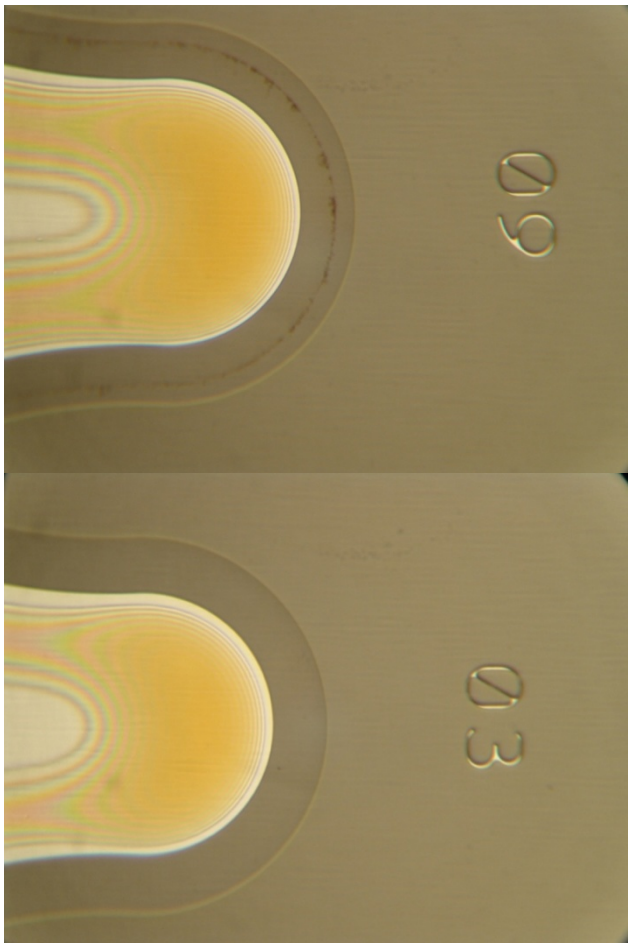

Fig. 3-9 SiC bevel surface on two samples (40mm^2 and 400mm^2) after dry etching with the same condition. The smaller sample has much better bevel surface.

3. Etching gas flow rate:

Five pieces cut from one sample with the same size of 40 mm^2 are dry etched under the same condition except the CF_4 gas flow rate, The CF_4 flow rate decreases from 60 sccm down to 5 sccm. **Fig. 3-10** shows the etched bevel surfaces of 4H-SiC at the CF_4 flow rate of 60 sccm and 5 sccm, respectively. We

find that at the reduced CF_4 flow rate of 5 sccm, the bevel quality is good, the etching rate of 4H-SiC is 56.7nm/sec, and the selectivity of the PR etching rate to SiC bevel etching rate is 4.6:1 (**Fig. 3-11**). We try to further reduce the CF_4 flow rate. However, when the flow rate is less than 5 sccm, the plasma during the ICP etching is unstable. Therefore, The SiC bevel etching should be performed at 5 sccm owning to better bevel surface and higher SiC etching rate.

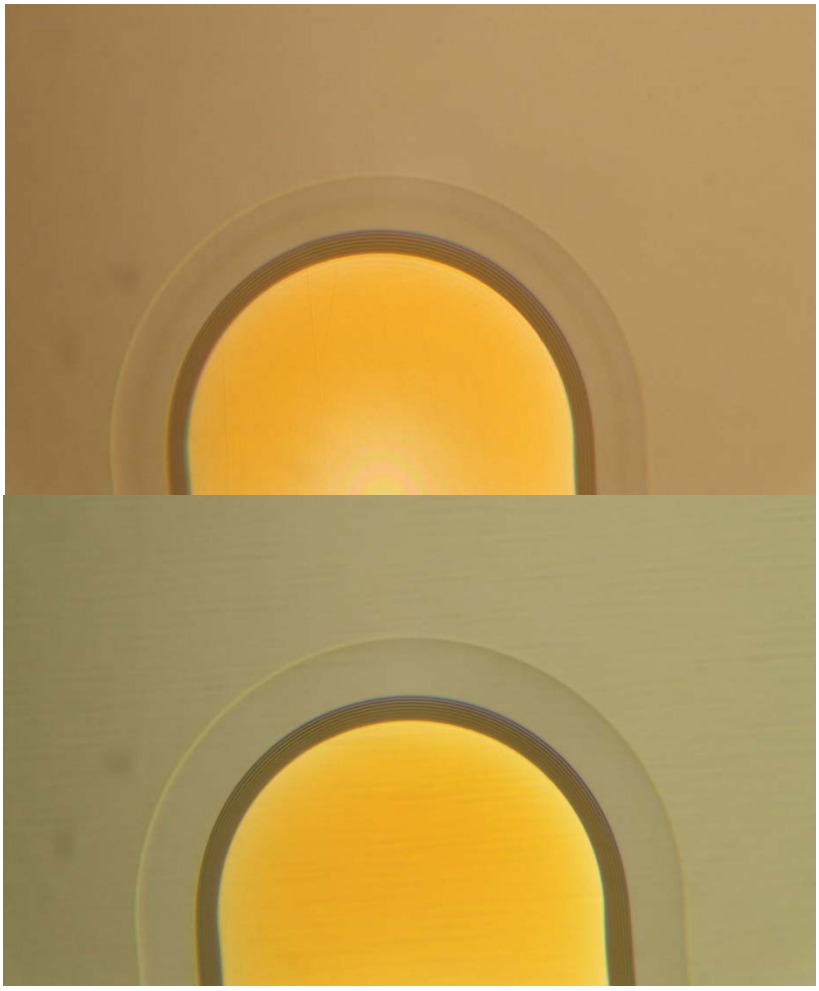

Fig. 3-10 SiC bevel surfaces with CF4 flow rate of 60sccm and 5sccm, respectively. The top one shows a rough surface etched at 60 sccm. The bottom one shows a smooth surface etched at 5 sccm.

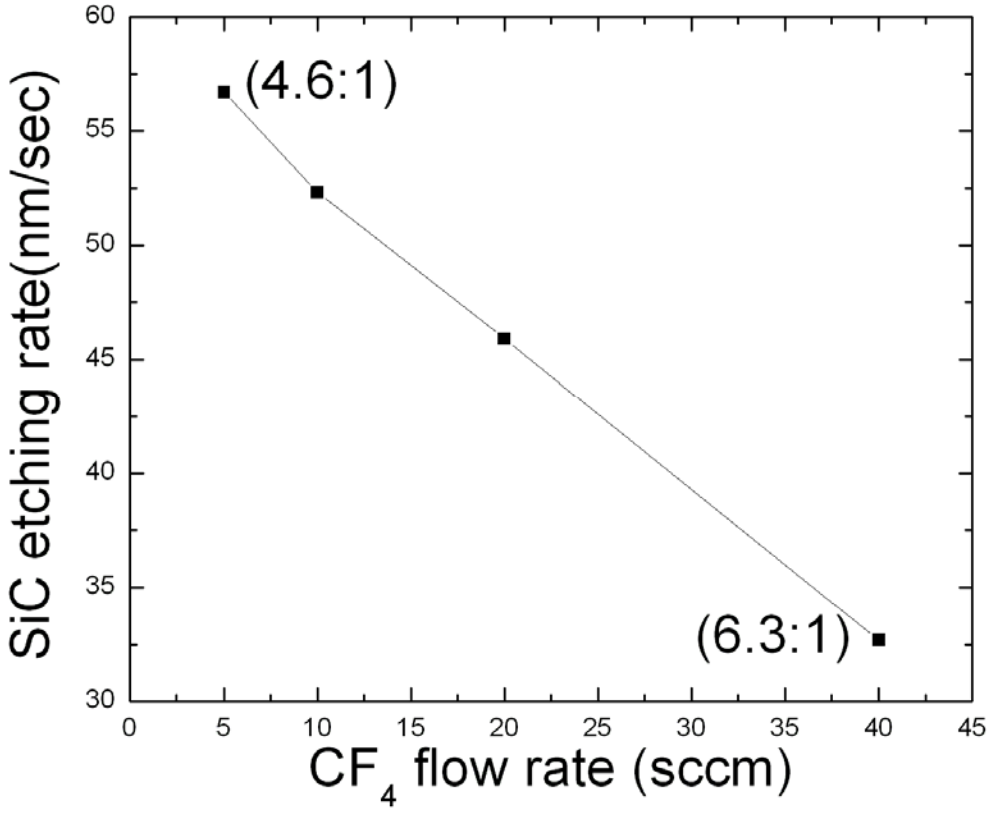

Fig. 3-11 Etching rate of 4H-SiC increases with the decrease of CF_4 flow rate. The selectivity of the photoresist etching rate to SiC bevel etching rate changes from 6.3:1 at 40 sccm to 4.6:1 at 5 sccm.

3.1.3 Ohmic contact study

Good ohmic contact is very critical for 4H-SiC SPADs. The recovery time of SPADs after avalanche is determined by the RC time constant. Within the recovery time, SPADs are blind to any incident photons. Therefore, to decrease the device resistance is an effective way to increase the work bandwidth. N-type ohmic contact has been studied

for a long time and becomes a mature technology. Ni is widely used to form a good n-type ohmic contact.

It is more difficult to achieve a good p-type ohmic contact, and the p-type contact resistance dominates the serial resistance of 4H-SiC SPADs. Normally Al is used to form the p-type ohmic contact. However, the top p++ layer of SiC avalanche photodiodes is designed to be very thin so that high QE can be achieved. In order to avoid the Al-spiking problem during the ohmic contact annealing at high temperature, a new p-type ohmic contact should to be developed and the annealing temperature and time should be carefully controlled. A good ohmic contact can improve the uniformity of the gain over the junction, reduce the contact resistance so as to reduce the *RC* product and increase the bandwidth. Firstly, we uses Ni (600 Å) \ Ti (200 Å)\ Ni (1500 Å) as the contact metal. The ohmic contact is annealed using a rapid thermal annealing system at different temperature in Ar (95%) + H_2 (5%). The specific contact resistivity is evaluated with the transmission line model (TLM). The I-V characteristics between the TLM patterns are measured. The specific contact resistivity is extrapolated from the linear fit of the resistances vs. spacing shown from **Fig. 3-12** to **Fig. 3-16**. The best specific contact resistivity is $5.8\times10^{-3}\Omega cm^2$, shown in **Fig. 3-16**, when the sample is annealed at 650^{o}C for 5 minutes followed by another annealing at 1000^{o}C for 5 minutes.

When the annealing temperature is higher than 1000 ^{o}C, the top p++ layer will be totally consumed and the device is punch-through. The I-V characteristics after punch-through are shown in **Fig. 3-17**.

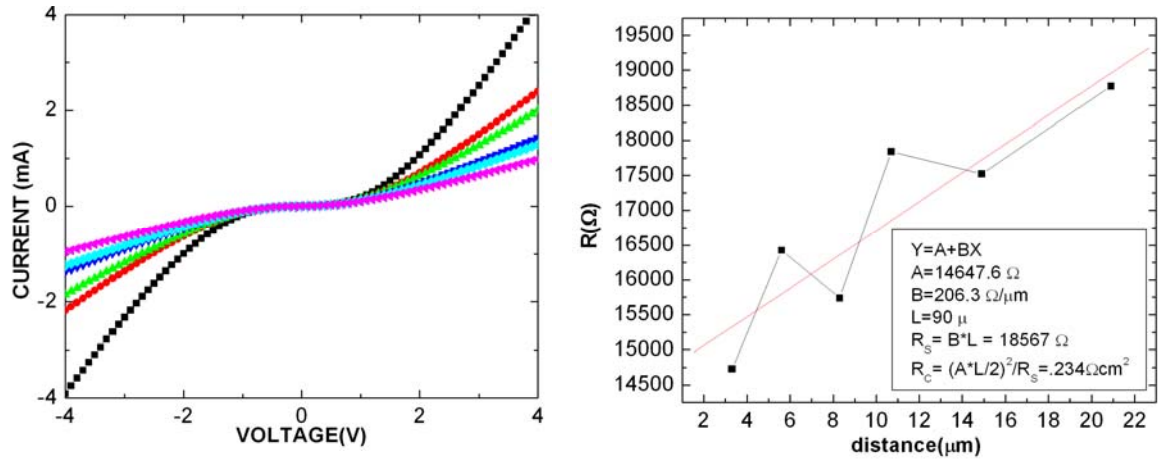

Fig. 3-12 TLM measurement results of p-type ohmic contact annealed at 650°C and extrapolated specific contact resistivity

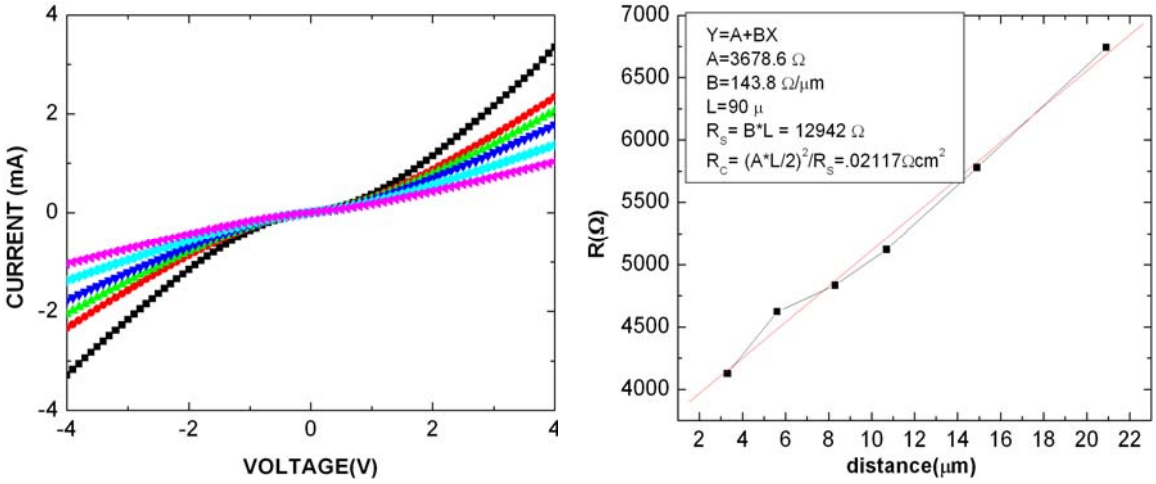

Fig. 3-13 TLM measurement results of p-type ohmic contact annealed at 750°C and extrapolated specific contact resistivity

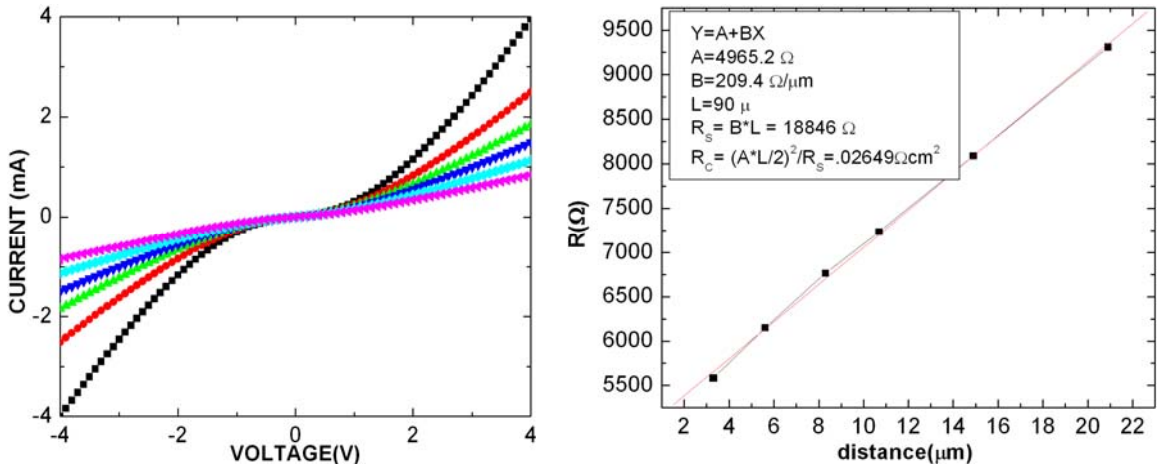

Fig. 3-14 TLM measurement results of p-type ohmic contact annealed at 850°C and extrapolated specific contact resistivity

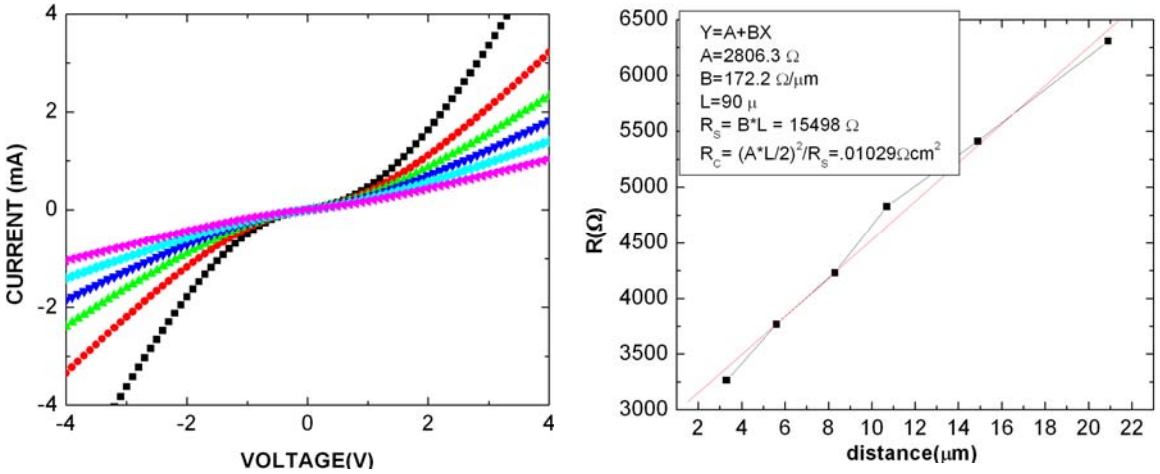

Fig. 3-15 TLM measurement results of p-type ohmic contact annealed at 950°C and extrapolated specific contact resistivity

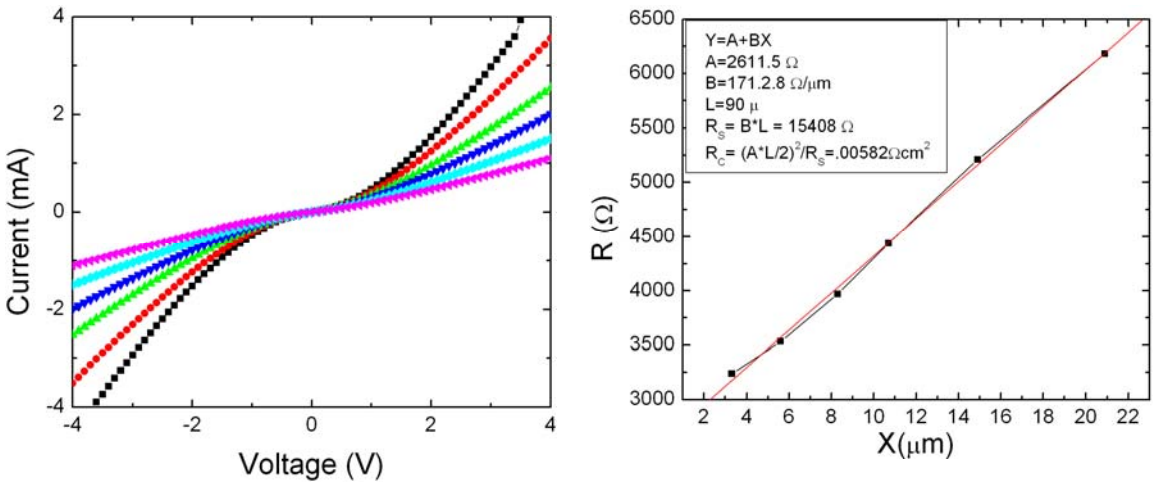

Fig. 3-16 TLM measurement results of p-type ohmic contact annealed at 650°C and 1000°C and extrapolated specific contact resistivity

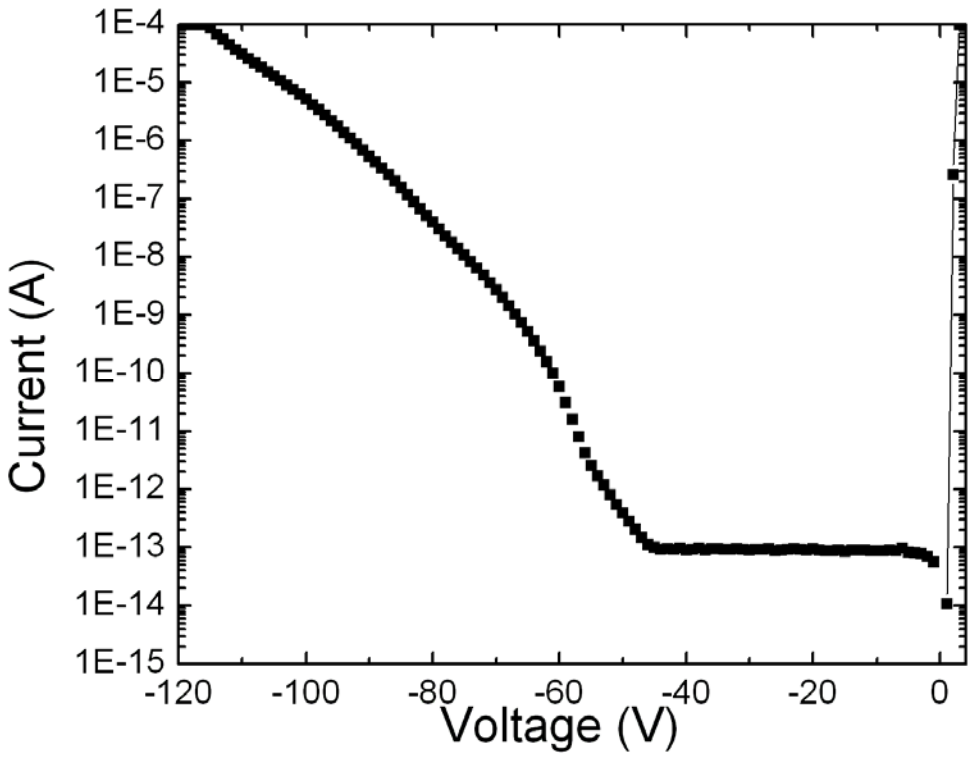

Fig. 3-17 Reverse I-V characteristics of SPAD when p ohmic contact is annealed at 1050°C

3.2 Fabrication of 4H-SiC Single photon avalanche diodes

The 4H-SiC single photon avalanche diodes are designed with on-mesa or off-mesa overlay. With the same optical window, the process of the SPADs with the on-mesa overlay is relatively easier than the SPADs with the off-mesa overlay. However, the on-mesa overlay structure has a larger p-n junction area, which may cause a high dark current and a low yield. The off-mesa overlay structure has its overlay on the dielectric layer. The process is more complicated and dielectric layer should be thick enough to prevent the breakdown through the dielectric.

The epilayers of the SPADs are grown on an n+ 4H-SiC commercial substrate at a rate of 2 μm/hr in an Aixtron/Epigress VP508 hot-wall CVD reactor equipped with Ar gas foil rotation, the rotation improves the doping and thickness uniformity. The entire growth is accomplished in one continuous run in order to avoid interlayer defects during the growth. Silane and propane are used as precursor sources, and nitrogen and trimethylaluminum are used as n-type and p-type dopant sources, respectively [51].

Secondary ion mass spectroscopy (SIMS) result shown in **Fig. 3-18** reveals that the SiC SPAD structure consists of a 0.22 μm p+ contact layer, a 0.16 μm p layer, a 0.26 μm n- depletion layer and a 0.38 μm n buffer layer with doping concentrations of 6×10^{19} cm^{-3}, 6.5×10^{17} cm^{-3}, 4×10^{15} cm^{-3} and 6×10^{18} cm^{-3} for the p+, p, n- and n buffer layers, respectively.

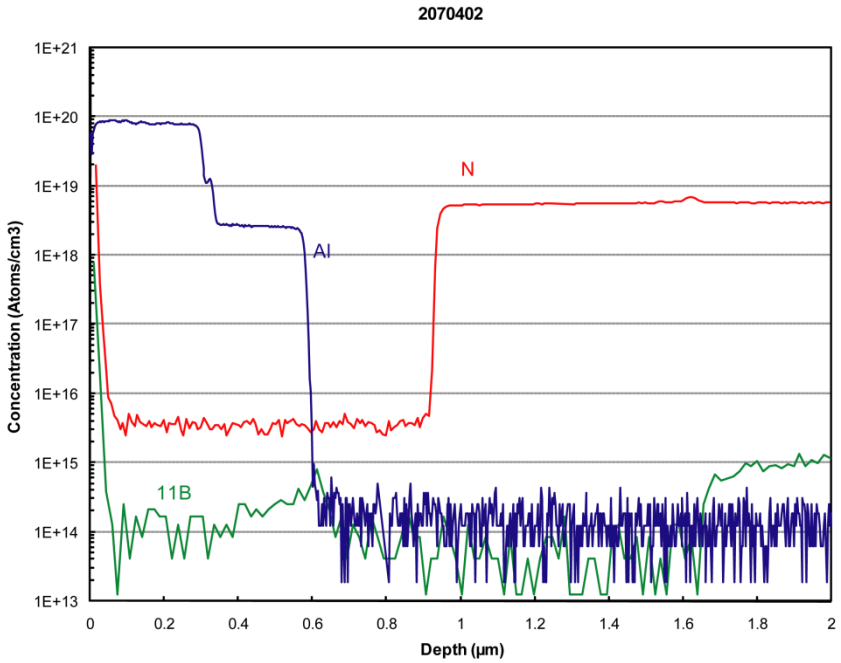

Fig. 3-18 Doping profile of SiC SPAD wafer.

3.2.1 Fabrication of 4H-SiC SPADs with on-mesa overlay

Fig. 3-19 is the schematic cross sectional view of a 4H-SiC SPAD. The 4H-SiC SPAD is firstly isolated by a shallow negative bevel, which is created by the inductive coupled plasma (ICP) dry etching using thick PR as etching mask. The 0.8 µm deep bevel extends 18 µm laterally, indicating a 4^{o} bevel edge termination has been achieved. Before the device passivation, a standard RCA cleaning is carried out to remove the ICP byproducts, native oxide, and organic and ionic contaminants. Device passivation is accomplished in three steps. In the first step a thin sacrificial oxide layer is grown at 1050 ^{o}C for 30 min in wet oxygen to remove the ICP etching damages on the surface (especially on the bevel sidewalls). Then a 3-hour passivation wet oxide is grown at 1050

°C after the sacrificial oxide is removed by the diluted HF. Finally the thermal oxide is covered by 400 nm PECVD SiO_2 and 150 nm PECVD Si_3N_4.

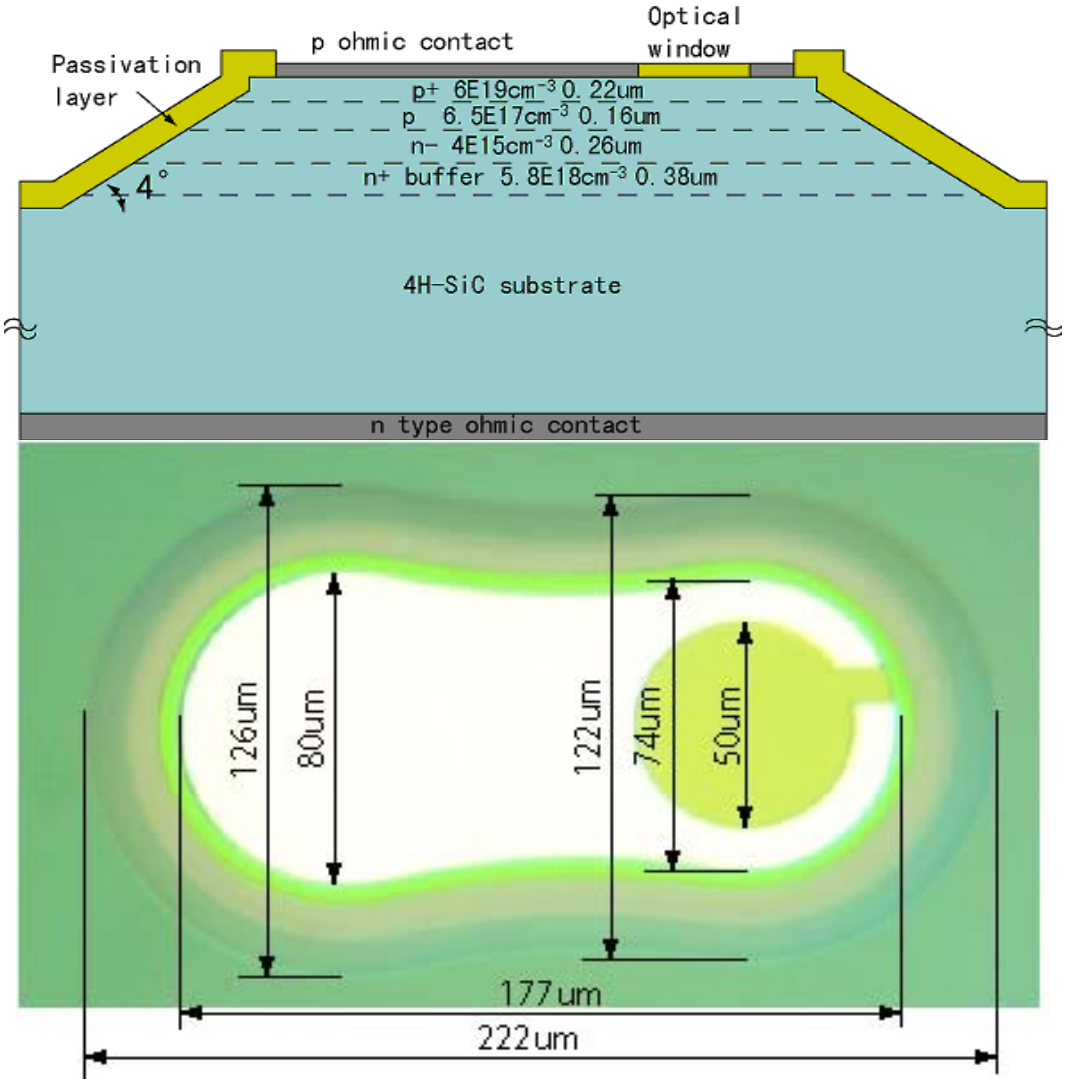

Fig. 3-19 Cross sectional view and top view of 4H-SiC SPADs with on-mesa overlay.

After the oxide is removed from the backside using the buffered oxide etchant (BOE), AlTi (25nm)/Ni (300nm) is sputtered on the backside and annealed at 975 °C for 5 min to form n-type ohmic contact. The top PECVD Si_3N_4 layer within the p contact region and the optical window is removed by an ICP dry etching, and the oxide within the p-contact region is stripped away by a wet etching, whereas the optical window is still

protected by the SiO2 layer. The Ni/Ti/Ni layer is sputtered into the p contact area and annealed at 650 ^{o}C and 1000 ^{o}C to form an ohmic contact to the top p+ layer. This Al-free ohmic contact eliminated the possible Al-spiking during the high temperature ohmic contact annealing. The top view of the 4H-SiC SPAD is shown in **Fig. 3-19**.

3.2.2 Fabrication of 4H-SiC SPADs with off-mesa overlay

Compared with the SPADs with on-mesa overlay, the SPADs with off-mesa overlay have their bonding pad on the dielectric. Therefore, the processing is more complicated.

Before the device passivation, all the processing steps are the same. After thermal oxide layer is grown at 1050 ^{o}C for 3 hours, a dielectric layer $SiO_2\backslash Si_3N_4$ is deposited by PECVD on the device. The thickness is 400nm and 300nm, respectively.

Then backside ohmic contact, Ni, is sputtered on the backside after oxide is removed. The n-type ohmic contact annealing is performed at 975^{o}C for 5 minutes using the rapid thermal annealing system. Simultaneously the front $SiO_2\backslash Si_3N_4$ PECVD layer is condensed during the high temperature annealing. Another 300nm SiO_2 layer is deposited on the front surface so that the total thickness of the $SiO_2\backslash Si_3N_4\backslash SiO_2$ sandwich dielectric layer is increased to 1 μm to prevent the breakdown through the dielectric. Because the top SiO_2 layer is grown after the back side n type ohmic contact formation, the top $Si3N4\backslash SiO_2$ interface does not experience the high temperature annealing so far.

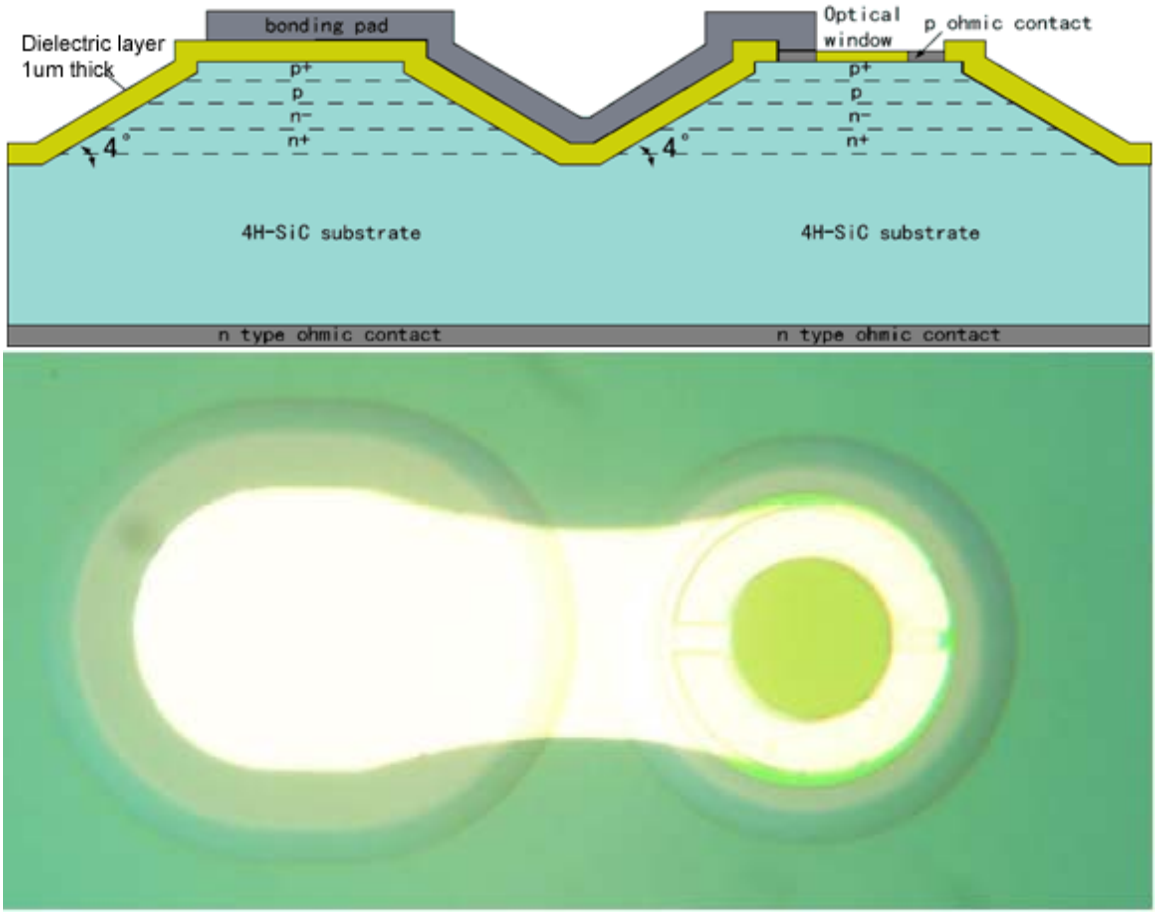

Fig. 3-20 Cross sectional view and top view of 4H-SiC SPADs with off-mesa overlay.

To open the optical window and p contact window, the top SiO_2 layer is firstly removed from the optical window and contact window by a wet etching using the PR as the etching mask and the annealed Si_3N_4 layer underneath as the stop layer followed by the removal of the Si_3N_4 layer using the ICP dry etching. Then the thermal oxide in the p-type contact window was removed by a wet etching, whereas the optical window is still protected by the annealed SiO_2 and thermal oxide.

The p contact metal Ni/AlTi/Ni is sputtered and annealed. During the p ohmic contact annealing, the top SiO_2 is also condensed. Finally, Ti/Au overlay is deposited

serving as the bonding pad of the SPADs. **Fig. 3-20** is the cross sectional view and top view of the fabricated 4H-SiC SPAD with off-mesa overlay.

3.3 Characteristics of 4H-SiC SPADs with on-mesa overlay

Avalanche photodiodes, which operate above the breakdown voltage in the Geiger mode connected with avalanche-quenching circuits, can be used to detect single photons and are therefore called single photon avalanche diodes (SPADs). When the avalanche photodiodes are working under the Geiger mode, the following issues should be considered seriously.

A. Quantum efficiency

   Detectors absorb photons in the detector active region and generate an electron-hole pair. Only those absorbed photons have the probability to trigger the avalanche in the SPAD, and generate voltage pulse or current pulse. The sensitivity and signal to noise ratio can be improved with higher quantum efficiency.

B. Dark current

   Dark current, especially when the device is working at the voltage above avalanche breakdown, is an important parameter to evaluate the performance of the SPADs. Dark current normally is caused by two effects: one is generated by the dark carriers in the bulk which is area dependent. The other is the peripheral leakage current, which is circumference dependent. Dark count rate of a single photon avalanche diode scales with its dark current to some level.

C. Photon detection efficiency

For a photon to be detected, not only must it be absorbed in the detector active volume and generate a primary carrier (more precisely, an electron–hole pair), it is also necessary that the primary carrier succeeds in triggering an avalanche. The efficiency of photon detection increases with excess bias voltage V_E, since a higher electric field enhances the triggering probability. Single photon detection efficiency (SPDE) is defined as the probability that a detectable voltage pulse or current pulse is generated by an incident photon:

$$SPDE(\lambda) = \frac{photon \quad count \quad rate}{incident \quad UV \quad photon \quad flux}$$

Another important parameter, count efficiency, is regarded as the probability of a photon-generated carrier to be multiplied and counted:

$$CE(\lambda) = \frac{SPDE(\lambda)}{QE(\lambda)}$$

D. Dark count rate

Single photon avalanche diode generates current or voltage pulses even without UV illumination. The dark counts include primary and secondary pulses. Primary dark pulses are due to thermally generated dark carriers in the SPAD junction. Secondary dark pulses are caused by afterpulsing effects. During the avalanche, the device capacitor is discharged. Some minority carriers are captured by the deep levels in the depletion region and subsequently released with a fluctuating delay. If the delay is longer than the hold off time of the SPAD after the avalanche, the released carriers can retrigger the avalanche, generating afterpulses correlated with a previous avalanche pulse. The more the charges flowing through the device during the avalanche, the greater the number of carriers trapped and the

more recurrent the afterpulses. Therefore, the trapped charge per avalanche should be minimized by minimizing the duration of the avalanche. If the SPAD can not be self quenched quickly, a feature of the quenching circuit can be exploited to reduce the afterpulsing rate to a negligible or at least an acceptable level. By deliberately maintaining the voltage at the quenching level, the avalanche retriggering by the released carriers are prevented during a hold-off time after quenching. For silicon SPAD's at room temperature a few hundred nanoseconds hold off can reduce the total dark-count rate by orders of magnitude, since it covers most of the release transient and practically eliminates afterpulsing. However, for SPAD's that work at cryogenic temperatures the method is less effective, since the release transient becomes much slower and the required hold-off time may be much longer and hence seriously limit the dynamic range in photon-counting measurements.

3.3.1 I-V and gain characteristics

The SiC SPAD wafer consists of a p+ contact layer, a p layer, an n- depletion layer and an n buffer layer on the n-type substrate. The n- depletion layer is 0.3μm thick with a light doping of $3\times10^{14}cm^{-3}$. The SiC epitaxial layer is grown in one continuous run. **Fig. 3-21** shows the doping concentration of the epilayers and electric field distribution across the bulk SiC. The critical electrical field at the avalanche breakdown is 3.2 MV/cm.

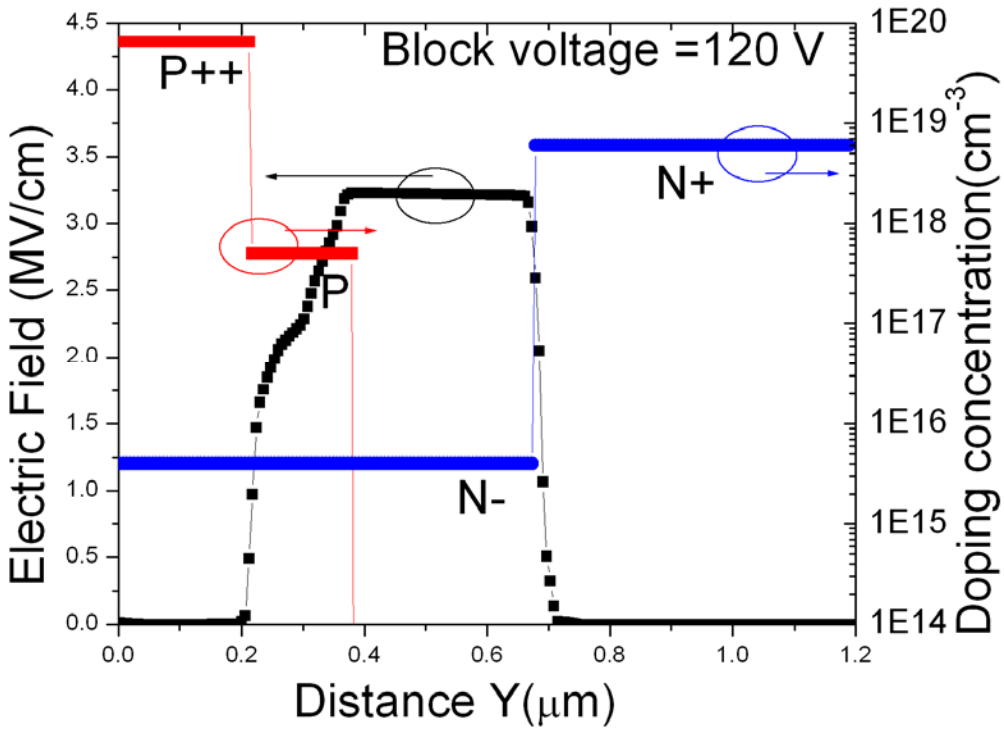

Fig. 3-21 Doping concentration of 4H-SiC single photon avalanche diode and Electrical field across the bulk according to computer simulations.

The 4H-SiC SPAD is characterized at the chip level. Reverse I-V characteristics are measured by Keithley 4200-SCS semiconductor characterization system. **Fig. 3-22** shows that the leakage current at –5 V is 5.3 fA, which corresponds to a low current density of 26 pA /cm^2 if the p-n junction area (2.03×10^4 μm^2) is considered. When the reverse bias is less than 80 V, the leakage current is lower than 20 fA. Avalanche breakdown occurs at the reverse bias of 114 V, and both the 0.26 μm n- layer and the 0.16 μm p layer are depleted at the breakdown. At 90% of the breakdown voltage, the leakage current is 57 fA, which corresponds to a current density of 0.28 nA/cm^2. The gain of the 4H-SiC SPAD is measured with UV illumination at the wavelength of 280 nm. The unit gain is defined at 50% of the breakdown voltage (-57 V), where the SPAD shows a

low leakage current of 17 fA. The linear gain reaches 1.4×10^{6} at the reverse bias of 116.8 V.

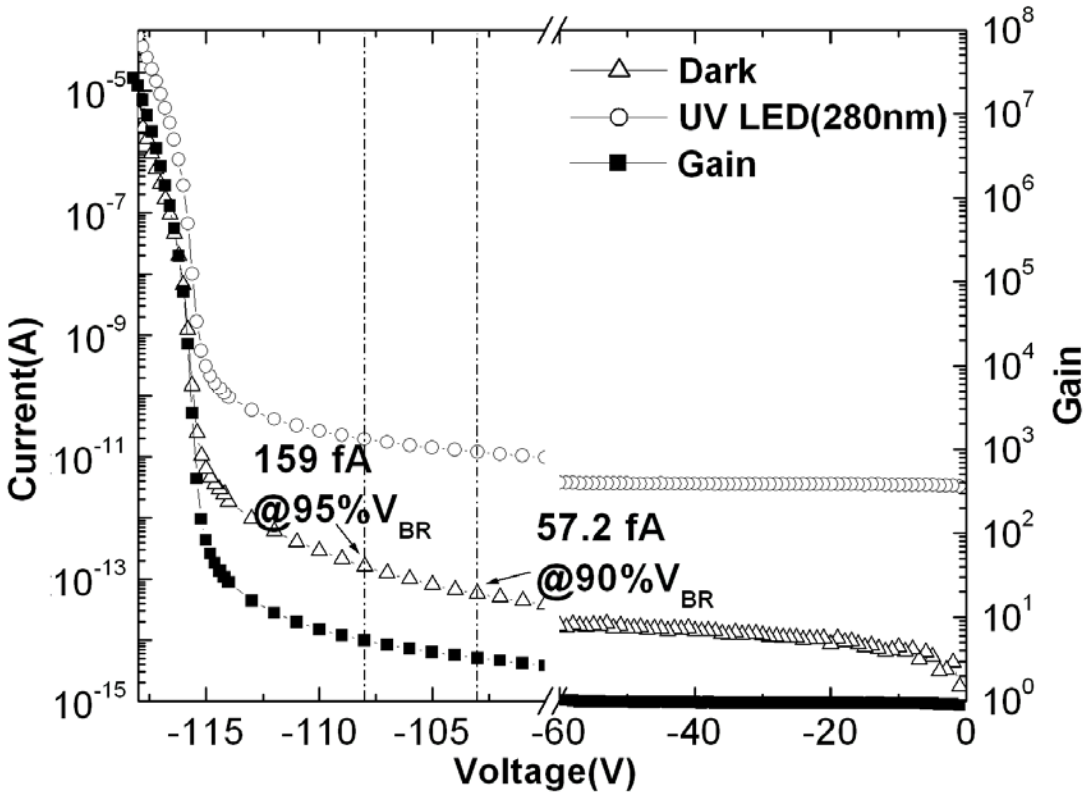

Fig. 3-22 I-V and gain characteristics of 4H-SiC single photon avalanche diode.

3.3.2 UV photo response measurement

The photoresponse spectra of 4H-SiC SPADS from 250 nm to 400 nm are measured using a Xenon lamplight source with a near UV monochromator. The UV monochromic light is coupled into an optical fiber and then focused on the devices through a UV objective. The QE of 4H-SiC is measured at –5 V and –57 V. **Fig. 3-23** shows that the QE at –5 V is virtually the same as that at –57 V indicating a unit gain before avalanche breakdown. The maximum QE of 43% occurs at the wavelength of 270

nm. Compared with the QE of <0.007% at 400 nm, the UV-to-Visible rejection ratio is higher than 6.1×10^{3}. At the wavelength of 280 nm and 350 nm, the QE is 29.8% and 2.04% respectively.

It should be recognized that the absorption length of 4H-SiC decreases dramatically when the wavelength decrease from visible region to 270 nm. The 4H-SiC SPAD has its p and n- layer depleted during the measurement, and the absorption layer is 0.22 μm away from the surface and 0.42 μm thick. At 350 nm, the absorption length of 4H-SiC is 35 μm [11]; our calculation shows that around 2% UV light will be absorbed in this absorption layer, indicating that this absorption layer has the dominant contribution to the QE.

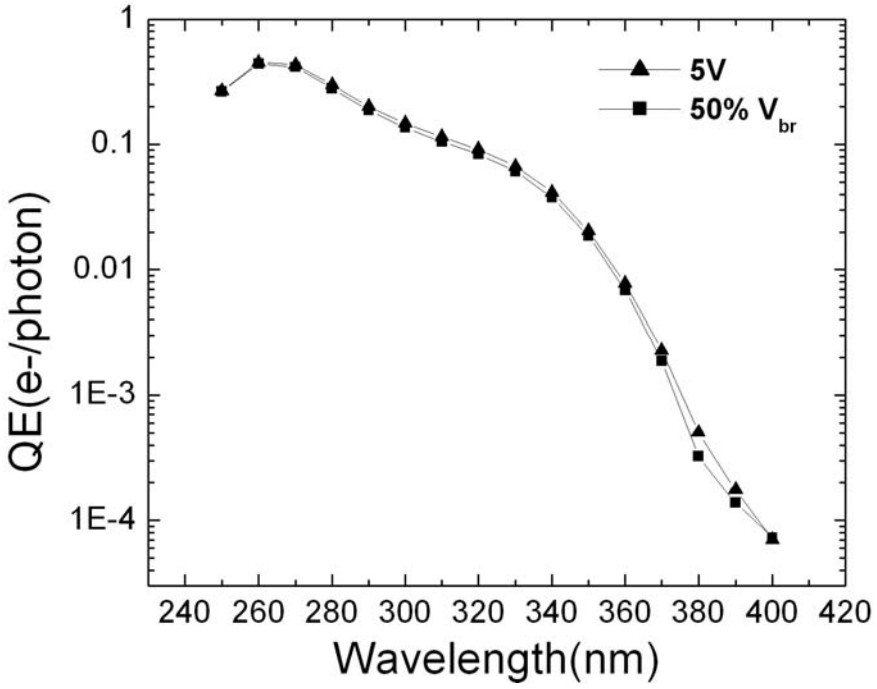

Fig. 3-23 Quantum efficiency of 4H-SiC single photon avalanche diode.

3.3.3 Single photon counting measurements

Traditional passive quenching circuits employed in the experimental studies shown in **Fig. 3-24**.

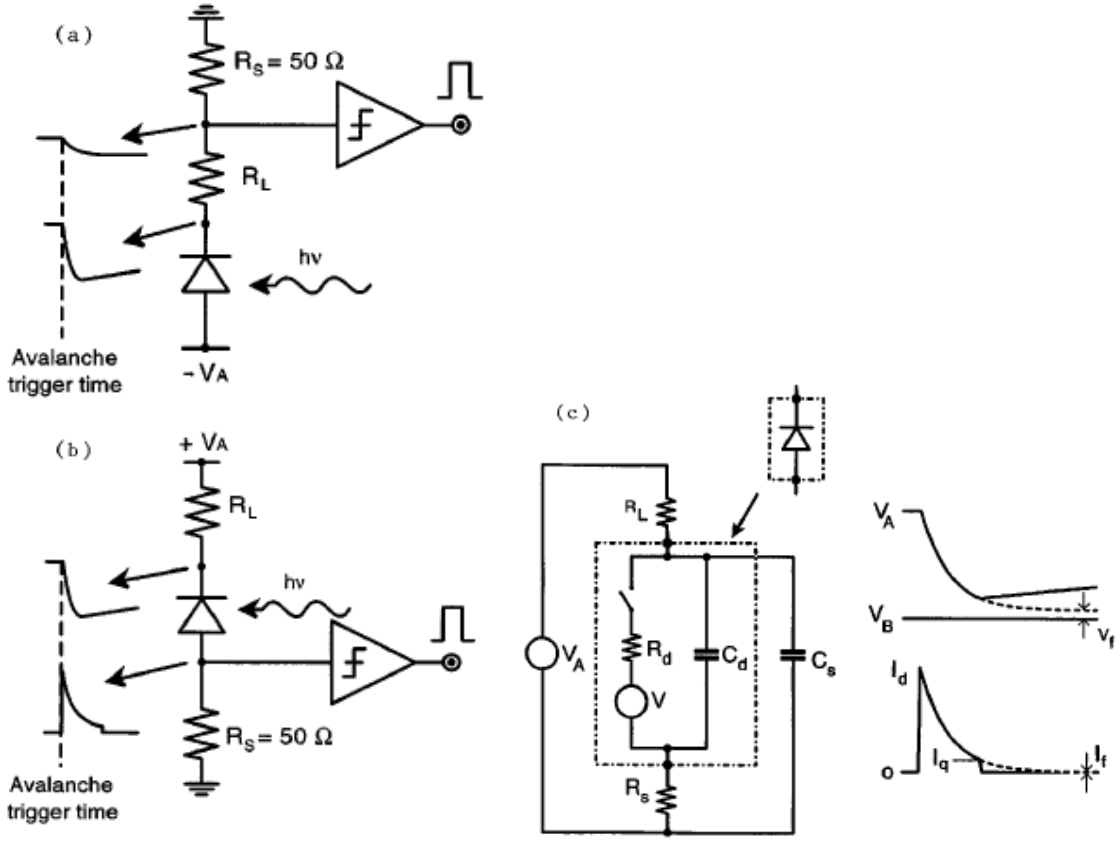

Fig. 3-24 Basic passive quenching circuits: (a) configuration with voltage-mode output, (b) configuration with current-mode output, (c) equivalent circuit of the current-mode output configuration.

The avalanche current quenches itself simply by developing a voltage drop on a high impedance load. The SPAD is reverse biased through a high ballast resistor R_L of 100 kΩ or more, C_d is the junction capacitance, typically in pF level, and C_s is the stray capacitance (capacitance to ground of the diode terminal connected to R_L, typically a few

picofarads). The diode resistance R_d is given by the series of space–charge resistance of the avalanche junction and the ohmic resistance of the neutral semiconductor crossed by the current. The R_d value depends on the semiconductor device structure. Avalanche triggering corresponds to closing the switch in the diode equivalent circuit.

The avalanche current discharges the capacitances so that V_d and I_d exponentially fall down. The quenching time constant T_q is set by the total capacitance $C_d + C_s$ and by R_d and R_L in parallel, i.e., in practice simply by R_d,

$$T_q = (C_d + C_s)\frac{R_d R_L}{R_d + R_L} \approx (C_d + C_s)R_d$$

The avalanche is self-sustaining above a latching current level I_q and is self-quenching below it. The I_q value is not sharply defined, as is evidenced by a jitter of the quenching time with respect to the avalanche onset and by a corresponding jitter of diode voltage V_q at which quenching occurs.

The total charge Q in the avalanche pulse is an important parameter for evaluating the trapping effects. After avalanche, the reverse bias on the diode will be recovered and the switch in the equivalent passive quenching circuit is open. The recovery time constant T_r of the voltage is defined as:

$$T_r = R_L(C_d + C_s)$$

The load resistance should be carefully chosen for traditional passive quenching circuit. It must be large enough so that voltage across the avalanche diode drops to below the breakdown voltage when avalanche is triggered and the avalanche can be quenched. Otherwise, avalanche will be self-sustaining for a long time before quenching happens, which may heat up the avalanche diode and damage the diode.

However, the load resistance should not be too large, since the recovery time is proportional to it. With larger R_L, It takes longer time for the voltage across the avalanche diode to recover, which means the diode has a longer dead time after one avalanche occurs and is blind to the photons coming into the diode during the dead time. In this case, the avalanche diode can only work at lower counting rates.

To extend the working range toward higher counting rates, the recovery time of SPAD's in PQC's must be minimized by minimizing the values of ballast resistor R_L and stray capacitance *Cs*.

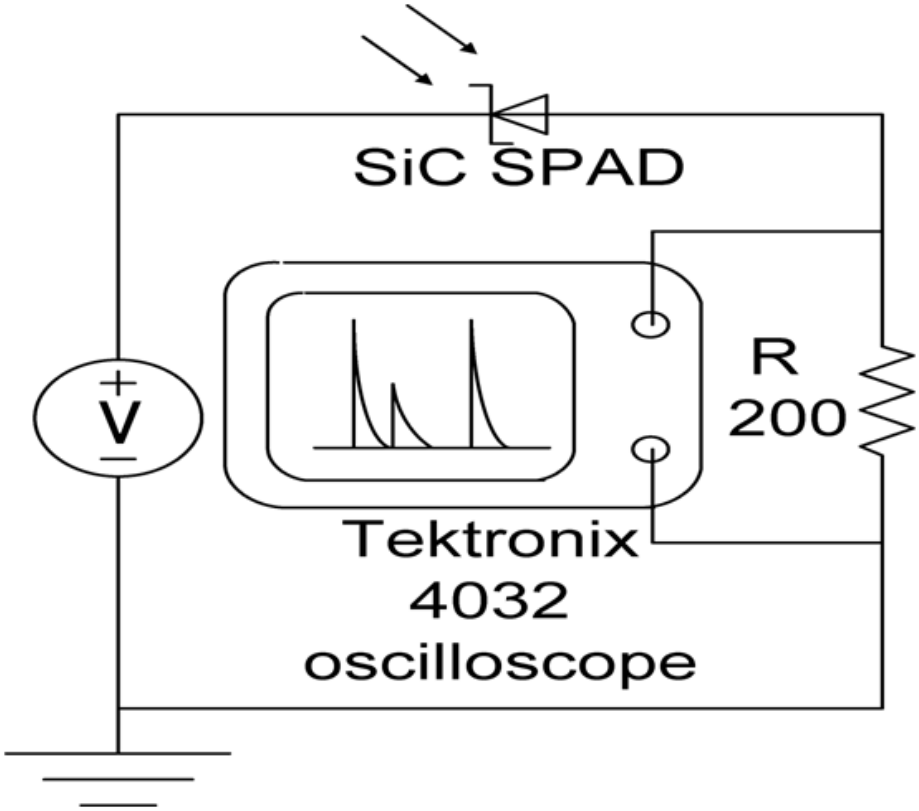

Fig. 3-25 Passive quenching circuit for 4H-SiC SPAD testing.

The passive quenching circuit in our single photon counting experiments for 4H-SiC SPADs is shown in **Fig. 3-25**. It is worthwhile to notices that the ballast resistor is

zero. However, our 4H-SiC SPADs can still be self quenched very quickly, and the single photon counting results will be present later.

Keithley 2400 sourcemeter is used to provide a reverse DC bias on the anode of the SPAD. UV LEDs peaked at 280 nm and 350 nm are used as the photon sources. Output voltage pulse signals are collected through a 200 Ω load resistor using a Tektronix DPO 4032 oscilloscope. Each measurement recorded 4 msec data with a sampling rate of 2.5 Gs/sec.

Single photon counting measurements should be done at a very quiet environment. In order to eliminate the noise coming from any electrical magnetic interference, the measurement is performed in a box with electrical magnetic screen. The system noise is measured before avalanche diode is loaded into the passive quenching circuit, which is shown in **Fig. 3-26**.

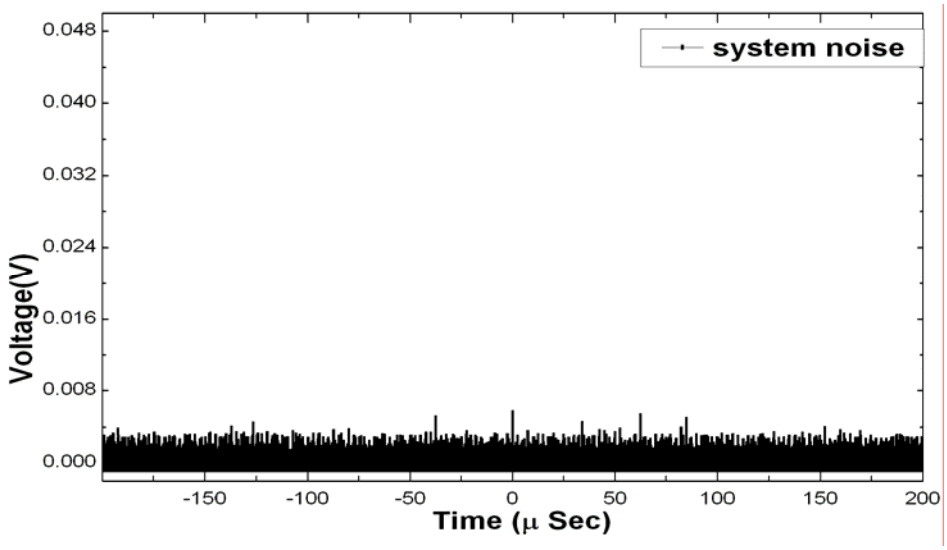

Fig. 3-26 System noise before avalanche diode is loaded into the passive quenching circuit.

Single photon counting measurements are performed at the solar-blind wavelength of 280 nm. The incident photon flux is measured to be 1.50×10^7 photon/sec. The working reverse bias is carefully chosen to obtain the optimized single photon counting performance for the SiC SPAD and is increased from 116 V to 117 V in 0.2 V steps. Both the dark count rate and photon count rate are measured.

Fig. 3-27 and **Fig. 3-28** show the dark count over a wide time span of 400 μsec and photon count spectra over a wide time span of 40 μsec, respectively, at the reverse bias from 116.0V to 116.8 V with an increment of 0.2V. The avalanche gain, the voltage pulse height, the DCR and the photon count rate increases with the reverse bias applied on the SPAD.

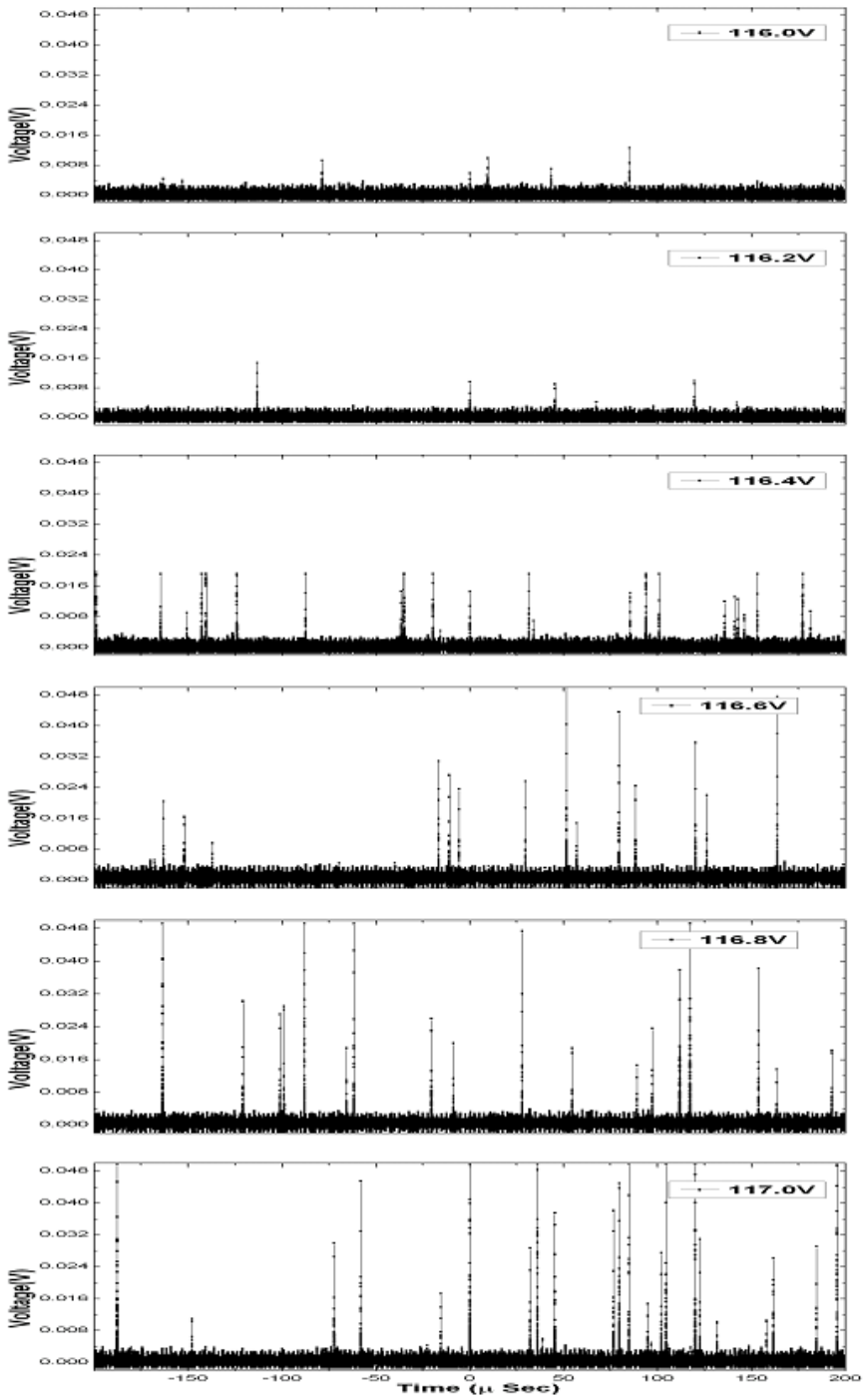

Fig. 3-27 Dark count spectra over 400 μsec at the voltage from -116.0V to -116.8V with an increment of 0.2V

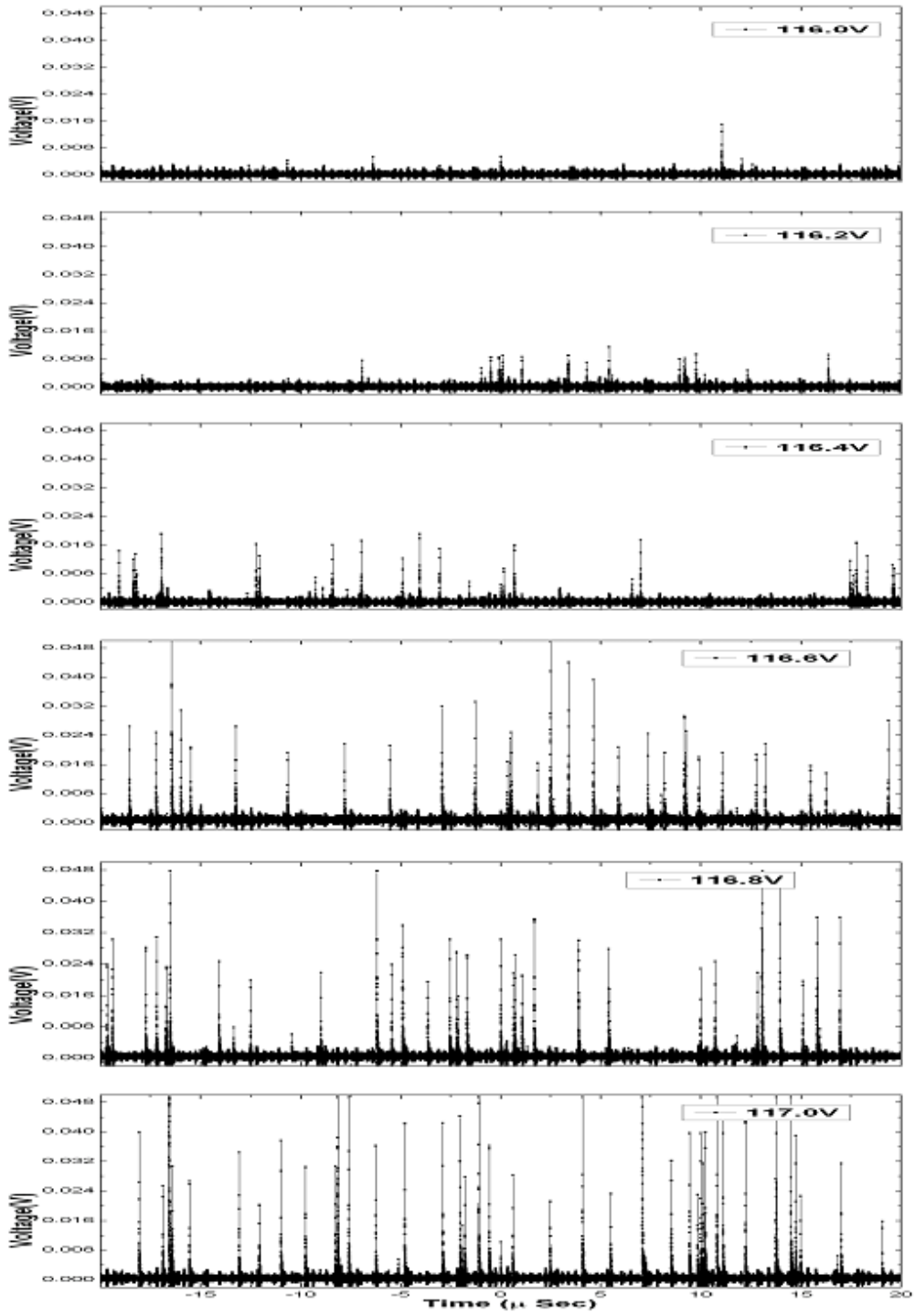

Fig. 3-28 Photon count spectra over 40 μsec at the voltage from -116.0V to -116.8V with an increment of 0.2V

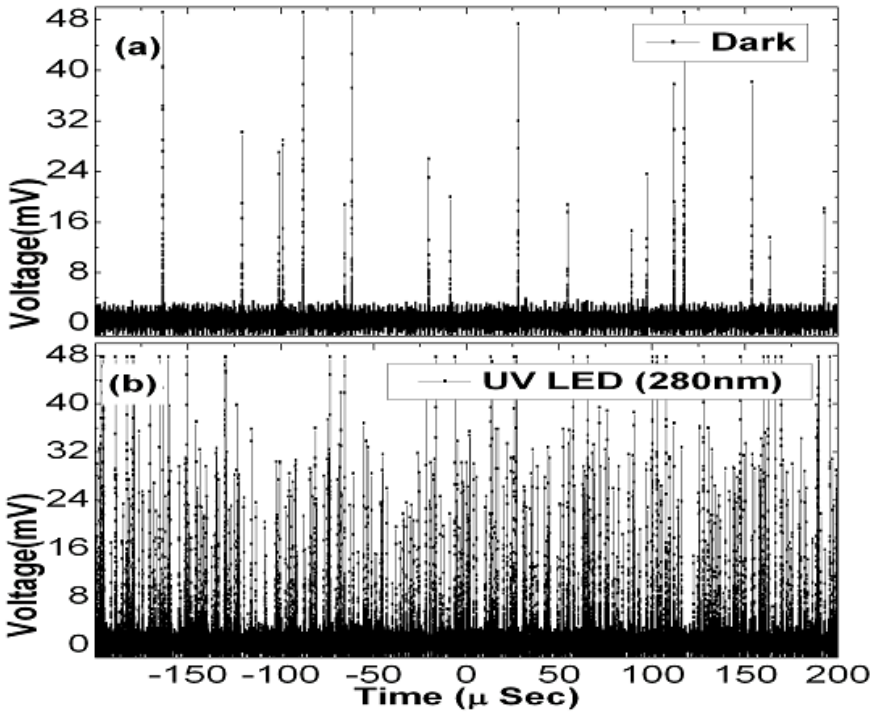

Fig. 3-29 Dark count and photon count spectra over 400 μsec at -116.8V

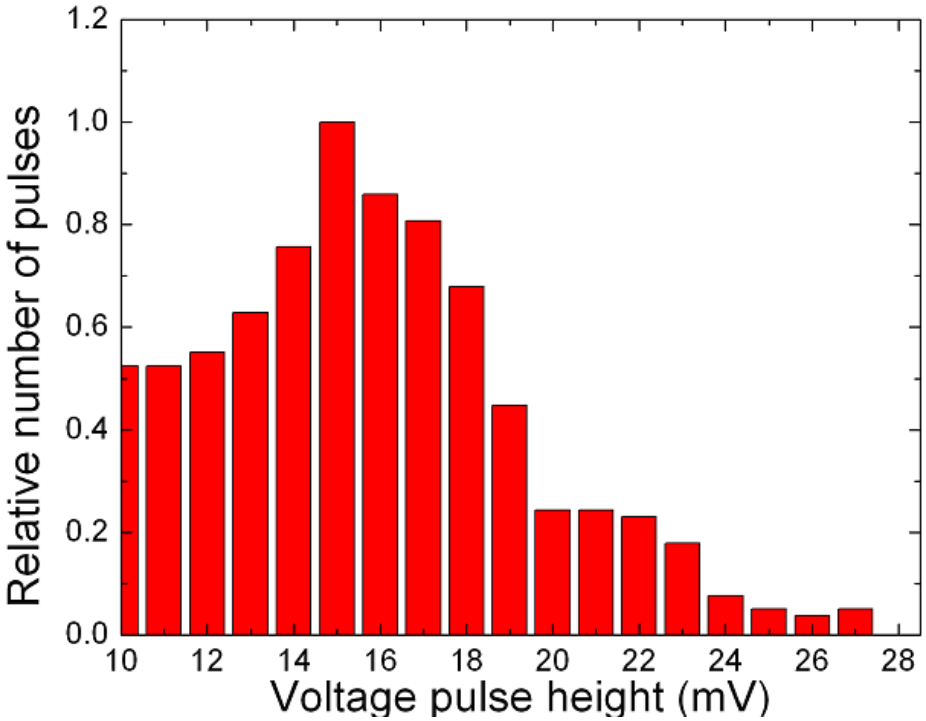

Fig. 3-30 A typical histogram pulse-height distribution

Fig. 3-29 shows the dark count and photon count spectra at -116.8V in 400 μsec. A typical histogram of the pulse-height distribution is shown in **Fig. 3-30**. The procedure is to adjust the threshold voltage level to avoid noise pulses at lower voltage levels. The major population of the voltage pulses has the pulse height between 10 mV and 18 mV. Therefore, the threshold voltage of 10 mV allows utilization of the majority of photo generated voltage pulses and effectively discriminates against noise pulses at lower voltage levels.

The dark count is not only a function of SPAD applied reverse bias, but also is dependent on the photon counting threshold voltage. **Fig. 3-31(a)** shows that the number of dark counts decreases dramatically with the increase of the photon counting threshold voltage. The operation condition can be optimized by minimizing the DCR and maximizing the SPDE at the same time. However, because the DCR and SPDE have the same tendency when the operation voltage and threshold voltage change, we can only find a best compromise between them. **Fig. 3-32** shows that the highest ratio of SPDE over the DCR is achieved at the reverse bias of 116.8 V with the threshold voltage from 12 mV to 18 mV.

Based on **Fig. 3-31(b)**, when the threshold voltage used for pulse counting at the reverse bias of 116.8V is increased from 10 mV to 18 mV, the DCR drops from 91 kHz to 22 kHz, and the photon count rate decreases from 1.44 MHz to 836 kHz, which corresponds to a reduction of the SPDE from 4.87% to 2.83%.

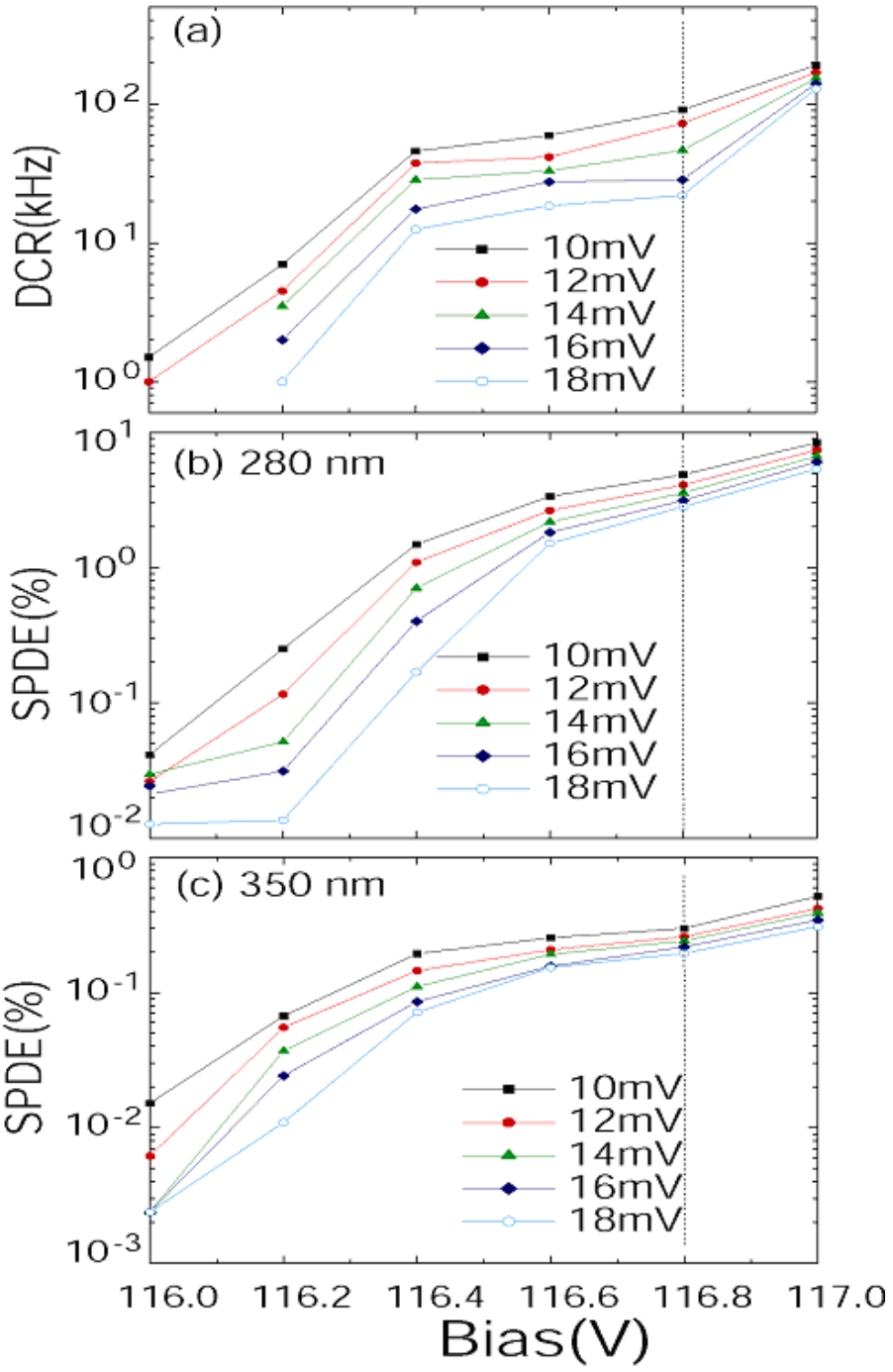

Fig. 3-31 Dark count rate and single photon detection efficiency (SPDE) of 4H-SiC SPAD at 280 nm and 350 nm

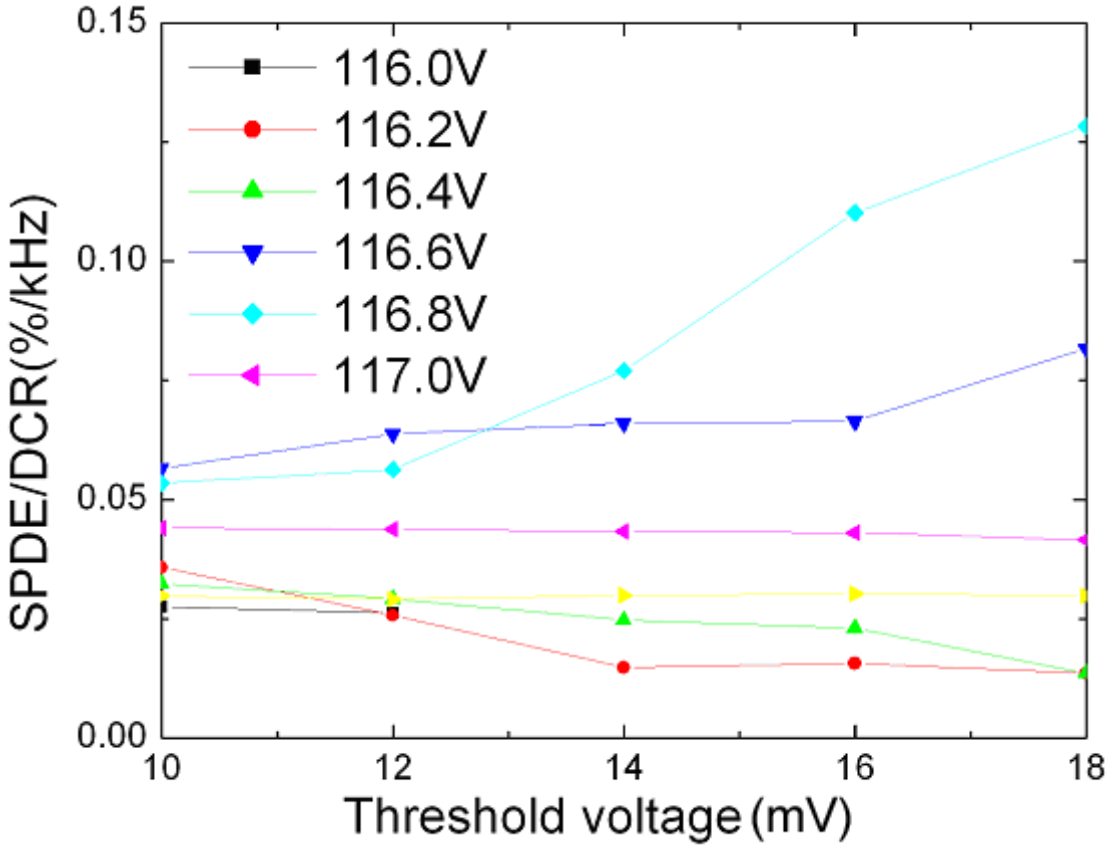

Fig. 3-32 The ratio of the single photon detection efficiency (SPDE) to dark count rate (DCR) at 280 nm to determine the optimized working bias for single photon counting.

It should be pointed out that the SPAD has a low DCR of 22 kHz at 116.8 V with a threshold voltage of 18 mV, which corresponds to a very low normalized DCR of 1.2 Hz/μm^2, showing the tremendous potential of SiC SPADs as SiC material quality continues to be improved. Moreover, since the dark current and the DCR of a SPAD scale with the p-n junction area, reducing the junction area is an effective way to reduce the DCR. The optical window size of the SPAD is 1.93×10^3 μm^2. Although much larger than typical Si SPADs, the window is only 10% of the junction area, and >60% of the top mesa is occupied by the wire-bonding pad that has no contribution to the photon counting. Various approaches, including off-mesa bond pad design, to further reduce

DCR show that SiC SPAD with lower DCR and larger optical window is possible even at present when SiC defect density is still many orders of magnitude higher than that in Si.

The counting efficiency of the SiC SPAD is analyzed at the optimized reverse bias of 116.8 V with different threshold voltages. The QE at the wavelength of 280 nm is 29.8%, which also sets an upper limit on the counting efficiency. **Fig. 3-33** shows that when the threshold voltage increases from 10 mV to 18 mV, the counting efficiency decreases from 16.4% to 9.45% at 280 nm.

As comparison, single photon counting measurement is also performed at the wavelength of 350 nm. Because of much longer penetration depth of 4H-SiC at 350 nm, the QE of 2.04% is much lower than that at 280 nm. In order to get enough photon counts, UV LED light intensity is increased to 5.26×10^{7} photon/sec. The SPDE of the 4H-SiC SPAD at 350 nm is also shown in **Fig. 3-31(c)**. At the reverse bias of 116.8 V, the SPDE varies from 0.299% to 0.195% when the threshold voltage increases from 10 mV to 18 mV. Correspondingly, the calculated counting efficiency decreases from 15.1% to 9.6% shown in **Fig. 3-33**.

It is very interesting to observe that at reverse bias of 116.8V, the counting efficiency at the wavelength of 350 nm agrees very well with that at 280 nm with the threshold voltage between 10 mV to 18 mV. The slight difference at the threshold voltage of 10 mV is due to the noise pulses at lower voltage levels. The good agreement of the counting efficiency implies that, as a function of wavelength, SPDE appears to be more dependent on QE rather than the avalanche process which follows, namely, SPDE appears to increase in proportion to QE. The virtually identical values of CE at 280 nm and 350 nm suggest the SPAD avalanche process is uniform within the UV region.

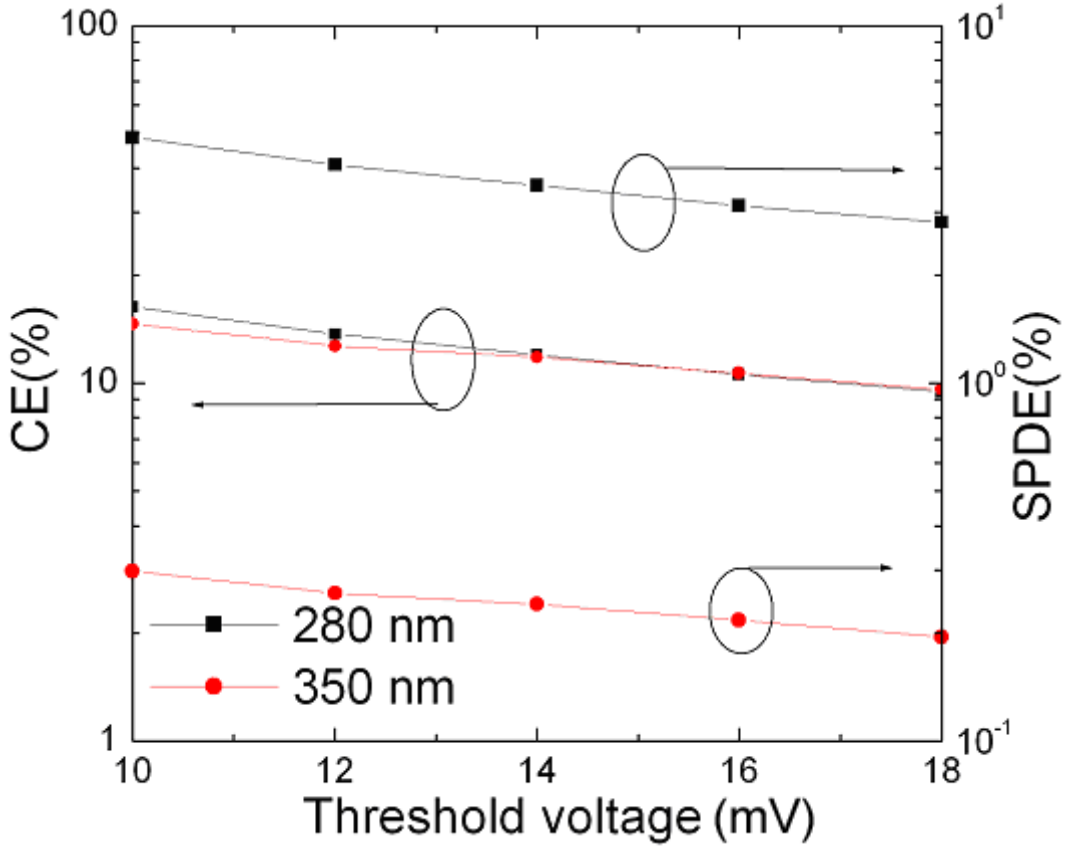

Fig. 3-33 Single photon detection efficiency (SPDE) and counting efficiency of 4H-SiC SPAD at 280 nm and 350 nm under reverse bias of 116.8V. The counting efficiency at 350 nm closely approximates that at 280 nm.

The typical passive quenching circuits and the equivalent circuit of current-mode output configuration have been shown in **Fig. 3-24**, where R_L is the ballast resistor, which is typically higher than 100 kΩ for Si SPADs in the passive quenching mode. The typical quenching transition is as follows:

1) When avalanche occurs, the switch is close, APD discharges through Rd//(R_L+R) and the APD is quenched
2) Then the switch is open, V_A charge the APD through (R_L+R)
3) APD is then ready for single photon counting

In our passive quenching circuit shown in **Fig. 3-25**, the ballast resistance is zero. A typical voltage pulse of 4H-SiC SPAD is shown in **Fig. 3-34**. The rise time of the pulse is 0.8 nsec and the fall time is about 12.4 nsec. The full width at half height (FWHH) of voltage pulses is 1.6 nsec. The total charges passing through the SPAD in this avalanche are 3.91×10^{6} electrons. It should be pointed out that our passive quenching circuit does not involve a ballast resistor, which is used in Si SPAD passive quenching circuits to suppress the current through the Si SPAD below the quenching level after avalanche. The minimum ballast resistor in Si passive quenching circuits is about 100 kΩ to several MΩ, which always introduces a long recover time and limits the photon counting rate of Si SPADs in the passive quenching mode [52]. In our case, the 4H-SiC SPAD can be self-quenched very quickly in the passive quenching mode without a large ballast resistor, indicating that 4H-SiC SPAD can work at much higher photon count rate in a passive quenching circuit instead of a more complex active quenching circuit.

If we consider the capacitance of SiC APD at 116.8V, the pn junction area, A, is $2.03\times10^{-4}\mu m^2$, the depletion depth, W_d, is 0.42 μm (both p and n- layers are depleted). The device capacitance, $C_d=\varepsilon_r\bullet\varepsilon_0\bullet A/W_d=4.15pF$. The total charges on the device junction capacitor, $Q_{SiC}=V_A\bullet C_d=484pC$.

From **Fig. 3-34**, we find that the pulse height, I_{peak} = 25 mA and the pulse width (T_p) at the bottom is about 14 nsec. The total charges in one avalanche event is: $Q_{SiC}'= 1/2 \bullet I_{peak} \bullet T_p = 1.75\ pC$, which is only 0.4% of the total charges, which means that the device is almost self quenched in this "passive quenching" mode. And normally the stray capacitance is a few pF. And because in our case the R_L is small, The quenching time constant Tq is determined by (assume $C_s = 5pF$)

$$Tq = (C_d + C_s)\frac{R_d R_L}{R_d + R_L} \approx (C_d + C_s)R_L = 9.15\,pF \times 312.6\Omega = 2.86nSec$$

From **Fig. 3-34**, we find the pulse drop to 1/e of the peak in about 1.6nSec, which is at the same level of T_q considering that Cs is unknown.

As comparison, a commercial Si single photon avalanche diode is also tested in the same passive quenching circuit. The breakdown voltage is 24.5V, C_d is typically 10pF. The total charges on the device capacitor should be $Q_{Si}=V_A \bullet C_d=24.5pC$. However, from **Fig. 3-34**, we find the total charges that are discharged in one Avalanche event is $Q_{Si}'= 312pC$, which is larger than the total charges on the device before avalanche. That mean the device self-sustains avalanche for a long time, and it takes a long time to quench the avalanche.

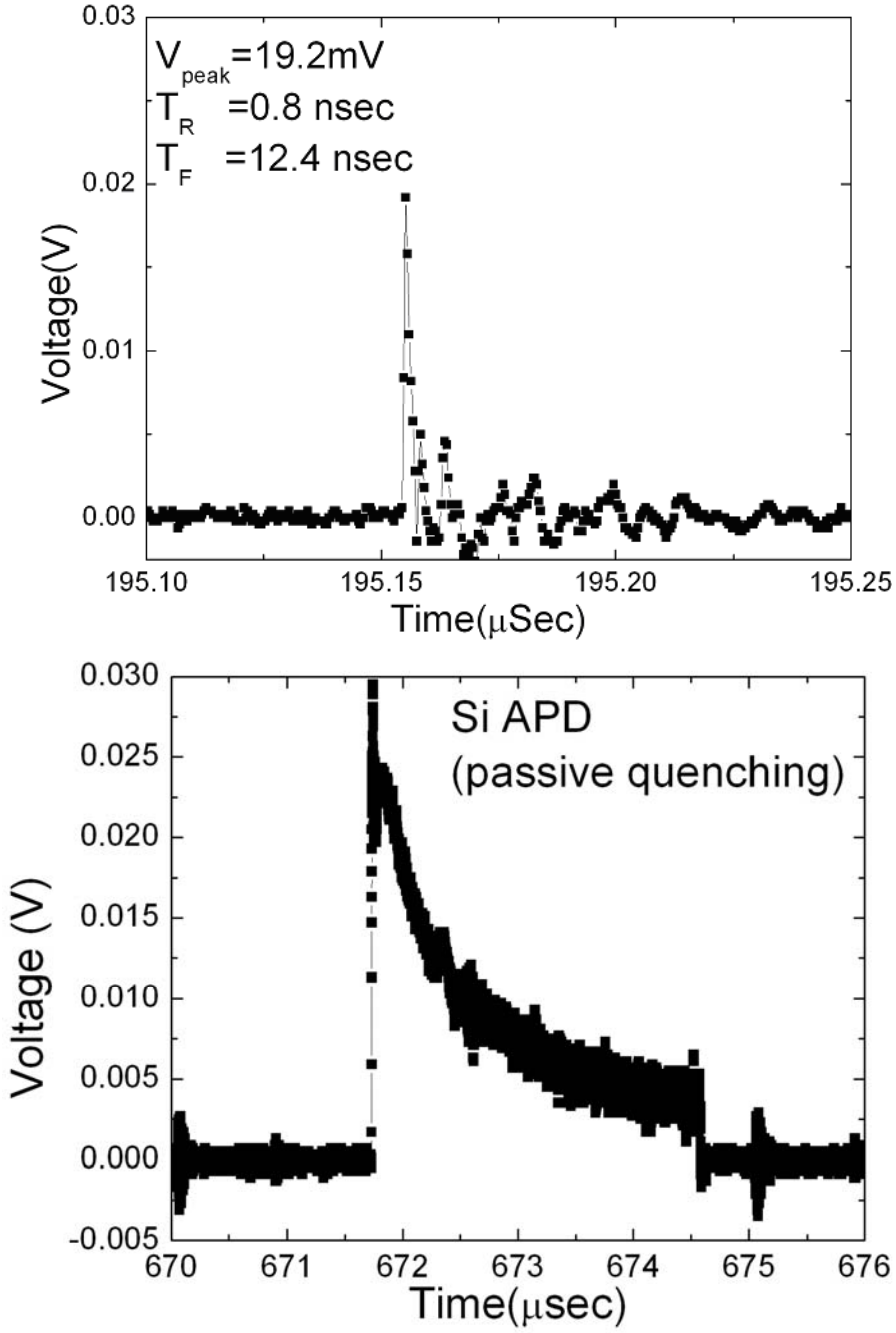

Fig. 3-34 Comparison of pulse transition of 4H-SiC SPAD and Si SPAD in the same passive quenching circuit.

3.4 Characteristics of 4H-SiC SPADs with off-mesa overlay

3.4.1 I-V and gain characteristics

As I mentioned before, 4H-SiC SPADs with on-mesa overlay occupy a much larger p-n-junction area than the SPADs with off-mesa overlay, and the leakage current scales with the junction area to some degree. In order to improve the single photon counting performance, a 4H-SiC SPAD with off-mesa overlay with ID of QDL20 is fabricated and characterized at the chip level using Keithley 4200 Semiconductor characterization system.

Fig. 3-35 shows that the avalanche breakdown voltage of the SPAD is -117 V. When the reverse bias is less than 60 V, the leakage current is very low and reaches the system limit of Keithley 4200. At the 90% breakdown voltage, the leakage current is 43 fA, which corresponds to a current density of 0.47 nA/cm^2 if the p-n junction area of 9161 μm^2 is taken into account. The gain of 4H-SiC SPAD is measured at the wavelength of 280 nm. The unit gain is defined at 50% breakdown voltage of -117V, where the SPAD shows a low leakage current of less than 5 fA. The linear gain reaches 1.2×10^6 at the reverse bias of 119.2 V, where the dark current is 2.05×10^{-8} A. As comparison, For the single photon avalanche diode with on-mesa overlay structure, at the gain of 1.14×10^6 with the reverse bias of 116.8 V, the dark current is 1.68×10^{-7} A, which is 8 times higher than the SPAD with off-mesa overlay, indicating a lower DCR can be achieved for the SPAD with off-mesa overlay.

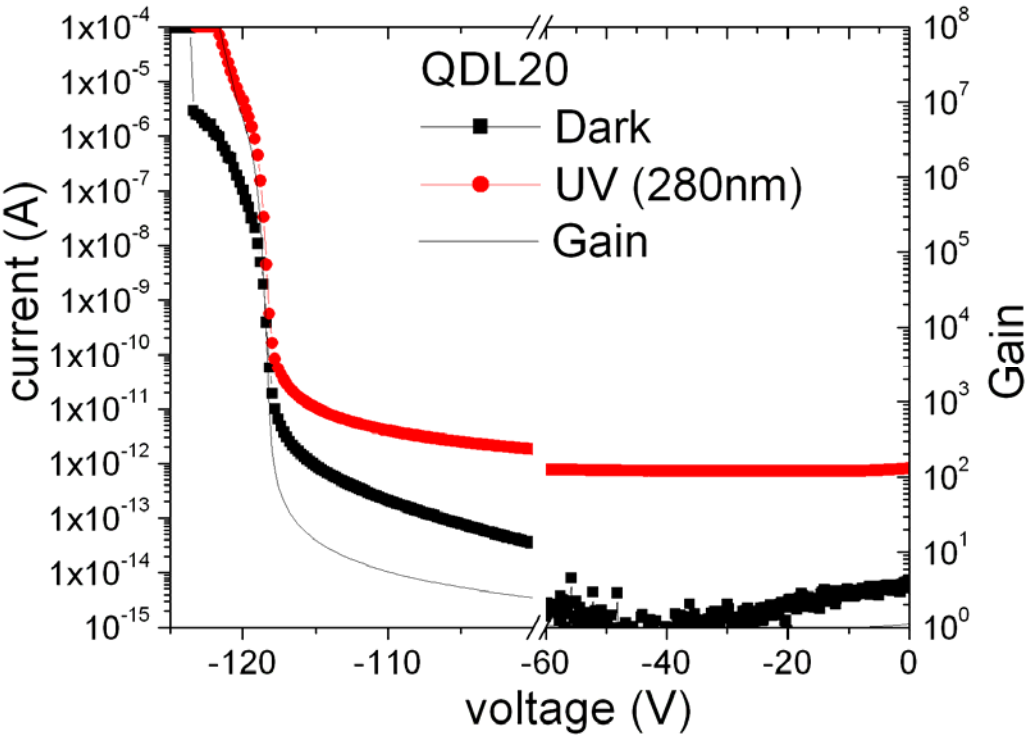

Fig. 3-35 I-V and gain characteristics of 4H-SiC SPAD with off-mesa overlay

3.4.2 Single photon counting measurements

The SPAD with off-mesa overlay has the same QE as the SPAD with on-mesa overlay. Single photon counting measurements are performed at 280 nm from 118.8V to 119.4V with the increment of 0.1 V. Because the avalanche triggered by the photon-generated carriers is a statistical event, in order to ensure the results to be reliable and accurate, we adjust the photocurrent so that the photon count rate is at least one order higher than the DCR. In this case, the photon current at unit gain is 342fA, consider the QE of 29.8% at 280 nm, the incident photon flux is 7.05×10^6 photons/sec and the corresponding photon-generated carrier flux is 2.11×10^6 electrons/sec.

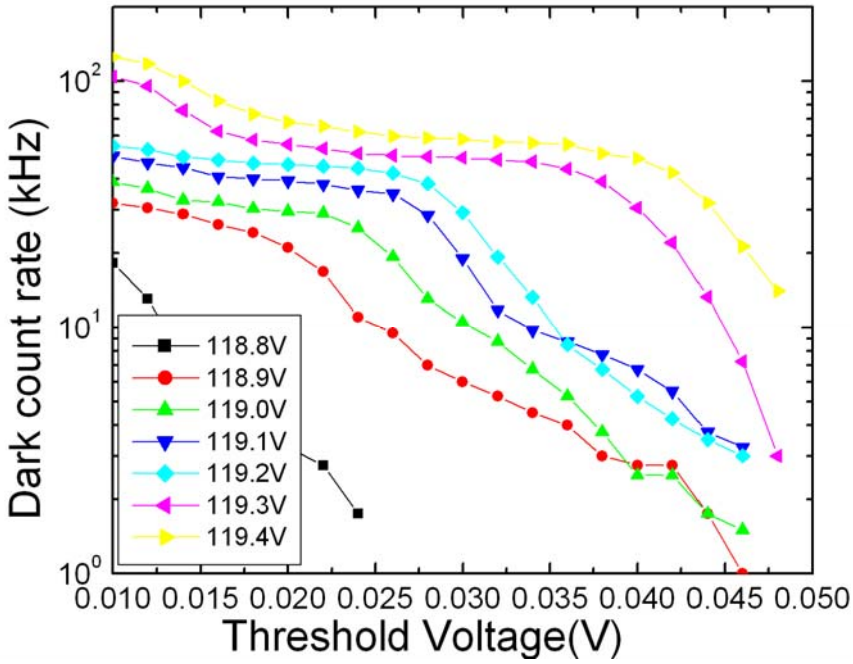

Fig. 3-36 Dark count rate of 4H-SiC SPAD with off-mesa overlay from -118.8V to -119.4V

Fig. 3-36 and **Fig. 3-37**show the DCR and the photon count rate of the 4H-SiC SPAD with off-mesa overlay from 118.8V to 119.4V with the threshold voltage from 0.010 V to 0.046 V. A histogram of the pulse-height distribution at the reverse bias from 118.8V to 119.4V is shown in **Fig. 3-38**. The avalanche gain and the pulse height increase with the applied reverse bias. At the reverse bias of 118.8V, the height of most pulses is between 0.015 V and 0.025 V and the peak is located at 0.021V. When the reverse bias increases to 119.4V, the peak shifts to 0.041V and the height of the most pulses is between 0.036 V and 0.046 V.

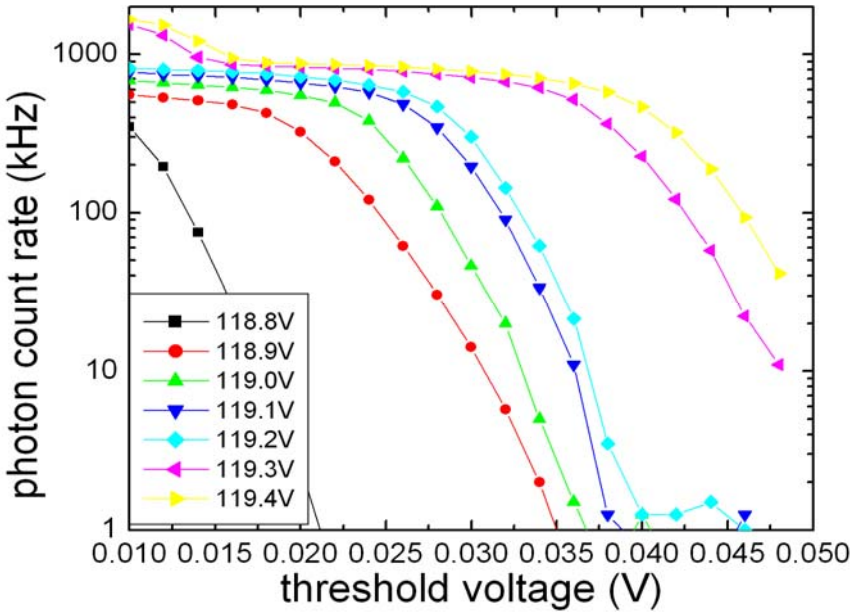

Fig. 3-37 Photon count rate of 4H-SiC SPAD with off-mesa overlay from -118.8V to -119.4V.

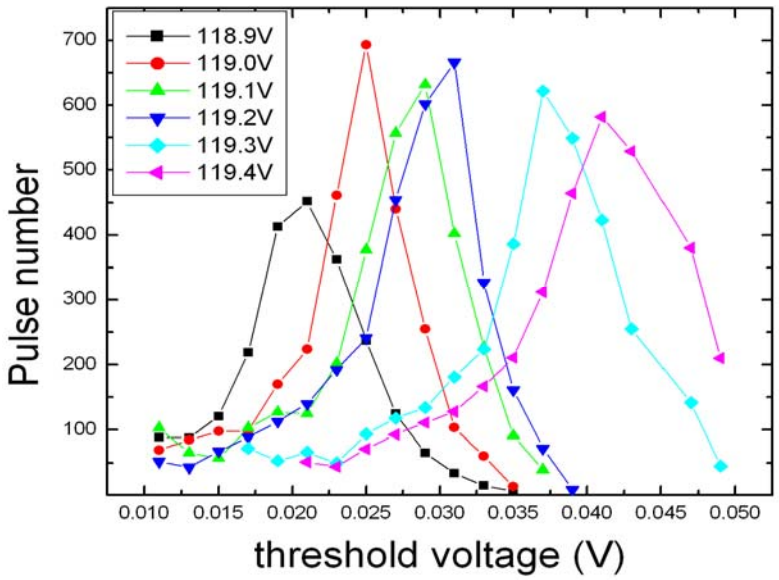

Fig. 3-38 A histogram pulse-height distribution at the bias from -118.8V to -119.4V.

The single photon detection efficiency and counting efficiency shown in **Fig. 3-39** and **Fig. 3-40** are calculated from the photon count rate and the QE. The single photon

counting results at -119.0 V and -119.4V are interesting. When the SPAD is working at -119.0V, with the threshold voltage increasing from 10 mV to 28 mV, the DCR, the SPDE and the CE decrease from 38.75 kHz, 9.7% and 32% down to 13 kHz, 1.6% and 5.2%, respectively.

When the device is working at -119.4 V. with the threshold voltage increases from 10 mV to 46 mV, the DCR, the SPDE and the CE decrease from 125kHz, 23.7% and 79.4% down to 21.3 kHz, 1.33% and 4.46%, respectively.

Table 3-2 Dark count rate, single photon detection efficiency and counting efficiency at 119.0V and 119.4V

	119.0V			119.4V		
Vth (mV)	DCR (kHz)	SPDE (%)	CE (%)	DCR (kHz)	SPDE (%)	CE (%)
10	38.75	9.67	32.5	125.25	23.7	79.4
12	36.5	9.43	31.6	117.5	21.8	73.2
14	32.75	9.12	30.6	100	17.2	57.8
16	32.25	8.78	29.5	83	13.5	45.2
18	30.25	8.43	28.3	73.25	12.6	42.3
20	29.5	7.83	26.3	68	12.4	41.7
22	29	7.03	23.6	65.5	12.2	41.1
24	25.25	5.40	18.1	62.25	12.1	40.5
26	19.25	3.12	10.5	59.75	11.8	39.7
28	13	1.56	5.23	58.75	11.5	38.6
30	10.5	0.653	2.19	58	11.1	37.3
32	8.75	0.284	0.952	56.5	10.6	35.7
34	6.75	0.0710	0.238	56	10.1	33.8
36	5.25	0.0213	0.0714	55.25	9.31	31.2
38	3.75	0.00710	0.0238	50.75	8.20	27.5
40	2.5	0.0177	0.0595	48.5	6.62	22.2
42	2.5	0.00710	0.0238	42.5	4.56	15.3
44	1.75	0.00710	0.0238	32	2.68	8.99
46	1.5	0.00710	0.0238	21.25	1.33	4.46
48	0	0	0	14	0.585	1.96

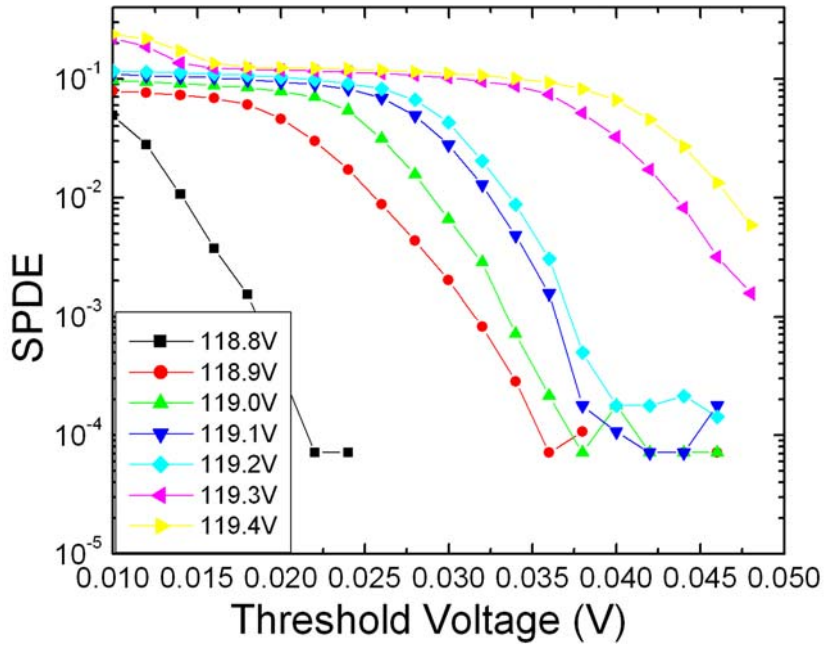

Fig. 3-39 Single photon detection efficiency of the 4H-SiC SPAD with off-mesa overlay from -118.8V to -119.4V.

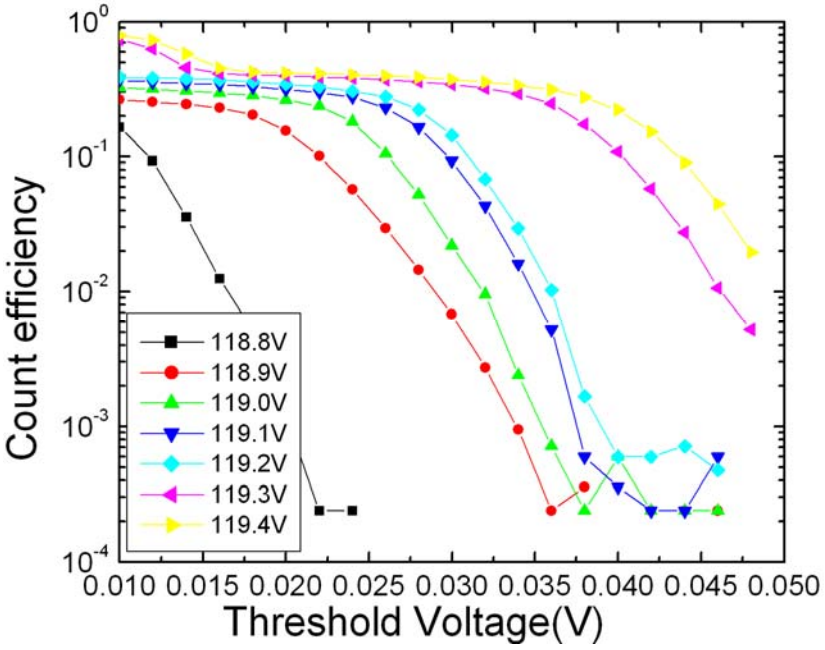

Fig. 3-40 Counting efficiency of 4H-SiC SPAD with off-mesa overlay from -118.8V to -119.4V

3.5 Characteristics of the 4H-SiC SPAD array

The most critical issue in fabricating 4H-SiC SPAD linear arrays is the yield. With aforementioned improved continuous growth technology and process technology, we succeed in fabricating the first 4H-SiC SPAD linear array.

The Pixels of 4H-SiC APD array are terminated by a very shallow negative bevel with the junction area of 9161μm^2. The optical window is 50 μm in diameter. The p ohmic contact is formed at the peripheral of the optical window with the contact area of 3007 μm^2. **Fig. 3-41** shows the top view of the 1×33 4H-SiC single photon avalanche diode array. The spacing between two adjacent pixels is 37 μm, and the period is 165 μm.

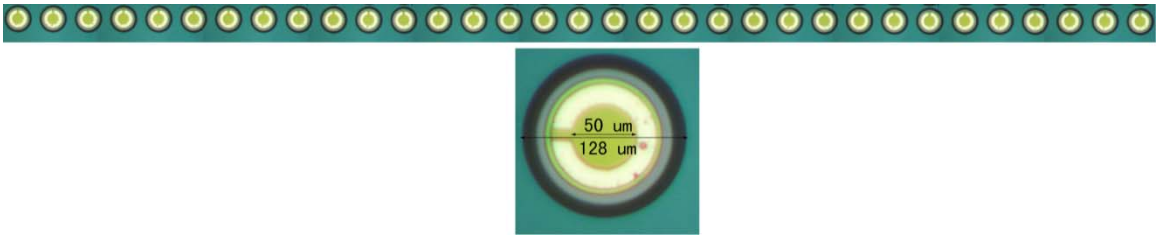

Fig. 3-41 Top view of 1×33 4H-SiC single photon avalanche diode. The pixel is 128 um in diameter and the spacing between two adjacent pixels is 37 um. The optical window is 50 um in diameter.

3.5.1 I-V and Gain characteristics

The reverse I-V characteristics of the 4H-SiC SPAD array are measured from -60 V to -125V and shown in **Fig. 3-42**. All pixels show avalanche breakdown at around -117

V. There is only one bad pixel (pixel #19) out of 33 pixels showing a higher leakage current than others.

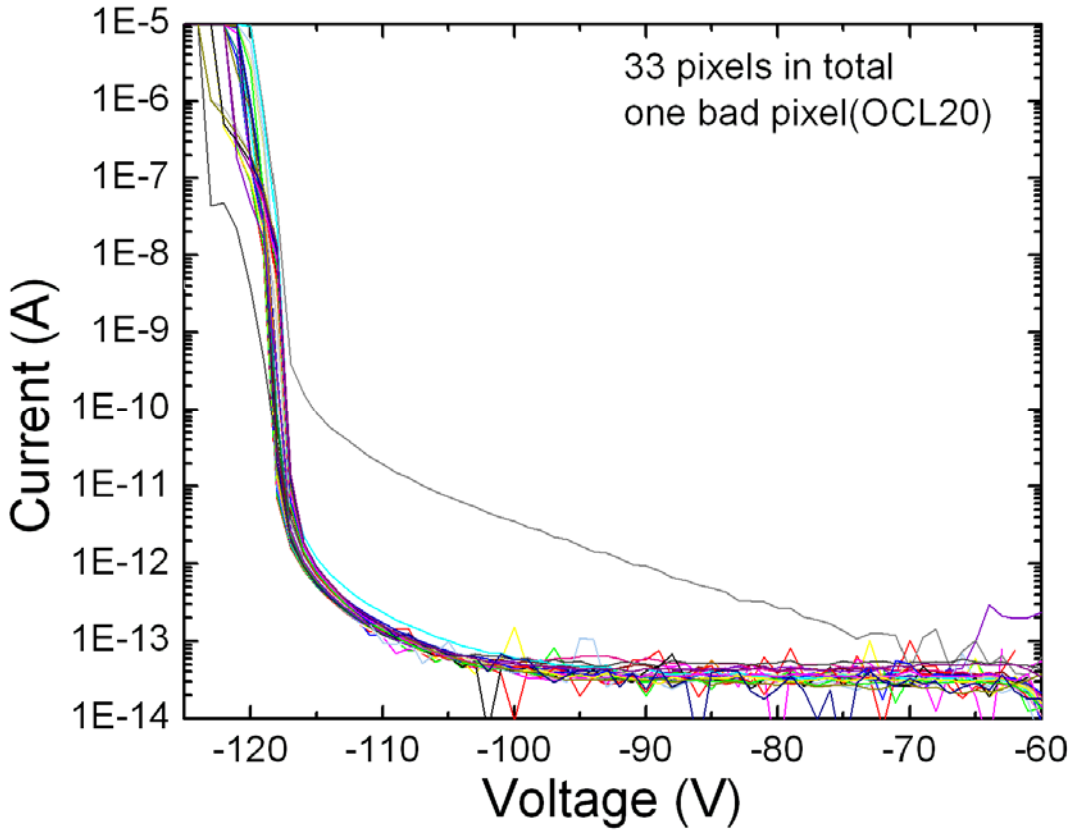

Fig. 3-42 Reverse I-V characteristics of 4H-SiC SPAD array from -60 V to -125V

Fig. 3-43 shows the mapping of the dark current at the breakdown voltage of -117V and 95% of the breakdown voltage. The array (excluding the bad pixel) shows a low leakage current of $< 3\times10^{-13}$ A and <14.0pA at 95% of the breakdown voltage and -117V, respectively.

Gain characteristics of the 4H-SiC SPAD array is measured at 280 nm using UV LED as the light source. From **Fig. 3-44**, we find that all the good pixels show a gain of $>10^6$ at -119.5V.

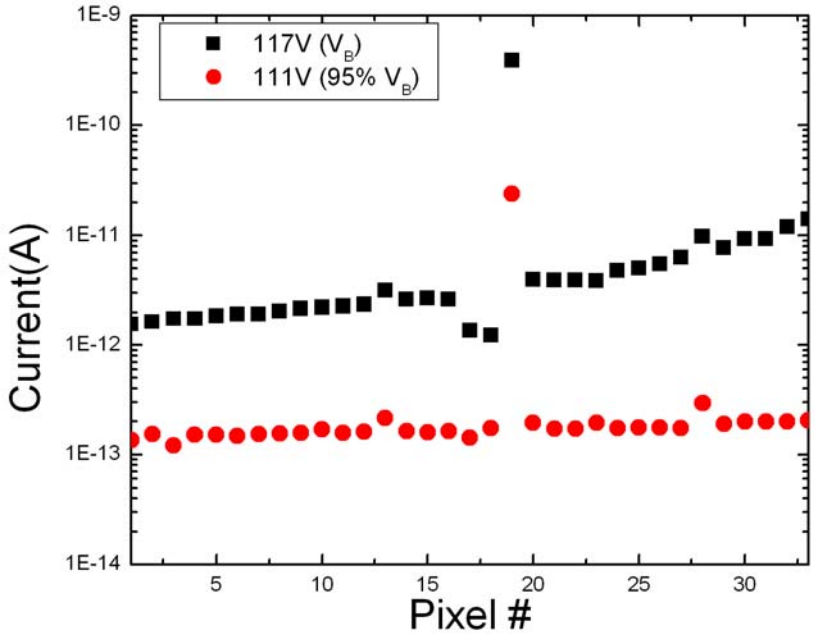

Fig. 3-43 Dark currents of the 4H-SiC SPAD array at the breakdown voltage of -117V and 95% of V_B.

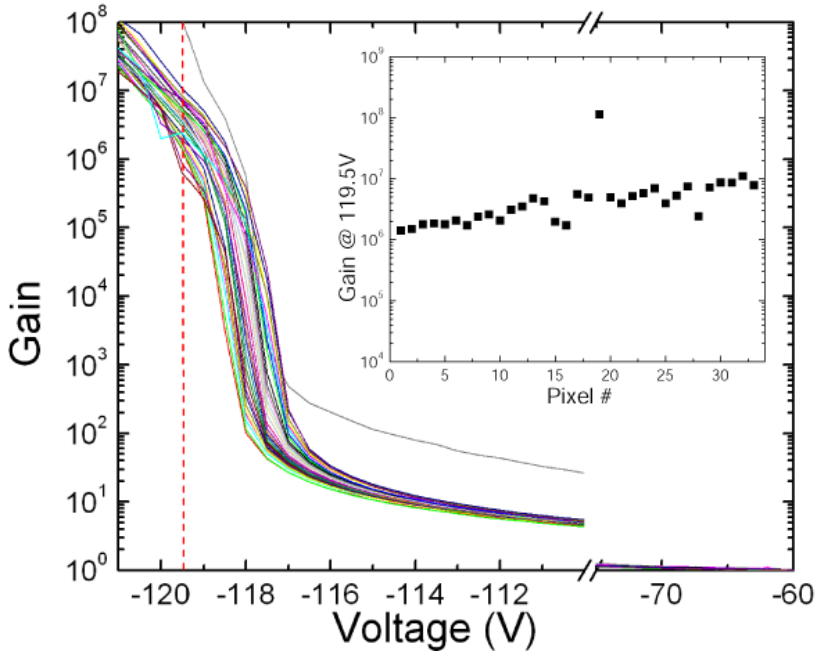

Fig. 3-44 Gain characteristics of the 4H-SiC SPAD array measured at 280 nm.

3.5.2 Single photon counting measurements

Single photon counting measurements of the 4H-SiC SPAD array are performed at room temperature in a passive quenching circuit shown in **Fig. 3-45**. Keithley 6517A electrometer is used to provide a reverse DC bias on the anode of the SPAD. A UV LED peaked at 280 nm is used as the light source. From the previous measurement we find the gain of the SPAD pixels varies from 10^6 to 10^7 at -119.5V. In order to quench the pixels effectively, the passive quenching circuit consists of a 33 kΩ load resistor (R_L). Output voltage pulse signals are recorded through a 50 Ω sensing resistor using a Tektronix DPO 4032 oscilloscope. Each measurement records 4 msec data with a sampling rate of 2.5 Gs/sec.

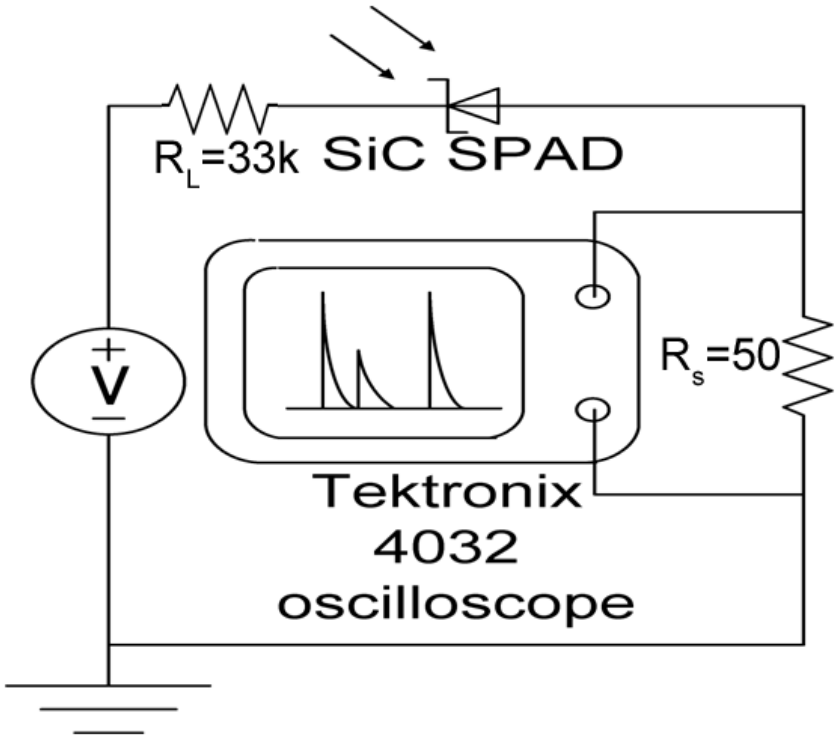

Fig. 3-45 Passive quenching circuit for the 4H-SiC SPAD array measurement

When the reverse bias is 119.5V, with the threshold voltage for photon counting (V_{th}) of 25 mV, the DCR of the array (excluding the bad pixel) is less than 100 kHz (**Fig. 3-46**). The pixel #1 shows the lowest DCR of 30 kHz. The incident UV photon flux is 1.22×10^{8} photons/sec. The photon count rate of all the pixels is also shown in **Fig. 3-46**. The photon count rate is 2.42MHz for the pixel #1 and 8.36MHz for pixel #33, respectively. **Fig. 3-47** shows that the SPDE of the Pixel #1 and the pixel #33 is 2.0% and 7.0%, respectively, which corresponds to the CE of 6.7% and 23%.

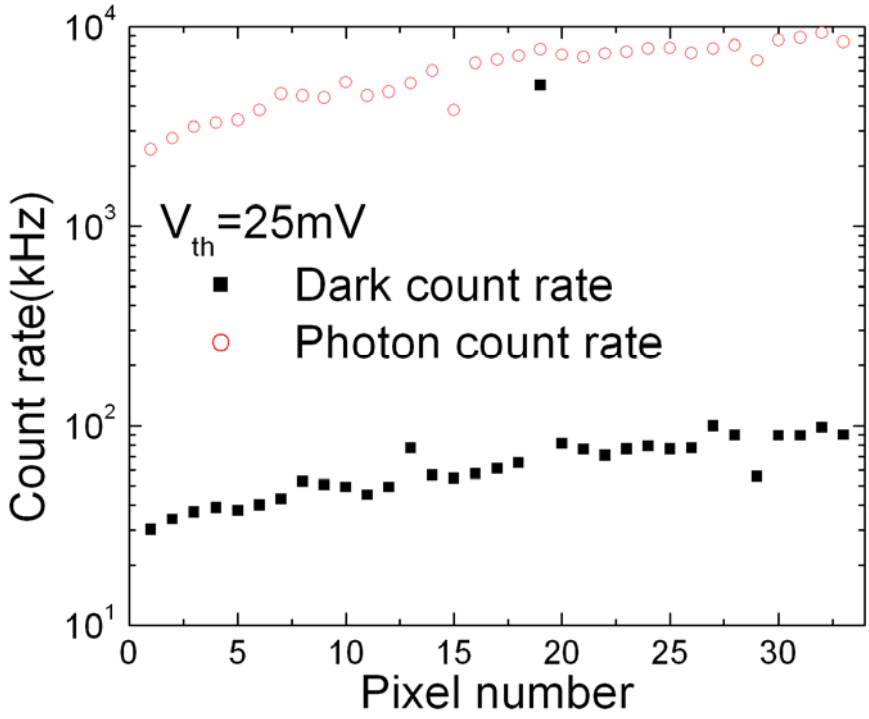

Fig. 3-46 Dark count rate and photon count rate at -119.5V with V_{th}=25mV

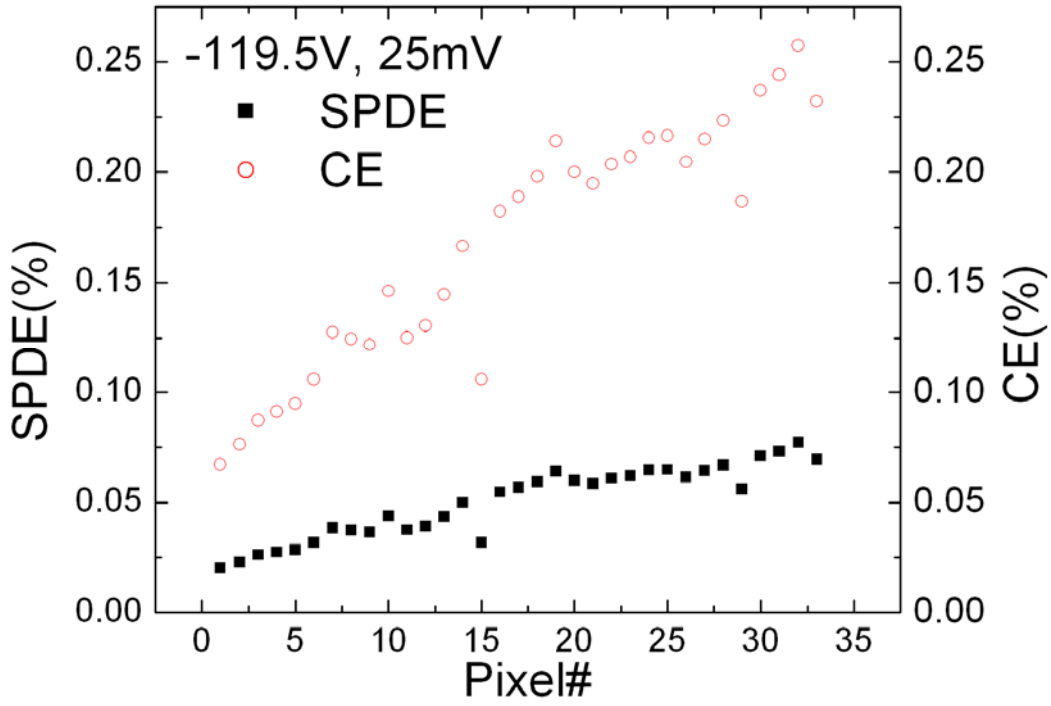

Fig. 3-47 SPDE and CE of 4H-SiC SPAD array.

3.6 Radiation impact to 4H-SiC Single photon avalanche diodes

Radiation effects to 4H-SiC detectors with a variety of radiation types such as high energy proton, neutron, electron and pion have been studied and reported [53-56]. Radiation hardness of 4H-SiC SPADs has never been reported so far. Whereas Si SPADs in a near-earth orbit satellite have shown a 55.5counts/day DCR increment due to cosmic rays (such as mega eV protons) and a distinct DCR increase (2500cts/s per device) in a solar storm. In this section, we present for the first time the effects of proton irradiation on 4H-SiC SPADs.

Proton irradiation experiment to the 4H-SiC SPADs is carried out under no bias condition. The 4H-SiC SPADs are irradiated under 2 MeV protons to a total dose of 1×10^{12} protons/cm^2 with terminals floating. The current-voltage characteristics are studied with a femto-amp resolution before and after the irradiation. Single photon

counting measurements before and after the irradiation are carried out under the same condition. Both of the DCR and SPDE are analyzed carefully.

The forward and reverse I-V characteristics of the 4H-SiC SPADs are measured on-chip using Keithley 4200SCS semiconductor characterization system. More than 10 devices are measured before and after the irradiation. **Fig. 3-48** shows the typical forward I-V characteristics of one 4H-SiC SPAD. After the proton irradiation, the leakage current of the SPAD increases from 13 fA to 32 fA when the forward voltage (V_F) is less than 1.9 V. When V_F is higher than 1.9V, the forward current starts to increase. The forward current of the SPAD after the irradiation is virtually the same as that before the irradiation when V_F is higher than 2.1 V. The ideality factor (n) is extrapolated from the linear fit of *log (I)* as a function of V_F, The value of n is calculated to be 1.6-1.8, indicating the existence of recombination via multiple recombination centers.

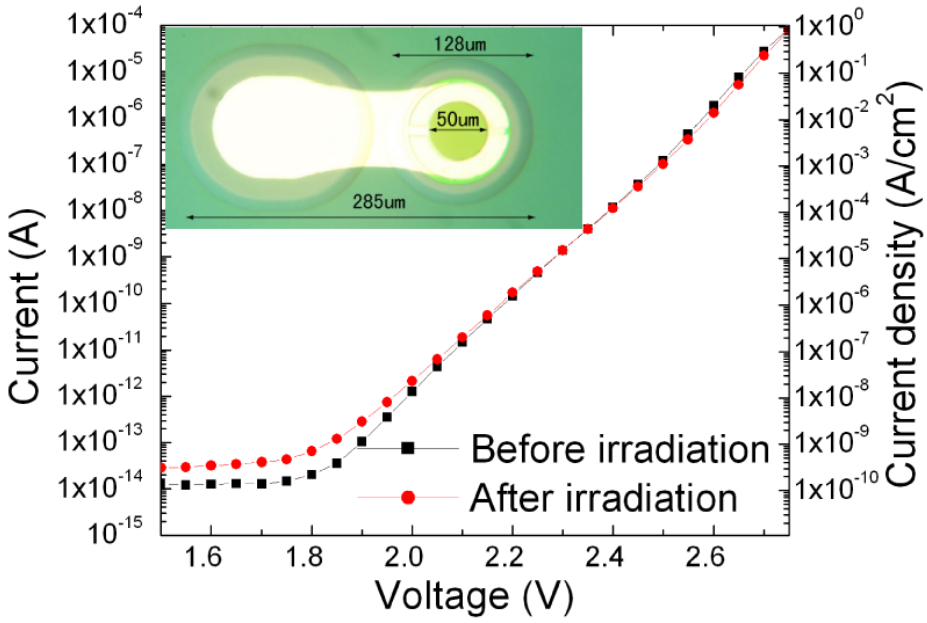

Fig. 3-48 Forward I-V characteristics of 4H-SiC single photon avalanche diode. The inset shows the top view of the 4H-SiC SPAD.

Reverse I-V and gain characteristics of the 4H-SiC SPAD before and after the proton irradiation are shown in **Fig. 3-49**. Before the proton irradiation, the avalanche breakdown of the SPAD occurs at the reverse bias of 113V and the SPAD shows very low leakage current before the avalanche breakdown. At the reverse bias less than 50 V, the leakage current is less than 30 fA. At 90% and 95% of the breakdown voltage, the leakage is 57 fA and 145fA, respectively. After the proton irradiation, the avalanche breakdown voltage of the SPAD is -112.4V, which is 0.6V less than that before irradiation. The leakage current is 1.27 pA at -50V. At 90% and 95% of the breakdown voltage, the leakage is 84.2 pA and 282 pA, respectively, which is higher than that before the irradiation. The optical gain is measured at the wavelength of 280 nm. When the reverse bias is less than 70 V, the photocurrent keeps constant at unit gain. At the gain of 10^6, the leakage current of the SPAD before the irradiation is 93.1 nA. As comparison, after the irradiation, the leakage current at the same gain is 6.98 μA, which is 75 times higher.

Before the proton irradiation, the single photon counting measurements are performed with the incident UV photon flux of 3.08×10^7 photon/sec. The operation condition can be optimized by minimizing the DCR and maximizing the SPDE at the same time. However, because the DCR and SPDE have the same tendency when the reverse voltage and the threshold voltage used for pulse counting change, we can only find a best compromise between them. Simultaneously, the threshold voltage should also be adjusted to discriminate against noise pulses at low voltage level effectively. In this experiment, the 4H-SiC SPAD was working at the optimized condition with the reverse biased of 114.2V and the threshold voltage of > 10mV, which is carefully chosen to

obtain the optimized single photon counting performance for the SPAD. As shown in **Fig. 3-50**, before the proton irradiation, when the threshold voltage at the reverse bias of 114.2V increases from 10 mV to 30 mV, the DCR drops from 68.8 kHz to 26.8 kHz, and the SPDE decreases from 8.75% to 4.70%.

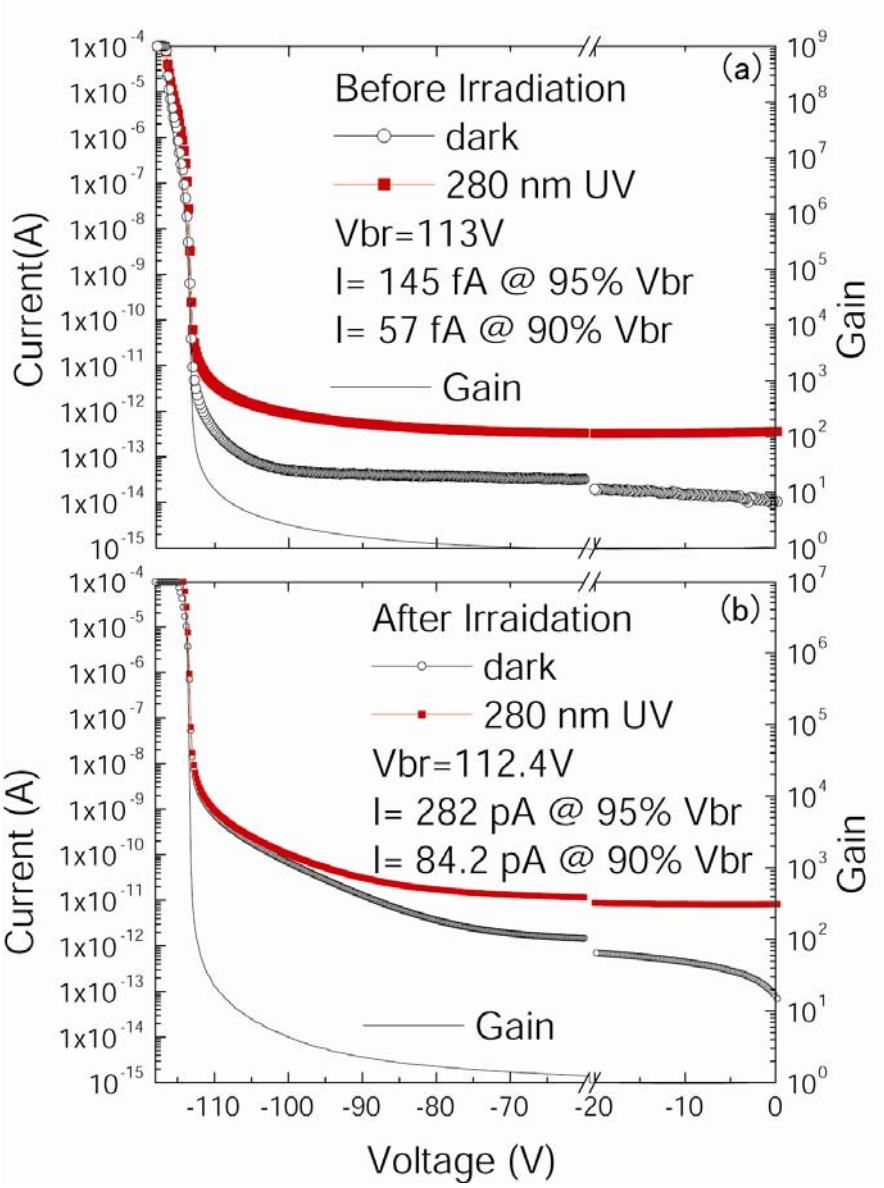

Fig. 3-49 Reverse I-V characteristics and gain performance before and after proton irradiation.

The single photon counting experiments after the irradiation are performed under the same condition. From **Fig. 3-50**, we find that at the threshold voltage less than 17 mV, the DCR is higher than 1MHz, which is much higher that before irradiation. It indicates that the proton irradiation with 2MeV energy and a total dose of 1×10^{12} protons/cm^2 generates some defects in the 4H-SiC SPAD, which will introduce dark carriers during the single photon counting experiments. The DCR is 100 kHz when the threshold voltage is 23 mV and decreases dramatically when the threshold voltage is higher than 27mV. Another important parameter to evaluate the performance of SPADs is the SPDE. The SPDE of 4H-SiC SPAD after the irradiation is less than that before the irradiation, which is shown in **Fig. 3-50**. At the threshold voltage of 10mV, the SPDE after the irradiation is 8.63%. When the threshold voltage is less than 15mV, the difference of the SPDE before and after the irradiation is small. However, the DCR under this condition is too high, indicating a poor signal-to-noise ratio in the single photon counting experiments. The difference of the SPDE before and after the irradiation increases when the threshold voltage increases. When the threshold voltage is 27 mV, the SPDE after the irradiation is less than 1% comparing to 4.89% before the irradiation. Please notice that when the threshold voltage is higher than 27mV, the DCR and SPDE after the irradiation decrease to zero dramatically, whereas before the irradiation, they are 23 kHz and 4.07%, respectively, even at higher threshold voltage of 40mV, which means that the pulse height decreases a lot due to the proton irradiation. It is also worthwhile to notice that after the irradiation there is a threshold voltage window from 24 mV to 26 mV, in which the 4H-SiC SPAD still shows a low DCR (<100 kHz) and a relatively high SPDE (>1%). The SPDE/DCR ratio at 24, 25 and 26 mV after irradiation is

1.86%/54kHz, 1.45%/25.3kHz and 1.07%/10.5kHz, respectively. As comparison, before the irradiation, the SPDE/DCR at 24, 25 and 26 mV is 5.05%/28.3kHz, 5.02%/28.0kHz and 4.96%/27.8kHz, respectively.

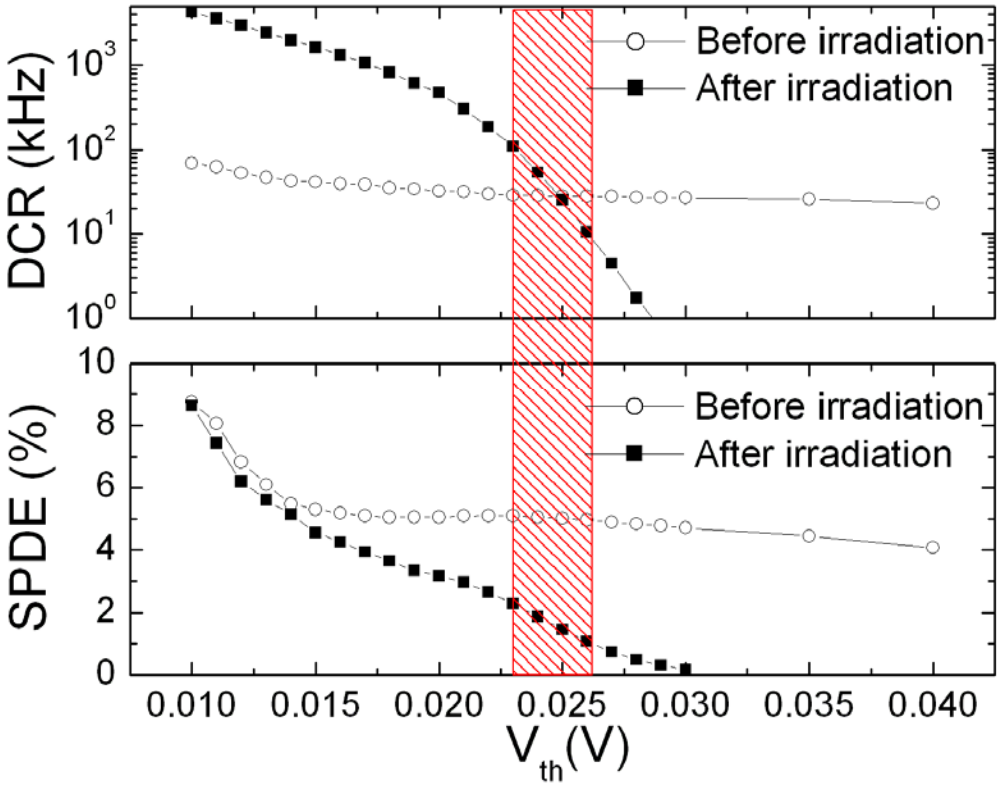

Fig. 3-50 Dark count rate and single photon detection efficiency of 4H-SiC SPAD before and after proton irradiation.

Chapter 4 4H-SiC punch-through phototransistors and avalanche phototransistors

4.1 Design of 4H-SiC avalanche phototransistors

Phototransistor is an optical detection device that provides internal gain and is therefore attractive for many applications [57]. It is a bipolar transistor excited by an optical signal. More often than not, the base contact is not fabricated and there is no base current. This is called the floating-base mode of operation. In a sense, the optical signal acts as the base current in this device. In the phototransistor, the base-collector junction, at which most of the photons are absorbed, is reverse biased. And the generated photocurrent is amplified by transistor action shown in **Fig. 4-1**.

The motivation of this study is to investigate the performance of 4H-SiC phototransistor for low level UV detection. Theoretically, phototransistors have internal transistor current gain. If the BC junction is driven into avalanche breakdown, the photo-generated electron-hole pairs will be multiplied by the avalanche gain. For n-p-n phototransistor structure, electrons are collected by the collector. Holes will be multiplied during the avalanche, and then injected into the base. The total current is amplified by transistor gain.

Therefore, compared with 4H-SiC avalanche photodiodes, 4H-SiC avalanche phototransistors may benefit from:

1. Better n-type ohmic contact on the anode side, instead of poor p ohmic contact of 4H-SiC photodiodes. A good ohmic contact on the anode can improve the dynamic range and the uniformity.
2. With the combination of avalanche gain and transistor gain, a higher gain can be achieved at lower excess voltage, indicating a lower dark count rate.

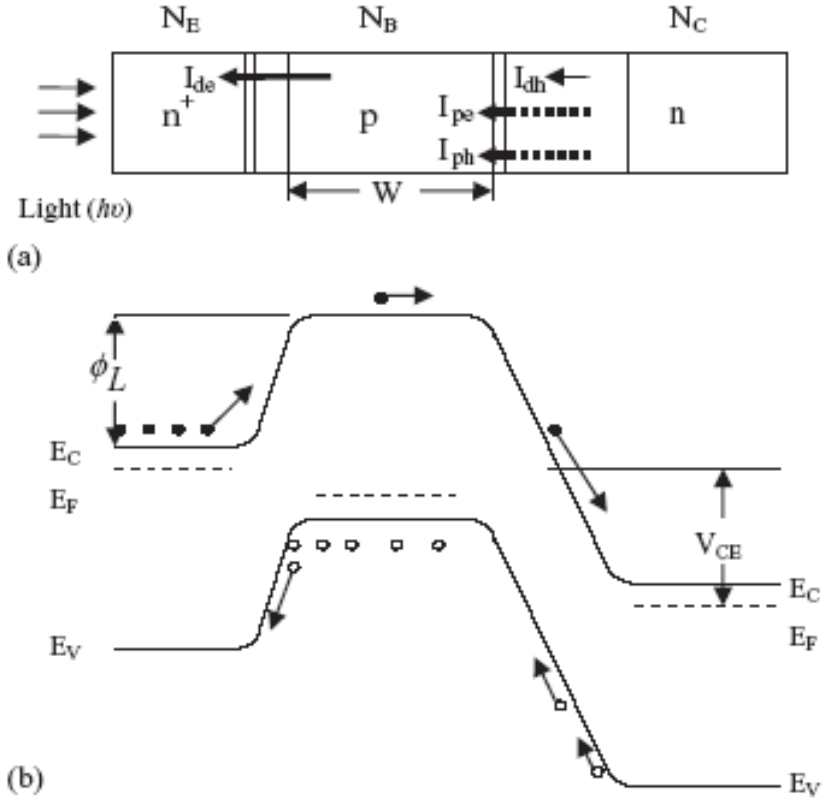

Fig. 4-1 Schematic diagram (a) and energy band diagram (b) of a phototransistor. I_{de} and I_{dh} are electron and hole dark current, respectively. I_{pe}, I_{ph}, is electron and hole photocurrent, respectively.

We design the avalanche phototransistor structure shown in **Fig. 4-2**. The avalanche phototransistor has a 0.3 μm N+ emitter layer with 2×10^{19} cm^{-3} doping, a 0.46 μm p base layer with 5×10^{17} cm^{-3} doping, and a 0.46 μm n- drift layer with 5×10^{14} cm^{-3}

doping grown on n+ buffer layer with 1×10^{18} cm^{-3} doping. The phototransistor structure is designed with a breakdown voltage of -209.8V and a critical electrical field of 2.9 MV/cm.

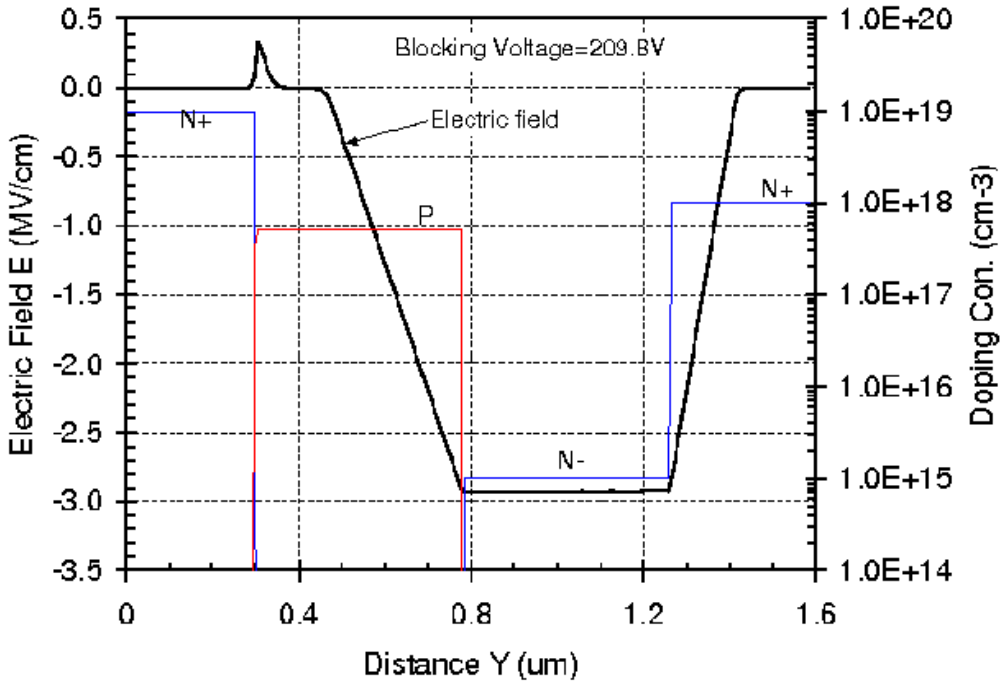

Fig. 4-2 Structure design of 4H-SiC single photon avalanche transistor and electrical field cross the bulk according to computer simulations.

Simulation of transistor gain (β) based on the above avalanche transistor structure is shown in **Fig. 4-3**, β=17 at 161V. If we can take advantage of the combination of transistor gain and avalanche gain, 4H-SiC avalanche phototransistors can have higher gain and lower dark count rate than 4H-SiC avalanche photodiodes.

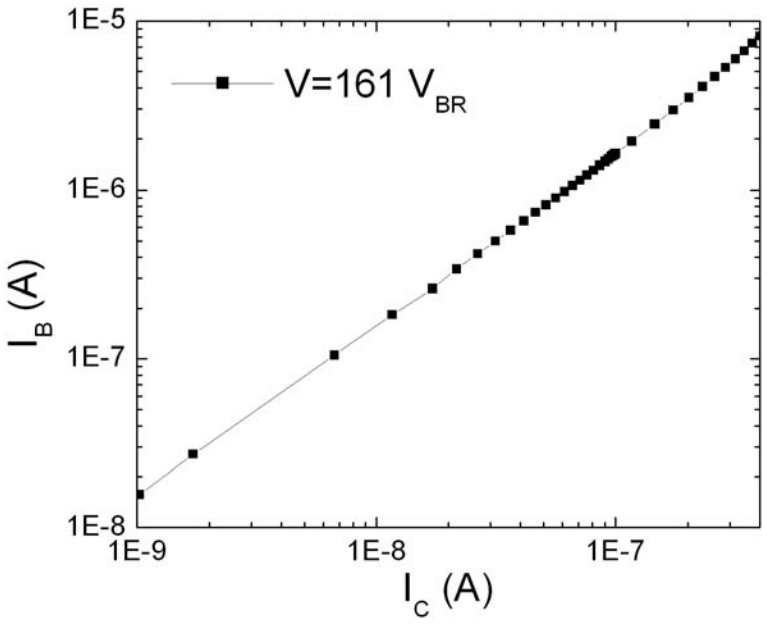

Fig. 4-3 Simulation of transistor gain shows β=17 at 161V.

The 4H-SiC phototransistors with on-mesa overlay and off-mesa overlay are shown in **Fig. 4-4**.

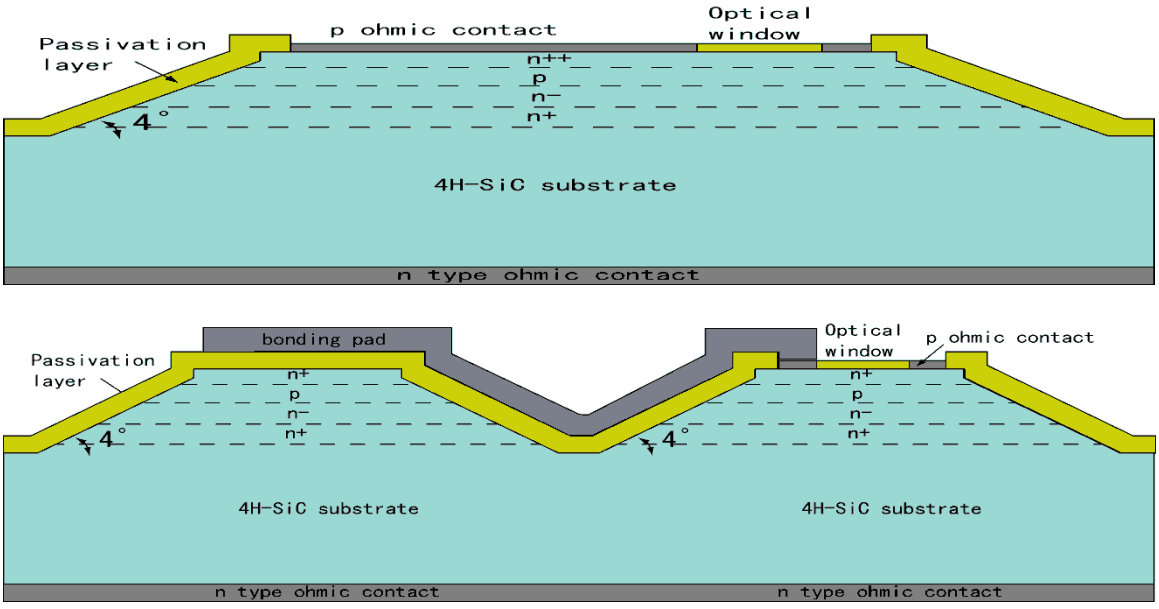

Fig. 4-4 Cross sectional view of designed 4H-SiC avalanche transistors

4.2 Fabrication of 4H-SiC avalanche phototransistors

4.2.1 Fabrication procedure of 4H-SiC avalanche phototransistors

Fabrication procedure of 4H-SiC phototransistors is the same as that of avalanche photodiodes, except that for our phototransistors both of the emitter contact and collector contact are made from annealed Ni simultaneously.

The epilayer structure of phototransistors is grown on an n+ 4H-SiC commercial substrate in an Aixtron/Epigress VP508 hot-wall CVD reactor. Nitrogen and trimethylaluminum are used as n-type and p-type dopant sources, respectively.

Two 4H-SiC phototransistor wafers, 2080201 and 2080423, are grown for avalanche phototransistor fabrication. The epilayer thickness and doping concentration from our design and SIMS analysis are shown in **Table 4-1**. From the SIMS analysis shown in **Fig. 4-5**, we find that the base doping and thickness of the wafer 2080201 are less than the designed structure. With this structure, the device will reach punch-through before avalanche breakdown occurs. The SIMS analysis from **Fig. 4-6** indicates that the p base doping and thickness of the other wafer 2080423 is higher than the designed structure.

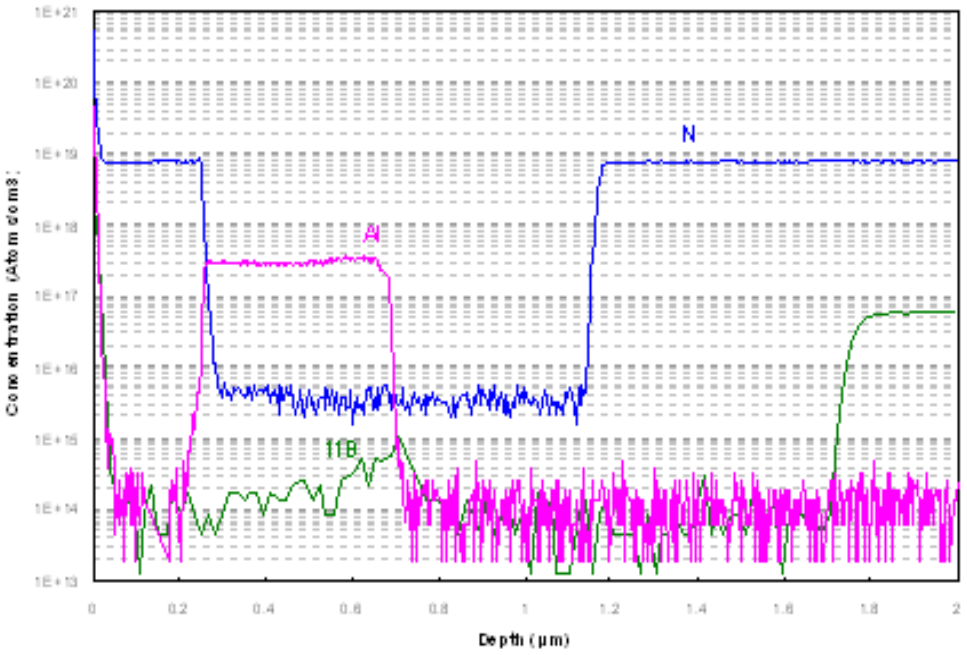

Fig. 4-5 Doping profile of 4H-SiC phototransistor wafer 2080201.

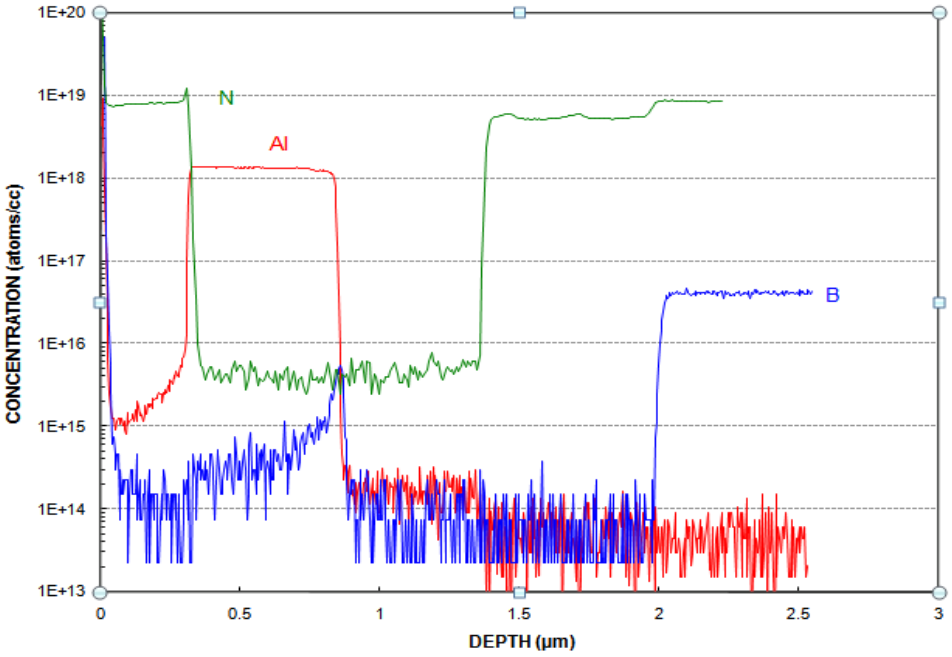

Fig. 4-6 Doping profile of 4H-SiC phototransistor wafer 2080423.

Table 4-1 Comparison of the epilayer structures of our design and the two actual wafers

	Designed		2080201 (SIMS)		2080423 (SIMS)	
	Doping (cm^{-3})	Thickness (μm)	Doping (cm^{-3})	Thickness (μm)	Doping (cm^{-3})	Thickness (μm)
Top n++ emitter	1e19	0.3	7.7e18	0.28	8.0e18	0.30
P base	7e17	0.48	2.9e17	0.41	1.3e18	0.5
n-	4e14	0.48	4.5e15	0.45	5.0e15	0.55
n+ collector	1e18	NA	7.3e18	NA	6e18	0.6

4.2.2 Ohmic contact formation

For the avalanche phototransistor structure, the top n++ emitter layer is only 0.3 μm thick, and the emitter contact is 100 nm Ni. During the ohmic contact annealing, SiC is consumed and NiSi is formed. In order to prevent NiSi consuming the entire 0.3 μm n+ emitter layer during the ohmic contact annealing, the emitter contact need to be very thin. A 100nm Ni layer is sputtered and annealed at different temperature in Ar (95%) + H_2 (5%) gas for 5 minutes using a RTA system (**Fig. 4-7** to **Fig. 4-9**). A very good n-type ohmic contact can be achieved after annealing at the temperature between 900^{o}C to 1000^{o}C.

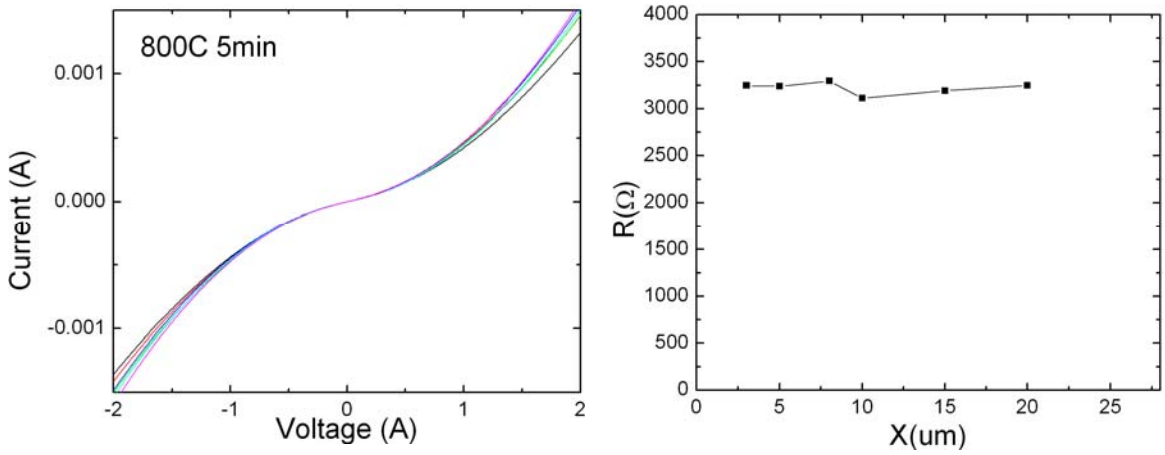

Fig. 4-7 TLM measurement results of n-type ohmic contact annealed at 800°C and extrapolated specific contact resistivity

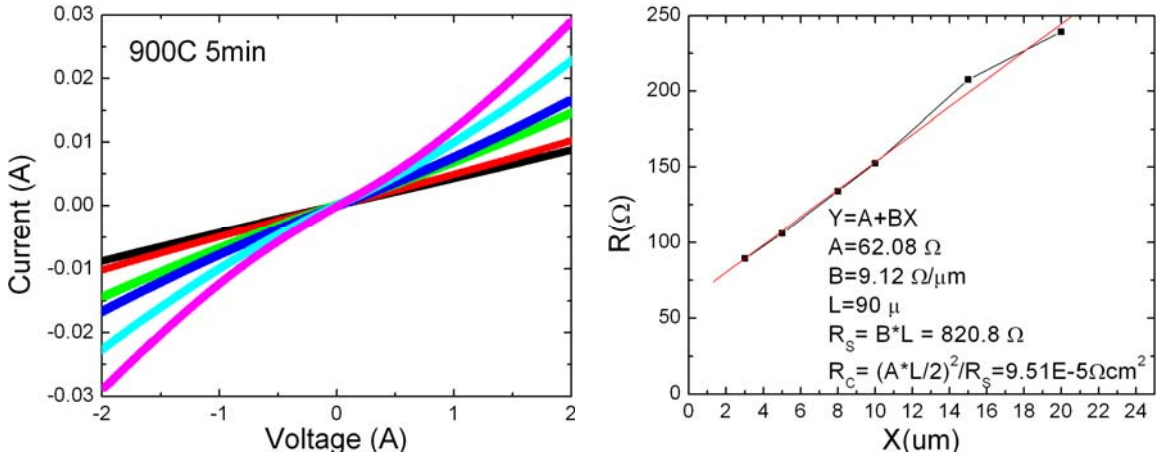

Fig. 4-8 TLM measurement results of n-type ohmic contact annealed at 900°C and extrapolated specific contact resistivity.

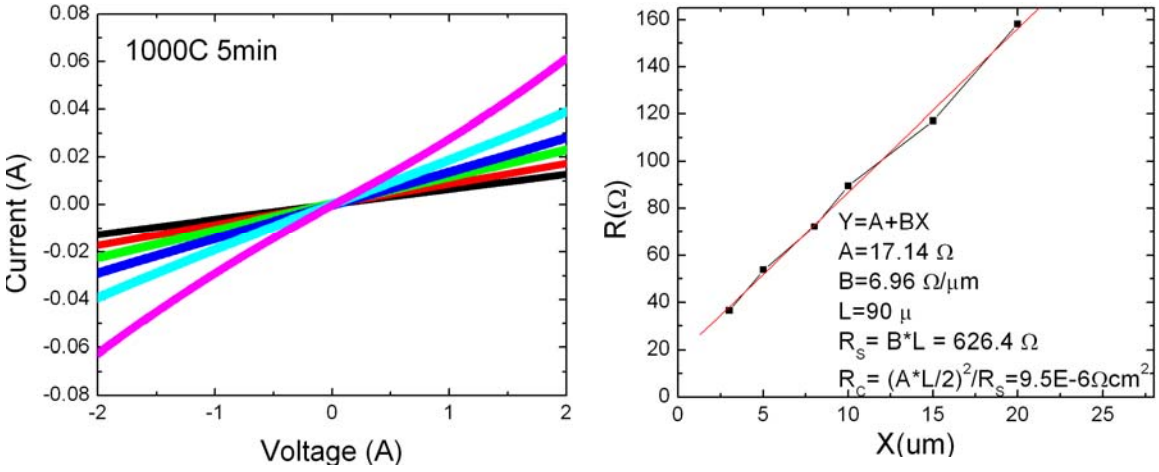

Fig. 4-9 TLM measurement results of n-type ohmic contact annealed at 1000°C and extrapolated specific contact resistivity

4.3 I-V and gain characteristics of 4H-SiC punch-through phototransistors

4.3.1 Reverse I-V characteristics of 4H-SiC punch-through phototransistors

4H-SiC punch-through phototransistors are fabricated on the wafer 2080201. The reverse I-V characteristics of 4H-SiC phototransistors are shown in **Fig. 4-10**. The leakage current is very low when the reverse bias is less than 110V. Once the reverse bias is higher than 110V, the current starts to increase dramatically. However, this voltage is much smaller than the designed avalanche breakdown voltage. The band diagram and the schematic electric field are shown in **Fig. 4-11**.The following calculation and analysis for

the n-p-n structure show that the p base is totally depleted at -102V and the phototransistor is punch through before avalanche breakdown happens.

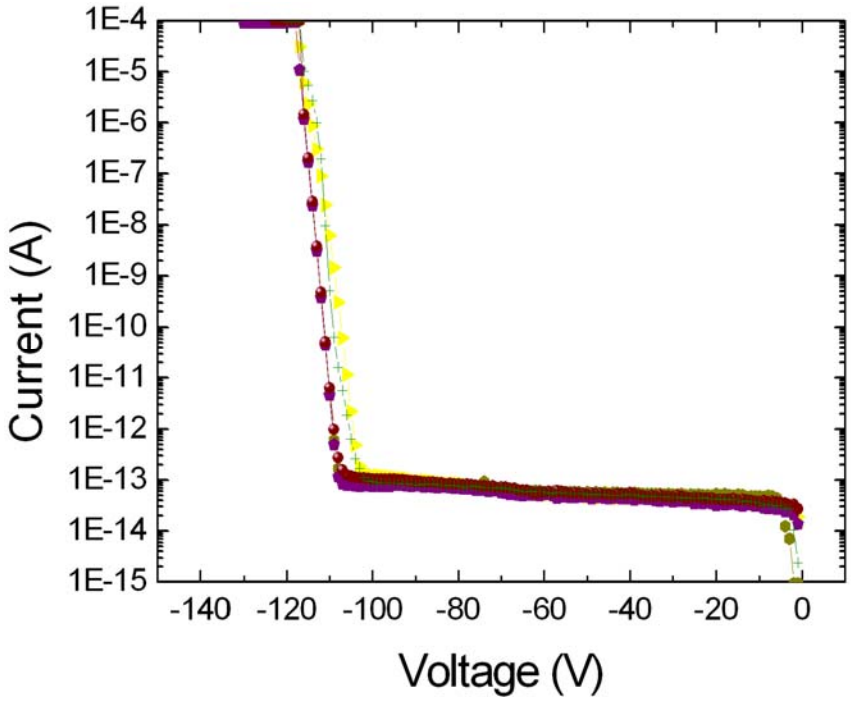

Fig. 4-10 Reverse I-V characteristics of 4H-SiC punch-through phototransistor.

(1) Calculation of the depletion width, W_p, in the p base at the BE junction:

Assuming the voltage at the punch-through breakdown is applied on the reverse biased BC junction, the build-in voltage, V_{bi}, at the BE junction is calculated to be

$$V_{bi} = \frac{kT}{q}\ln\left(\frac{N_A N_D}{n_i^2}\right) = 0.0259\times\ln\left(\frac{7.7\times10^{18}\times2.9\times10^{17}}{(1\times10^{-8})^2}\right) = 3V,$$

where T is the absolute temperature, N_A is the base doping, N_D is the emitter doping, and n_i is the intrinsic carrier density at room temperature.

The depletion width in the p base at the BE junction, W_p, is

$$W_p \approx \sqrt{\frac{2\varepsilon}{q}\frac{1}{N_A}V_{bi}} = \sqrt{\frac{2\times 8.854\times 10^{-14}\times 9.7}{1.6\times 10^{-19}\times 2.9\times 10^{17}}\times 3} = 1\times 10^{-5}\,cm = 0.1\mu m$$

(2) Calculation of the punch-through breakdown voltage:

At the punch-through, the depletion width, W_p' in the p base at the BC junction is

$W_p' = 0.41 - W_p = 0.41 - 0.1 = 0.31\mu m$,

and the critical electric field at punch through breakdown, E_{cr}, is

$$E_{cr} = \frac{qN_pW}{\varepsilon} = \frac{1.6\times 10^{-19}\times 2.9\times 10^{17}\times 0.31\times 10^{-4}}{9.7\times 8.854\times 10^{-14}} = 1.67MV/cm$$

.

The voltage drop on the p base, V_p, is

$$V_p = \frac{1}{2}E_{cr}W_p' = 0.5\times 1.67\times 10^6\times 0.31\times 10^{-4} = 25.9V$$

.

Since the thickness of the n- drift layer, W_n, is 0.45μm, the voltage drop on the fully depleted n- layer, V_n, is

$V_n \approx E_{cr}\times W_n = 1.67\times 10^6\times 0.45\times 10^{-4} = 75.1V$.

The total punch-through, V_{BR}, is

$V_{BR} = V_p + V_n = 25.9V + 75.1V = 101V$.

The calculated pouch-through breakdown voltage of 101V is very close to the experimental result of 110 V.

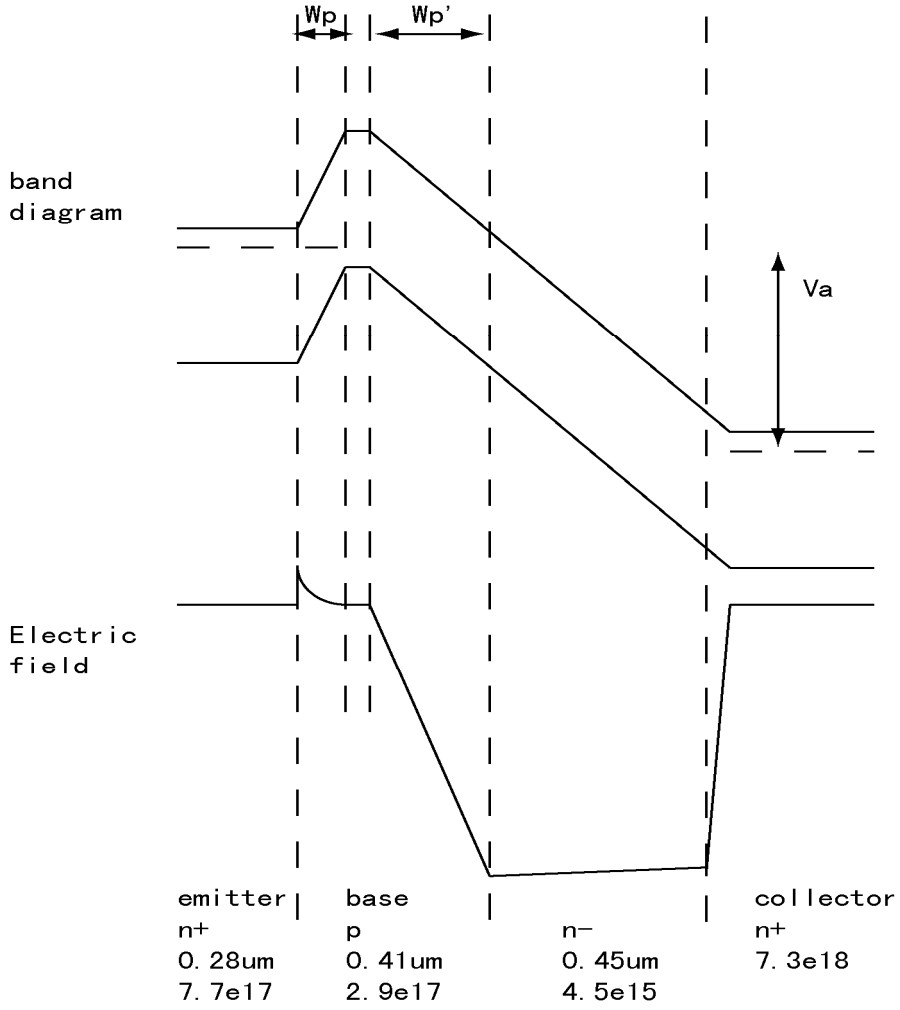

Fig. 4-11 Band diagram and electric field of 4H-SiC phototransistor structure.

4.3.2 Gain characteristics of 4H-SiC punch-through phototransistors

For a conventional phototransistor under normal operation conditions, the carrier transport of the device is dominated by thermionic emission. This is confirmed by the observation that the current increases with the substrate temperature at a given bias

condition [58], following the expression for thermionic emission. The current density of thermionic emission is given by

$$J = A^{*}T^{2}\exp(-q\Phi_{L}/kT) \ ,$$

where A* is the effective Richardson constant, T is absolute temperature, and Φ_L is the barrier height associated with the emission process.

When photons with energy greater than the SiC energy band gap impact on the incident window of the device, they generate electron-hole pairs in the depletion region of B-C junction and within the diffusion lengths of the minority carriers in the base and collector. Photo-generated electrons drift to and are collected by the back collector electrode, while the photo-generated holes drift to and are trapped in the potential well in the base. As shown in **Fig. 4-12**, accumulated holes lower the potential barrier height Φ_L , leading to a significant increase of the device current.

The photon current of a phototransistor is defined as

$$J_{ph} = J_{n} - J_{nd} = J_{nd} \cdot \{\exp(q\Delta\Phi_{L}/k_{B}T) - 1\} \ .$$

Those holes in the potential minimum can leave the potential minimum by several different mechanisms.

1. Holes can recombine with electrons. However, the probability of the recombination process is very small, because electrons would be swept to the collector by the high electric field.
2. Holes can diffuse to the emitter side and escape the potential well.
3. Holes can inject over the potential barrier by thermionic emission.

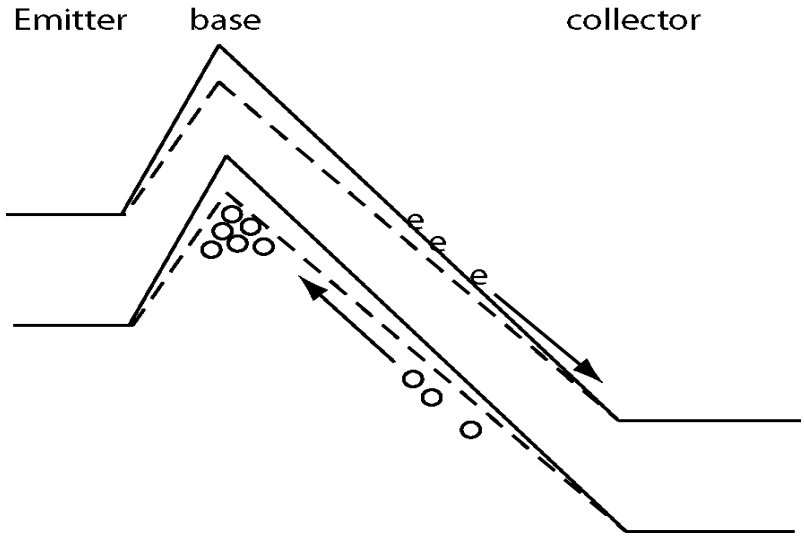

Fig. 4-12 Barrier lowing due to the hole accumulation in the base

In steady state the total flux of holes moving toward the potential well should be equal to that leaving the potential minimum. Balance of hole flux, therefore, leads to the following equation [59, 60]:

$$P_i \eta / h\nu + J_{pd} / q = \Delta p / \tau_{eff},$$

where η is the internal quantum efficiency associated with the absorption process in the B-C junction, hν is ht photon energy, J_{pd} is the dark current of holes, q is the electron charge, and Δp is the number of holes accumulated at the potential well, and τ_{eff} is the effective life time. The effective life time is defined as

$$\frac{1}{\tau_{eff}} = \frac{1}{\tau_r} + \frac{1}{\tau_t} + \frac{1}{\tau_{te}} + \frac{1}{\tau_D},$$

where τ_r, τ_t, τ_{te} and τ_D are lifetimes associated with recombination, trapping, thermionic emission, and diffusion processes, respectively.

Assuming the accumulated holes form a Fermi gas, we get:

$$\Delta p = \frac{\tau_{eff} J_{pd}}{q} \exp(\frac{q\Delta\Phi_L}{n_f k_B T}),$$

hence,

$$\Delta\Phi_L = \frac{n_f k_B T}{q} \ln(1 + \frac{P_{inc}\eta q}{J_{pd} h\nu}).$$

The optical gain Γ_G of the phototransistor is the ratio of the number of photon generated carriers to the number of incident photons. Thus,

$$\Gamma_G = \frac{h\nu}{q}\frac{J_{ph}}{P_{inc}} = \frac{h\nu}{q}\frac{J_{nd}}{P_{inc}}\left[\left(1 + \frac{P_{inc}\eta q}{J_{pd} h\nu}\right)^{n_f} - 1\right].$$

When n_f=1, $\Gamma_{G\max} = \eta\frac{J_{nd}}{J_{pd}}$.

For a p-i-n photodiode, electrons and holes are generated in pairs and no gain is involved, J_{nd}=J_{pd}. Therefore, as expected for a p-i-n photodiode, the optical gain reduces to quantum efficiency, η.

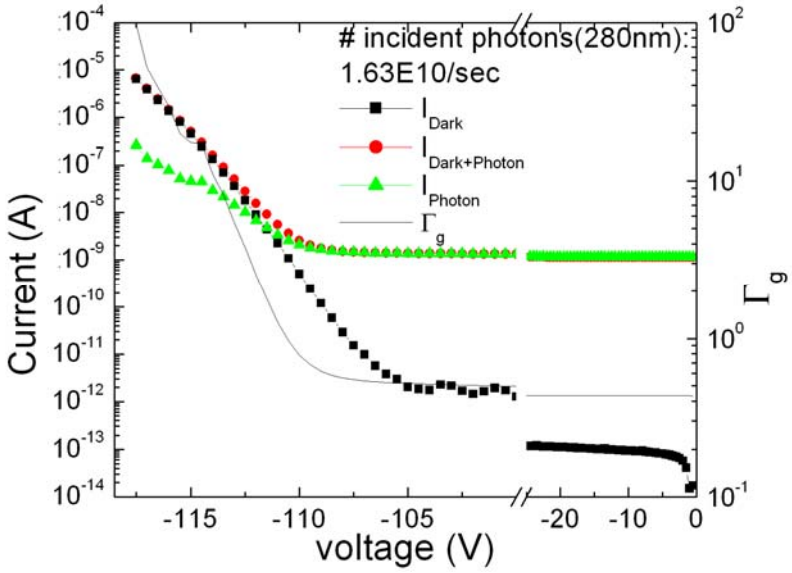

Fig. 4-13 I-V characteristics with and without UV illumination and gain characteristics.

In order to evaluate the optical gain of the fabricated 4H-SiC punch-through phototransistor, I-V characteristics with and without UV illumination from zero bias to punch-through are shown in **Fig. 4-13**. Before the punch-through, the optical gain is very low. At zero bias, the optical gain is 0.43. The optical gain starts to increase when the voltage is higher than -110V. The optical gain is higher than 1 at V=-112V, and reaches 100 at V=-117.5V. Because the quantum efficiency of the phototransistor is hard to evaluate, we can only estimate that at V=-117.5V the current gain of phototransistor is higher than 100/0.43 =230.

We also measure the photoresponse of the phototransistor at low bias from 240 nm to 390 nm, which is shown in **Fig. 4-14**.

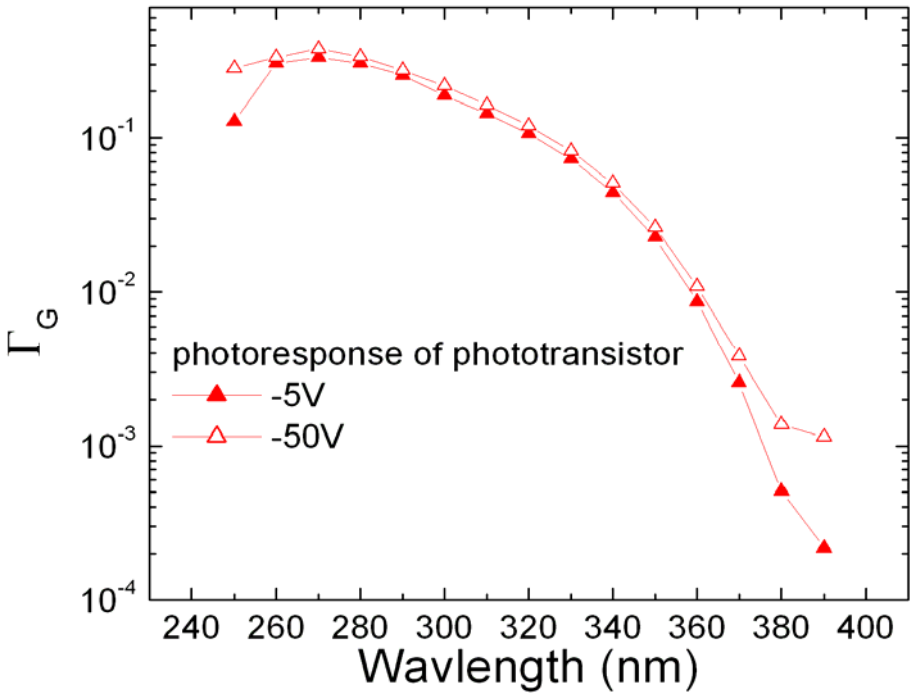

Fig. 4-14 Photoresponse at low bias of the phototransistor at UV range from 240 nm to 390 nm

4.4 I-V and gain Characteristics of 4H-SiC avalanche phototransistors

4H-SiC avalanche phototransistors are fabricated on the wafer 2080423. Since the critical field of SiC is almost 10 times higher than that of Si, edge termination process is very critical to prevent surface breakdown. A 4^o negative bevel is used to terminate the device edge. The phototransistor does not have a base contact and its base-collector junction is driven into avalanche breakdown. **Fig. 4-15** and **Fig. 4-16** show the simulation results of the electric field distribution across the phototransistor in the bulk and at the surface using ISE-TCAD software. The important parameters used in the simulations are shown in **Table 4-2**. The theoretical avalanche breakdown of the phototransistor occurs at -160V with the bulk critical electric field of 2.88 MV/cm at the base-collector junction and the electric field of 0.39 MV/cm at the base-emitter junction. At the same time, the peak of the surface electric field is 1.02 MV/cm and is 0.08 μm away from the base-collector junction into the p-base due to the electric field extension on the 4^o shallow negative bevel.

Table 4-2 Important parameters for avalanche phototransistor simulation with ISE-TCAD

Electron lift time (μsec)	Hole lift time (μsec)	Electron mobility (cm^2/Vs)	Electron mobility (cm^2/Vs)	Temperature (K)
2.5	0.5	947	124	300

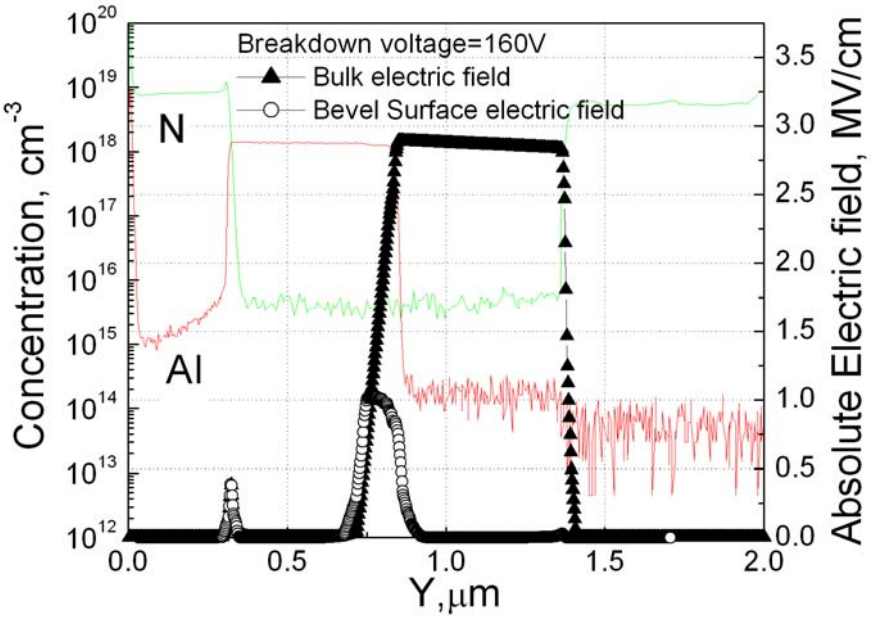

Fig. 4-15 Doping profile and electric field in the bulk and on the bevel surface

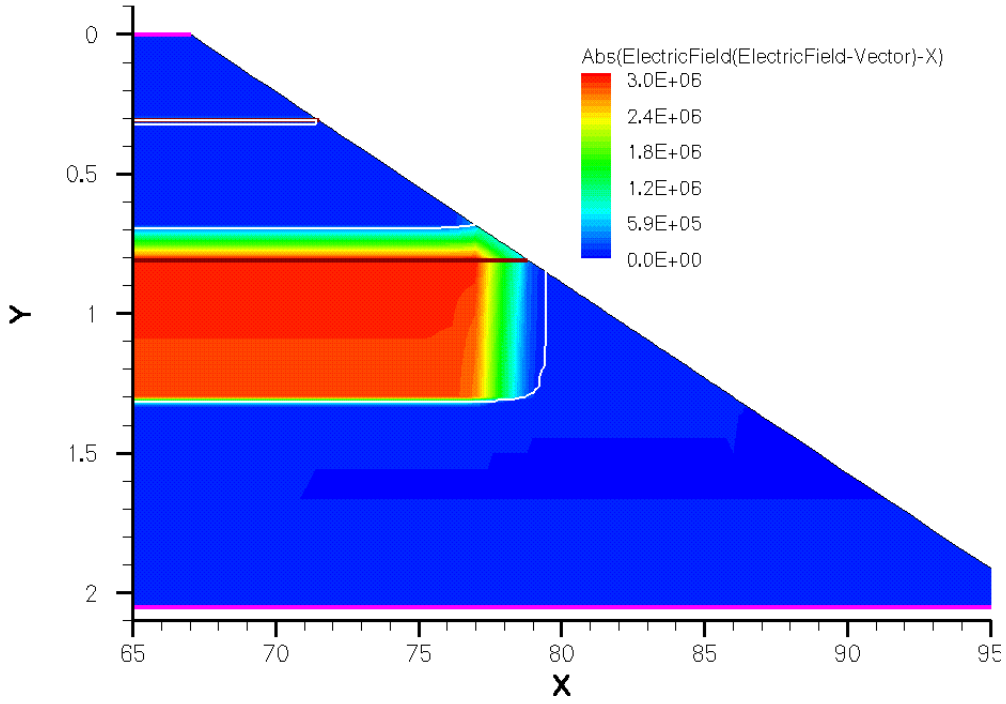

Fig. 4-16 Electric field distribution on the bevel surface at the avalanche breakdown

The reverser I-V characteristics of the 4H-SiC avalanche phototransistor with and without UV illumination are shown in **Fig. 4-17**. The phototransistor is characterized at the chip level using Keitheley 4200SCS Semiconductor characterization system. The leakage current at –5 V is 45 fA, which corresponds to a low current density of 0.22 nA /cm^2, if p-n junction area (2.0×10^4 μm^2) is considered. When the reverse bias is less than 100 V, the leakage current is lower than 0.21 pA. Avalanche breakdown occurs at -154 V. At 90% of the breakdown voltage, the leakage current is 8.5 pA, which corresponds to a current density of 42 nA/cm^2.

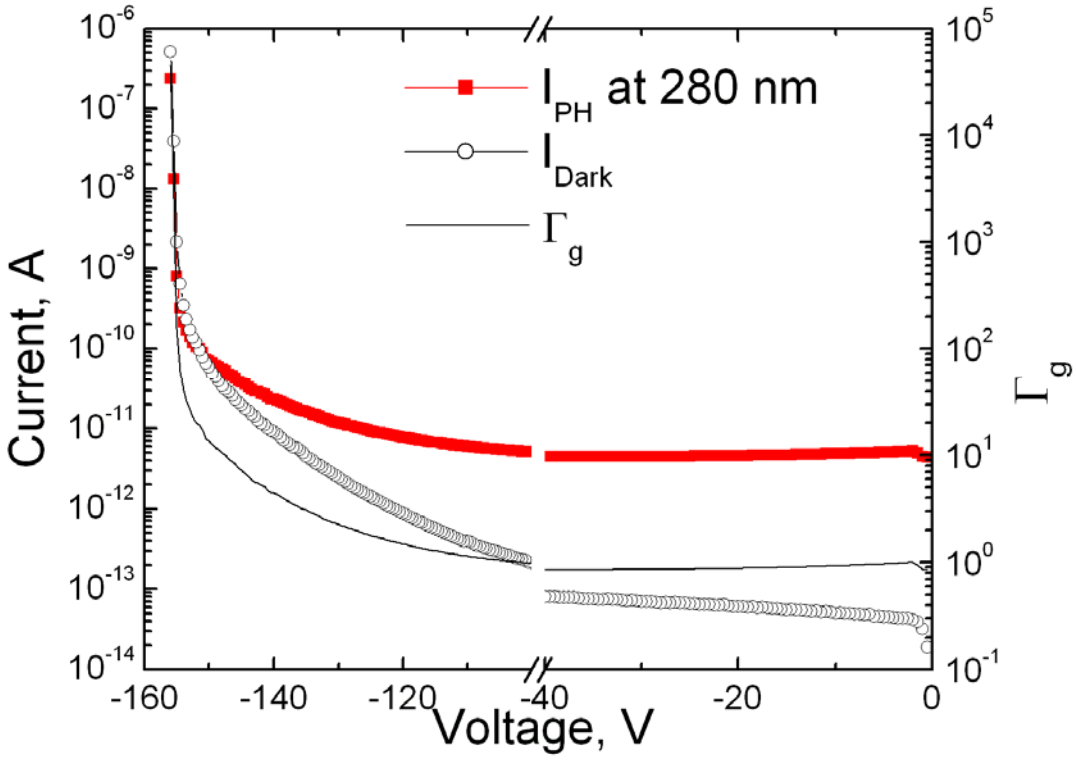

Fig. 4-17 I-V and gain characteristics of the 4H-SiC avalanche phototransistor

The photoresponse spectra of the 4H-SiC avalanche phototransistor from 250 nm to 400 nm are measured using a 150 W UV enhanced Xenon arc lamp with a 2400/mm

near UV monochromator as the light source. The UV monochromic light is coupled into an optical fiber and then focused on the device through an UV objective. The QE is shown in **Fig. 4-18**. The inset is the incident UV light power measured by a Si UV enhanced photodiode calibrated from 200 nm to 400 nm. The QE peak of 36.4% occurs at the wavelength of 260 nm. Given that the QE is <0.0037% at 400 nm, the UV-to-Visible rejection ratio is higher than 9.8×10^3.

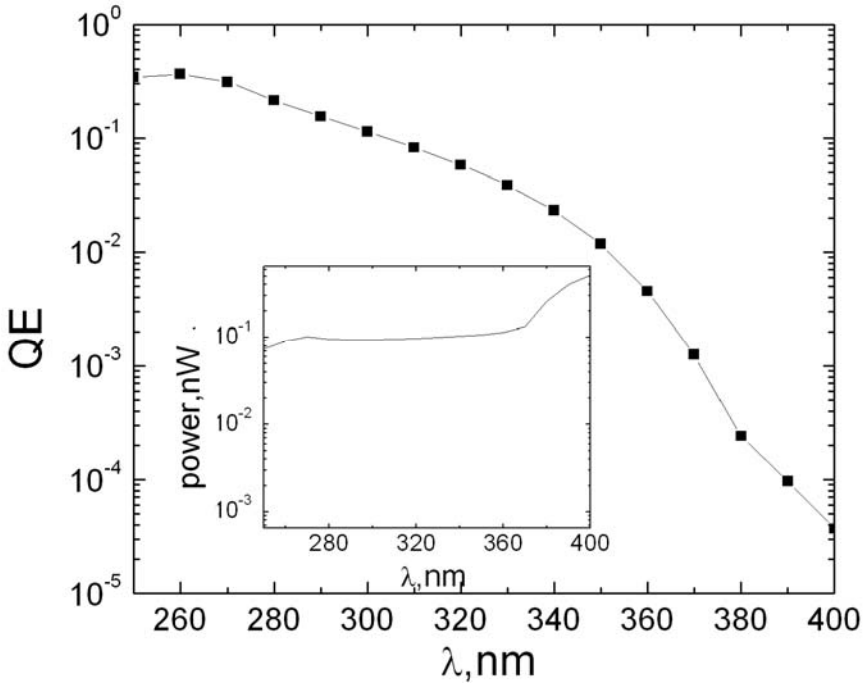

Fig. 4-18 Quantum efficiency of the 4H-SiC avalanche phototransistor

In this work, the 4H-SiC avalanche phototransistor is working under the floating-base mode of operation. The base-collector junction is reverse biased to the avalanche breakdown. Most of the incident UV light is absorbed in the drift layer between the base and collector junction, and the generated photocurrent is multiplied by avalanche gain and transistor gain. The optical gain of the 4H-SiC avalanche phototransistor, Γg, is

define as the ratio of the number of photon generated carriers to the number of incident photons. Thus,

$\Gamma_g=(hv/q)(I_{ph}/P_{inc})=\eta \bullet G_T$,

where I_{ph} is the photocurrent, P_{inc} is the incident UV light power, η is the quantum efficiency of the avalanche phototransistor at unit gain, and G_T is the gain of the avalanche phototransistor. The avalanche phototransistor gain is measured using a UV LED peaked at the solar blind wavelength of 280 nm. The incident UV light power is 23.3 pW. **Fig. 4-17** shows the optical gain characteristics of the avalanche transistor from 0V to -156V. When the applied reverse bias is 5V, the optical gain Γ_g is 0.91, and the corresponding G_T is 4.6 if the QE of 21.4% at 280 nm is taken into account. It indicates that the transistor gain dominates at low bias before the avalanche breakdown. Γ_g and G_T increase to 4.5×10^4 and 2.1×10^5 respectively at -156V when the base-collector junction is driven into the avalanche breakdown, at which the avalanche gain dominates G_T of the 4H-SiC avalanche phototransistor.

Chapter 5 Conclusion and future work

5.1 Conclusion

In this thesis work, high performance 4H-SiC photodetectors for low-level UV detection including Schottky photodiodes, avalanche PIN photodiodes and avalanche phototransistors have been designed, fabricated and characterized. The major achievements of this thesis work include:

1. The first 4H-SiC Schottky photodiode that can fully cover EUV to NUV range has been successfully fabricated. High quantum efficiency and high UV-to-visible rejection ratio have been achieved.
2. The first 1×16 4H-SiC Schottky photodiode array with very large detection area has been successfully fabricated and characterized. A novel UV spectrographic system using 4H-SiC Schottky photodiode array is demonstrated with a fine spectrum resolution.
3. 4H-SiC avalanche photodiodes are studied for UV single photon detection. Many challenging issues including bevel edge termination and ohmic contact have been addressed. 4H-SiC SPADs show high gain, low dark count rate, high single photon detection efficiency and high counting efficiency. The best 4H-SiC SPAD shows a high counting efficiency of >79% and 32.5% with a dark count rate of 125.3 kHz and 38.8 kHz at 119.4V and 119.0V, respectively.
4. The first 4H-SiC SPAD array has been successfully fabricated and characterized. Only 1 pixel out of 33 pixels shows high leakage and high dark count rate. All the

other good pixels show avalanche breakdown at around -117V and ultralow leakage current. For all the good pixels working at -119.5V, the gain is greater than 10^6, the dark count rate is less than 100 kHz and the SPDE is more than 2%.

5. The proton irradiation impact to 4H-SiC single photon avalanche diodes is investigated for the first time.
6. 4H-SiC avalanche phototransistors are designed, fabricated and characterized in this research. The avalanche phototransistor shows a high gain of 4.5×10^4.

5.2 Future work

We succeeded in fabricating 1×16 4H-SiC Schottky photodiode array with large detection area. The performance of the array can be further improved in the following aspects:

1. The cross talk between two adjacent pixels can be reduced. Pixels can be isolated from each other by trenched streets, and the surface can be coated with an Al film, which can prevent the penetration of UV light into the street.
2. The resolution of spectroscopic system is determined by the linear dispersion， resolution of the optics as well as the internal resolution of the detector and the sampling size of the pixels. For sensor-limited resolution, the width of the photodiode pixels can be reduced from our current 750 μm to 40 μm and the number of the pixels can be increased to keep the total detection area the same. Potentially, a dispersion of 0.08 nm/pixel with a corresponding 2-pixel resolution of 0.16 nm can be achieved. Moreover, the leakage current per pixel of the SiC

photodiode array will also decrease significantly, since it scales with the area of the Schottky contact.

4H-SiC SPADs with high performance have been fabricated and characterized. Some ideas for further experimental and theoretical studies are described here:

1. It should be point out that in my thesis work all the avalanche photodiodes and phototransistors are terminated by a shallow negative bevel edge termination. Due to the improved process and design, the avalanche photodiode shows a low leakage and good single photon counting performance. Our simulation shows that the surface electric field on the 4^{o} shallow negative bevel is 30% of the bulk electric field, which means the bevel etching is very critical to the device performance and the process margin is limited.

   However, if positive bevel edge termination with the same bevel angle is used, the surface electric field will drop to less than 10% of the bulk electric field according to our simulation. For the avalanche photodiode or phototransistor structure (**Fig. 5-1**) terminated by positive bevel, the peripheral leakage current and dark count rate can be reduced and the yield will be improved.

   In addition, the drift layer is closer to the surface, and the quantum efficiency can be improved.

2. Since active quenching enables single photon counting at high frequency without after-pulsing problem, it is worthwhile to investigate the performance of SiC SPADs under the active quenching mode.

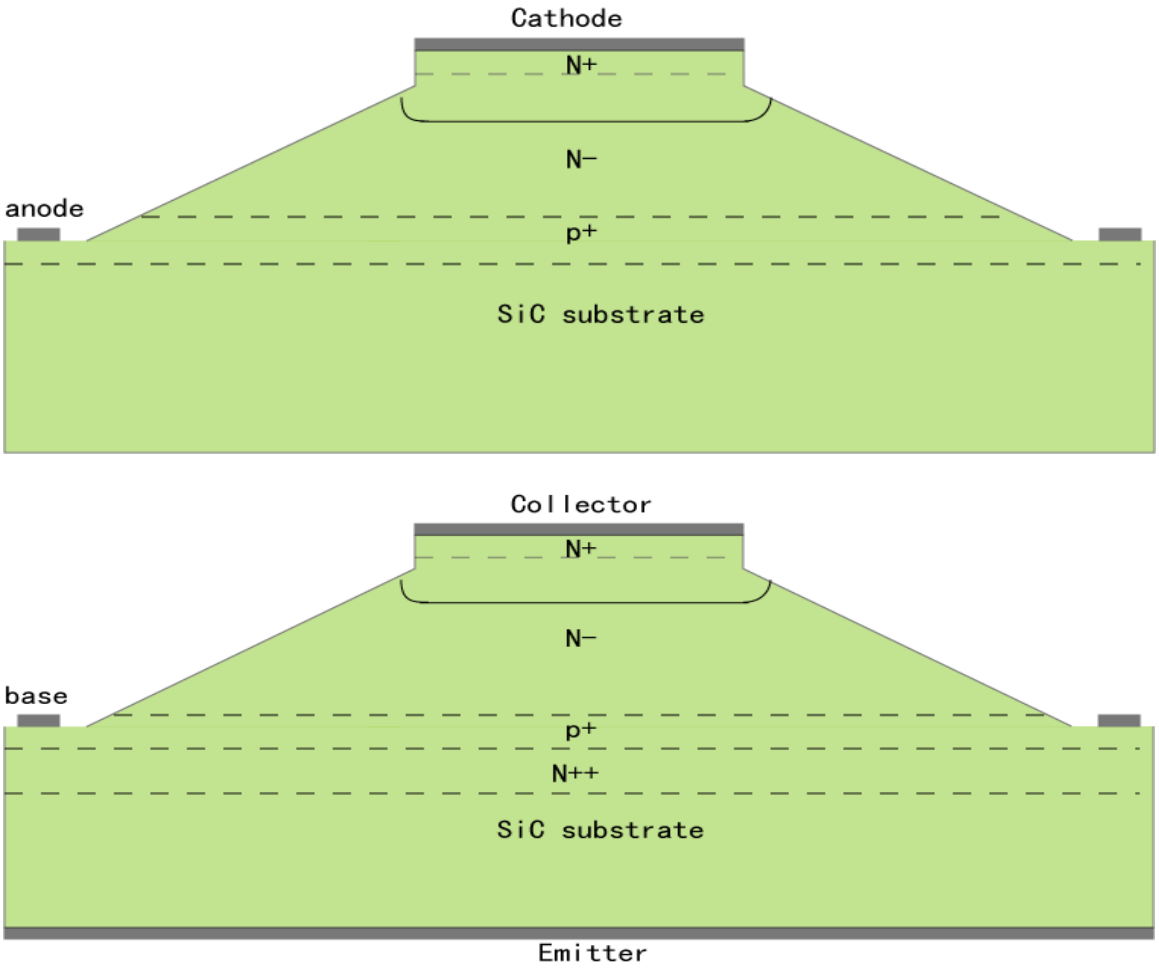

Fig. 5-1 Schematic cross sectional view of avalanche photodiode and phototransistor terminated by positive bevel edge.

References

[1] M. Razeghi and A. Rogalski, "Semiconductor ultraviolet detectors," *Journal of Applied Physics,* vol. 79, p. 7433, 1996.

[2] H. S. Ogawa, D. L. Judge, D. R. McMullin, P. Gangopadhyay, and A. B. Galvin, "First-year continuous solar EUV irradiance from SOHO by the CELIAS/SEM during 1996 solar minimum," *Journal of Geophysical Research-Space Physics,* vol. 103.

[3] R. Viereck, "GOES EUV Sensor Overview presentation," in *GOES-R Workshop* Boulder, CO, 2002.

[4] P. T. Landsberg, "Handbook of Geophysics and the Space Environment. Edited by A. S. Jursa," *Appl. Opt.,* vol. 27, p. 1597, 1988.

[5] D. M. Brown, E. Downey, J. Kretchmer, G. Michon, E. Shu, and D. Schneider, "SiC flame sensors for gas turbine control systems," *Solid-State Electronics,* vol. 42, pp. 755-760, 1998.

[6] P. Schreiber, T. Dang, T. Pickenpaugh, G. A. Smith, P. Gehred, and C. W. Litton, "Solar-blind UV region and UV detector development objectives," in *Photodetectors: Materials and Devices IV*, San Jose, CA, USA, 1999, pp. 230-248.

[7] G. A. Shaw, M. L. Nischan, M. A. Iyengar, S. Kaushik, and M. K. Griffin, "NLOS UV communication for distributed sensor systems," in *Integrated Command Environments*, San Diego, CA, USA, 2000, pp. 83-96.

[8] G. R. Fisher and P. Barnes, "Towards a unified view of polytypism in silicon carbide," *Philosophical Magazine Part B,* vol. 61, pp. 217 - 236, 1990.

[9] C. Basceri, I. Khlebnikov, Y. Khlebnikov, P. Muzykov, M. Sharma, G. Stratiy, M. Silan, and C. Balkas, "Growth of micropipe-free single crystal silicon carbide(SiC) ingots via physical vapor transport(PVT)," *Materials science forum,* vol. 527, pp. 39-42, 2006.

[10] F. Yan, X. Xin, P. Alexandrov, C. M. Stahle, B. Guan, and J. H. Zhao, "Development of Ultra High Sensitivity UV Silicon Carbide Detectors," *Materials Science Forum,* vol. 527-529, p. 3, 2006.

[11] S. G. Sridhara, R. P. Devaty, and W. J. Choyke, "Absorption coefficient of 4H silicon carbide from 3900 to 3250 Å," *Journal of Applied Physics,* vol. 84, p. 2963, 1998.

[12] E. D. Palik, *Handbook of optical constants of solids II*: Academic Press Boston, 1991.

[13] A. Ionascut-Nedelcescu, C. Carlone, A. Houdayer, H. J. A. v. B. H. J. von Bardeleben, J. L. A. C. J. L. Cantin, and S. A. R. S. Raymond, "Radiation hardness of gallium nitride," *Nuclear Science, IEEE Transactions on,* vol. 49, pp. 2733-2738, 2002.

[14] X. Sun, P. L. Jester, S. P. Palm, J. B. Abshire, J. D. Spinhirne, and M. A. Krainak, "In orbit performance of Si avalanche photodiode single photon counting modules(SPCM) used in the Geoscience Laser Altimeter System on ICESat," *Proceedings of SPIE, the International Society for Optical Engineering,* pp. 63720-63720, 2006.

[15] Z. Luo, T. Chen, A. C. Ahyi, A. K. Sutton, B. M. Haugerud, J. D. Cressler, D. C. Sheridan, J. R. Williams, P. W. Marshall, and R. A. Reed, "Proton radiation effects in 4H-SiC diodes and MOS capacitors," *Nuclear Science, IEEE Transactions on,* vol. 51, pp. 3748-3752, 2004.

[16] F. Yan, X. Xin, S. Aslam, Y. Zhao, D. Franz, J. H. Zhao, and M. Weiner, "4H-SiC UV photo detectors with large area and very high specific detectivity," *Quantum Electronics, IEEE Journal of,* vol. 40, pp. 1315-1320, 2004.

[17] J. F. Seely, B. Kjornrattanawanich, and R. Korde, "Silicon carbide photodiodes: future solar-blind EUV/soft x-ray detectors," *Proceedings of SPIE,* vol. 5901, p. 59010B, 2005.

[18] X. Xin, F. Yan, T. W. Koeth, C. Joseph, J. Hu, J. Wu, and J. H. Zhao, "Demonstration of 4H SiC visible-blind EUV and UV detector with large detection area," *Electronics Letters,* vol. 41, pp. 1192-1193, 2005.

[19] J. C. Jackson, D. Phelan, A. P. Morrison, R. M. Redfern, and A. Mathewson, "Toward integrated single-photon-counting microarrays," *Optical Engineering,* vol. 42, p. 112, 2002.

[20] T. Isoshima, Y. Isojima, K. Hakomori, K. Kikuchi, K. Nagai, and H. Nakagawa, "Ultrahigh sensitivity single-photon detector using a Si avalanche photodiode for the measurement of ultraweak biochemiluminescence," *Review of Scientific Instruments,* vol. 66, p. 2922, 1995.

[21] S. Verghese, K. A. McIntosh, R. J. Molnar, L. J. Mahoney, R. L. Aggarwal, M. W. Geis, K. M. Molvar, E. K. Duerr, and I. Melngailis, "GaN avalanche

photodiodes operating in linear-gain mode and Geigermode," *Electron Devices, IEEE Transactions on,* vol. 48, pp. 502-511, 2001.

[22] J. L. Pau, R. McClintock, K. Minder, C. Bayram, P. Kung, M. Razeghi, and D. Silversmith, "Geiger-mode operation of back-illuminated GaN avalanche photodiodes," *Applied Physics Letters,* vol. 91, p. 041104, 2007.

[23] A. O. Konstantinov, Q. Wahab, N. Nordell, and U. Lindefelt, "Ionization rates and critical fields in 4H silicon carbide," *Applied Physics Letters,* vol. 71, p. 90, 1997.

[24] B. K. Ng, F. Yan, J. P. R. David, R. C. Tozer, G. J. Rees, C. Qin, and J. H. Zhao, "Multiplication and excess noise characteristics of thin 4H-SiC UV avalanche photodiodes," *Photonics Technology Letters, IEEE,* vol. 14, pp. 1342-1344, 2002.

[25] X. Xin, F. Yan, P. Alexandrove, X. Sun, C. M. Stahle, J. Hu, M. Matsumura, X. Li, M. Weiner, and H. J. Zhao, "Demonstration of 4H-SiC UV single photon counting avalanche photodiode," *Electronics Letters,* vol. 41, pp. 212-214, 2005.

[26] A. L. Beck, X. Guo, H. D. Liu, A. Ghatak-roy, and J. C. Campbell, "Low dark count rate 4H-SiC Geiger mode avalanche photodiodes operated under gated quenching at 325nm," *Proceedings of SPIE,* vol. 6372, p. 63720O, 2006.

[27] A. L. Beck, G. Karve, S. Wang, J. Ming, X. Guo, and J. C. Campbell, "Geiger mode operation of ultraviolet 4H-SiC avalanche photodiodes," *Photonics Technology Letters, IEEE,* vol. 17, pp. 1507-1509, 2005.

[28] X. Xin, J. Hu, P. Alexandov, J. H. Zhao, B. L. VanMil, D. K. Gaskill, K. K. Lew, R. Myers-Ward, and C. Eddy Jr, "High-performance 4H-SiC single photon

avalanche diode operating at solar blind wavelength," *Proceedings of SPIE,* vol. 6771, p. 677114, 2007.

[29] J. Hu, X. Xn, P. Alexandov, J. H. Zhao, B. L. VanMil, and D. K. Gaskill, "4H-SiC Single Photon Avalanche Diode for 280nm UV Applications," in *International Conference on Silicon Carbide and Related Materials* Otsu, Japan, 2007.

[30] X. Bai, D. McIntosh, H. Liu, and J. C. Campbell, "Ultraviolet Single Photon Detection With Geiger-Mode 4H-SiC Avalanche Photodiodes," *Photonics Technology Letters, IEEE,* vol. 19, pp. 1822-1824, 2007.

[31] S. Metz, "The avalanche phototransistor: A novel type of radiation detector and its potential use in optical communication systems," *Electron Devices, IEEE Transactions on,* vol. 22, pp. 617-619, 1975.

[32] C. W. Chen and T. K. Gustafson, "Characteristics of an avalanche phototransistor fabricated on a Si surface," *Applied Physics Letters,* vol. 39, p. 161, 1981.

[33] J. Campbell, A. Dentai, G. Qua, and J. Ferguson, "Avalanche InP/InGaAs heterojunction phototransistor," *Quantum Electronics, IEEE Journal of,* vol. 19, pp. 1134-1138, 1983.

[34] V. Diadiuk, S. Groves, C. Hurwitz, and G. Iseler, "Low dark-current, high gain GaInAs/InP avalanche photodetectors," *Quantum Electronics, IEEE Journal of,* vol. 17, pp. 260-264, 1981.

[35] R. D. Dupuis, J. R. Velebir, J. C. Campbell, and G. J. Qua, "Avalanche photodiodes with separate absorption and multiplication regions grown by

metalorganic vapor deposition," *Electron Device Letters, IEEE,* vol. 7, pp. 296-298, 1986.

[36] F. Y. Huang, "GaAs/InGaAs/AlGaAs optoelectronic switch in avalanche heterojunction phototransistor vertically integrated with a resonant cavity," *Applied Physics Letters,* vol. 64, p. 405, 1994.

[37] G. Bertuccio and R. Casiraghi, "Study of silicon carbide for X-ray detection and spectroscopy," *Nuclear Science, IEEE Transactions on,* vol. 50, pp. 175-185, 2003.

[38] J. F. Seely, B. Kjornrattanawanich, G. E. Holland, and R. Korde, "Response of a SiC photodiode to extreme ultraviolet through visible radiation," *Optics Letters,* vol. 30, pp. 3120-3122, 2005.

[39] R. Yakimova, M. Syvajarvi, T. Iakimov, H. Jacobsson, A. Kakanakova-Georgieva, P. Raback, and E. Janzen, "Growth of silicon carbide: process-related defects," *Applied Surface Science,* vol. 184, pp. 27-36, 2001.

[40] M. Y. Gutkin, A. G. Sheinerman, T. S. Argunova, J. M. Yi, M. U. Kim, J. H. Je, S. S. Nagalyuk, E. N. Mokhov, G. Margaritondo, and Y. Hwu, "Interaction of micropipes with foreign polytype inclusions in SiC," *Journal of Applied Physics,* vol. 100, p. 093518, 2006.

[41] G. Wagner, D. Schulz, and D. Siche, "Vapour phase growth of epitaxial silicon carbide layers," *Progress in Crystal Growth and Characterization of Materials,* vol. 47, pp. 139-165, 2003.

[42] B. J. Skromme, E. Luckowski, K. Moore, M. Bhatnagar, C. E. Weitzel, T. Gehoski, and D. Ganser, "Electrical characteristics of schottky barriers on 4H-

SiC: The effects of barrier height nonuniformity," *Journal of Electronic Materials,* vol. 29, pp. 376-383, 2000.

[43] T. Kimoto, N. Miyamoto, and H. Matsunami, "Performance limiting surface defects in SiC epitaxial pn junctiondiodes," *Electron Devices, IEEE Transactions on,* vol. 46, pp. 471-477, 1999.

[44] D. Nakamura, I. Gunjishima, S. Yamaguchi, T. Ito, A. Okamoto, H. Kondo, S. Onda, and K. Takatori, "Ultrahigh-quality silicon carbide single crystals," *Nature,* vol. 430, pp. 1009-1012, 2004.

[45] A. Itoh and H. Matsunami, "Analysis of Schottky Barrier Heights of Metal/SiC Contacts and Its Possible Application to High-Voltage Rectifying Devices," *Physica Status Solidi (A), Applied Research,* vol. 162, pp. 389-408, 1997.

[46] A. Itoh and H. Matsunami, "Analysis of Schottky barrier heights of metal/SiC contacts and its possible application to high-voltage rectifying devices," *Phys. Stat. Sol. A*, vol. 162, pp.389, 1997.

[47] R. T. Tung, "Electron transport at metal-semiconductor interfaces: General theory," *Phys. Rev. B*, vol. 45, pp. 13509–13523, June, 1992.

[48] F. Roccaforte, F. L. Via, V. Raineri, R. Pierobon, and E. Zanoni, "Richardson's constant in inhomogeneous silicon carbide Schottky contacts," *J. Appl. Phys.*, vol. 93, pp. 9137–9144, June 2003.

[49] F. Yan, X. Xin, S. Aslam, Y. Zhao, D. Franz, J. H. Zhao, and M. Weiner, "4H-SiC UV photo detectors with large area and very high specific detectivity," *IEEE J. Quantum Electron.*, vol.40, pp. 1315, 2004.

[50] F. Paresce, S. Kumar, and C. S. Bowyer, "Continuous discharge line source for the extreme ultraviolet," *Appl. Opt.*, vol. 10, pp. 1904-1908, 1971.

[51] B. L. VanMil, K. K. Lew, R. L. Myers-Ward, R. T. Holm, D. K. Gaskill, C. R. Eddy Jr., “In Situ Measurement of Nitrogen during Growth of 4H-SiC by CVD, ” *Materials Science Forum*, vol. 556-557, pp. 125, 2007.

[52] S. Cova, M. Ghioni, A. Lacaita, C. Samori, and F. Zappa, “ Avalanche photodiodes and quenching circuits for single-photon detection,” *Applied Optics*, vol. 35, no. 12, pp. 1956-1976, April, 1996.

[53] F. H. Ruddy, A. R. Dulloo, J. G. Seidel, S. Seshadri, L. B. Rowland, W. Sci, T. Center, and P. A. Pittsburgh, "Development of a silicon carbide radiation detector," *Nuclear Science, IEEE Transactions on,* vol. 45, pp. 536-541, 1998.

[54] S. Seshadri, A. R. Dulloo, F. H. Ruddy, J. G. Seidel, and L. B. Rowland, "Demonstration of an SiC neutron detector for high-radiationenvironments," *Electron Devices, IEEE Transactions on,* vol. 46, pp. 567-571, 1999.

[55] F. Nava, E. Vittone, P. Vanni, G. Verzellesi, P. G. Fuochi, C. Lanzieri, and M. Glaser, "Radiation tolerance of epitaxial silicon carbide detectors for electrons, protons and gamma-rays," *Nuclear Inst. and Methods in Physics Research, A,* vol. 505, pp. 645-655, 2003.

[56] G. Bertuccio and R. Casiraghi, "Study of silicon carbide for X-ray detection and spectroscopy," *Nuclear Science, IEEE Transactions on,* vol. 50, pp. 175-185, 2003.

[57] P. Bhattacharya, *Semiconductor Optoelectronic Devices, Second Edition*, Prentice Hall, Upper Saddle River, NJ, 1997.

[58] H. Mader and R. Muller, "Transition from the bipolar to the bulk-barrier transistor," *Electron Devices, IEEE Transactions on,* vol. 31, pp. 1447-1454, 1984.

[59] C. Y. Chen, "Theory of a modulated barrier photodiode," *Applied Physics Letters,* vol. 39, p. 979, 1981.

[60] C. M. Sun, D. J. Han, L. Y. Sheng, X. R. Zhang, H. J. Zhang, R. Yang, L. Zhang, and B. J. Ning, "Punch through float-zone silicon phototransistors with high linearity and sensitivity," *Nuclear Inst. and Methods in Physics Research, A,* vol. 547, pp. 437-449, 2005.

[61] S. M. Sze, "Physics of semiconductor devices," pp. 278, 1981.

CURRICULAR VITA

09/2001-07/2008 Ph.D. Program, the Department of Electrical and Computer Engineering, The State University of New Jersey, Rutgers, New Jersey

01/2000-07/2001 M.A. Degree in Physics at Department of Physics, Boston University, Boston, MA

09/1994-07/1998 B.S. Degree in Physics at Department of Physics
Jilin University, Changchun, Jilin, China

PUBLICATIONS

JOURNAL PAPERS

1. J. Hu, L. Lin, X. Xin, J. H. Zhao, and K. Gaskill, “Demonstrationof 4H-SiC Ultraviolet Avalanche Phototransistor,” (in preparation).
2. J. Hu, X. Xin, J. H. Zhao, and K. Gaskill, “Proton irradiation impact to ultraviolet 4H-SiC single photon avalanche diode,” (in preparation).
3. J. Hu, X. Xin, C. L. Joseph, X. Li, and J. H. Zhao, “1×16 Pt-4H-SiC Schottky Photodiode Array for Low-Level EUV and UV Spectroscopic detection,” (submitted to *IEEE Photonics Technology Letters*).
4. J. Hu, X. Xin, X. Li, J. H. Zhao, B. L. VanMil, K. K. Lew, R. L. Myers-Ward, C. R. EddyJr, and D. K. Gaskill, "4H-SiC Visible-Blind Single-Photon Avalanche Diode

for Ultraviolet Detection at 280 and 350 nm," *Electron Devices, IEEE Transactions on,* vol. 55, pp. 1977-1983, 2008.

5. J. Wu, J. Hu, J. H. Zhao, X. Wang, X. Li, L. Fursin, and T. Burke, "Normally-off 4H-SiC trench-gate MOSFETs with high mobility," *Solid State Electronics*, In Press, Corrected Proof, Available online 5 March 2008
6. J. Hu, X. Xin, P. Alexandov, J. H. Zhao, B. L. VanMil, D. K. Gaskill, "4H-SiC Single Photon Avalanche Diode for 280nm UV Applications", *International Conference on Silicon Carbide and Related Materials* (*ICSCRM) 2007*, Oct 14-19, 2007, Otsu, Japan.
7. J. Hu, X. Li, P. Alexandrov, X. Wang, and J. H. Zhao, "5kV, 9.5A SiC JBS with Non-uniform Guard Ring Edge Termination for High Power Switching Applications," *International Conference on Silicon Carbide and Related Materials* (*ICSCRM) 2007*, Oct 14-19, 2007, Otsu, Japan
8. X. Xin, J. Hu, P. Alexandov, J. H. Zhao, B. L. VanMil, D. K. Gaskill, K.-K. Lew, R. Myers-Ward, C. Eddy, Jr., "High performance 4H-SiC single photon avalanche diode operating at solar blind wavelength," *Proceedings of SPIE - Advanced Photon Counting Techniques II,* vol. 6771, pp. 677114-21, 2007.
9. J. Hu, X. Xin, J. H. Zhao, F. Yan, B. Bai, J. Seely, and B, Kjornrattanawanich, "Highly sensitive visible-blind extreme ultraviolet Ni/4H-SiC Schottky photodiode with large detection area," *Optics Lett.*, vol. 31, no. 11, pp. 1591-1593, June, 2006.
10. X. Xin, F. Yan, T. Koeth, C. Joseph, J. Hu, J. Wu, and J. H. Zhao, "Demonstration of 4H-SiC Visible-Blind EUV and UV Detector with Large Detection Area," *IEE Electronic Lett.*, vol. 41, pp 1192, 2005.

11. X. Xin, F. Yan, X. Sun, P. Alexandov, C. M. Stahle, J. Hu, M. matsumura, X. Li, M. Weiner, and J. H. Zhao, "Demonstration of 4H-SiC UV Single Photon Counting Avalanche Photodiode," *IEE Electronic Lett.*, vol. 41, no. 4, pp 212, 2005.

12. S. Feng, C. Lu, J. Hu, Y. Lu, J. Wynn, and C. Ghosh, "Influence of InP Cap Layer on Photon-Responsivity of InP/InGaAs PIN Detector," *The 9th International Conference on Solid-State and Integrated-Circuit Technology (ICSICT)*, Oct. 18-21, Beijing, vol. 3, pp. 2332, 2004.

13. S. Feng, J. Hu, Y. Lu, B. V. Yakshinskiy J. D. Wynn, and C. Ghosh, "Comparative studies of p-type InP layers formed by Zn_3As_2 and Zn_3P_2 diffusion," *J. Electronic Materials*, vol. 32, no. 9, pp. 932, 2003.